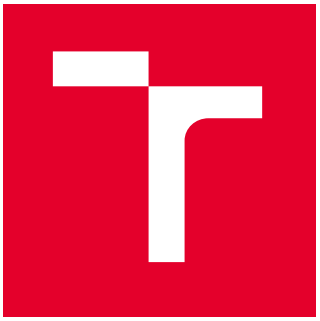

BRNO UNIVERSITY OF TECHNOLOGY

VYSOKÉ UČENÍ TECHNICKÉ V BRNĚ

CENTRAL EUROPEAN INSTITUTE OF TECHNOLOGY BUT

STŘEDOEVROPSKÝ TECHNOLOGICKÝ INSTITUT VUT

DAMAGE MECHANISMS IN MULTIAXIAL FATIGUE

MECHANISMY POŠKOZENÍ PŘI MULTIAXIÁLNÍ ÚNAVĚ

DOCTORAL THESIS

DIZERTAČNÍ PRÁCE

AUTHOR — **Ing. Ladislav Poczklán**

AUTOR PRÁCE

SUPERVISOR — **prof. Mgr. Tomáš Kruml, CSc.**

ŠKOLITEL

BRNO 2023

Abstract

The manuscript is focused on multiaxial fatigue of austenitic stainless steel 316L. The material was cyclically tested in tension/compression and pure torsion as well as in two multiaxial modes formed by their in-phase and 90° out-of-phase combination. All tests were performed in total strain-controlled mode at ambient temperature. Results of fatigue tests suggest that cycling in tension/compression mode causes the fastest crack growth rate and the shortest fatigue life. Torsional mode, on the contrary, led to the slowest propagation of fatigue cracks and the longest fatigue lives. Both multiaxial modes proved to be comparably damaging. Two aspects of microstructural changes were studied in detail: developed dislocation structures and strain-induced martensitic transformation. Electron microscopy was utilized for analyzing both features. In in-phase and both uniaxial modes similar dislocation structures distinguished from those observed in out-of-phase mode were formed which results in the distinct mechanical response observed in the case of out-of-phase loading path. The stability of austenite during cycling was dependent on the loading mode and strain amplitude. The distribution of induced α′ martensite in torsional and out-of-phase modes was strongly heterogeneous. Measuring its content on the outer surface with the Feritscope may give misleading results in some cases. The lowest amount of α′ martensite was observed in tension/compression mode. The endurance against fatigue fracture as well as the tilt angle of the fatigue crack path were predicted using models based on the critical plane approach. The number of cycles to failure was predicted the most precisely by the criterion proposed by Fatemi and Socie. The Smith-Watson-Topper yielded the best predictions of the fatigue crack orientation. The analysis proposed by Polák and the method using the plastic part of the J-integral were applied to investigate the crack growth kinetics. The later approach provided a versatile description of the crack growth rate under all loading paths except out-of-phase mode.

Keywords

Austenitic steel, Multiaxial fatigue, Strain-induced martensite, Dislocation structure, Critical plane, Crack growth rate

Abstrakt

Práce se zabývá víceosou únavou austenitické korozivzdorné oceli 316L. Materiál byl zatěžován cyklicky v tahu/tlaku a krutu. Jejich kombinace byla použita pro testování ve dvou víceosých módech: in-phase (ve fázi) a out-of-phase (mimo fázi). Všechny zkoušky byly provedeny v režimu řízení celkové deformace za pokojové teploty. Výsledky únavových zkoušek naznačují, že cyklování v módu tah/tlak způsobuje nejrychlejší růst trhliny a nejkratší životnost. Naproti tomu torzní mód vedl k nejpomalejšímu šíření únavových trhlin a k nejdelším životnostem. Oba víceosé módy se ukázaly být podobně poškozující. Detailně byly studovány dva aspekty mikrostrukturních změn: vzniklé dislokační struktury a deformačně indukovaná martenzitická transformace. Oba jevy byly analyzovány pomocí elektronové mikroskopie. In-phase zatěžování stejně jako oba jednoosé módy vedly k vytvoření podobných dislokačních struktur odlišných od těch pozorovaných v out-of-phase módu což vedlo k odlišné mechanické odezvě. Stabilita austenitu během cyklování byla závislá na zatěžujícím módu a amplitudě deformace. Rozložení indukovaného α′ martenzitu v torzním a out-of-phase módu se ukázalo být silně heterogenní. Měření jeho obsahu pomocí feritoskopu na vnějším povrchu může v některých případech vést k zavádějícím výsledkům. Nejnižší množství α′ martenzitu bylo pozorováno v módu tah/tlak. Odolnost vůči únavovému lomu a úhel náklonu únavové trhliny byly predikovány pomocí modelů založených na principu kritické roviny. Počet cyklů do lomu byl nejpřesněji předpovězen kritériem, které navrhnul Fatemi a Socie. Model Smith-Watson-Topper vedl k nejlepším odhadům orientace únavové trhliny. Kinetika růstu trhlin byla analyzována metodou navrženou Polákem a dále také pomocí plastické části J-integrálu. Druhý způsob vedl k univerzálnímu popisu rychlosti růstu trhlin ve všech zatěžujících módech s výjimkou out-of-phase, kde výpočet plastické části J-integrálu nebyl proveden.

Klíčová slova

Austenitická ocel, víceosá únava, deformačně indukovaný martenzit, dislokační struktura, kritická rovina, rychlost růstu trhliny

Bibliographic citation

POCZKLÁN, L. Damage mechanisms in multiaxial fatigue. Brno, 2023. Dissertation thesis. Brno University of Technology, Central European Institute of Technology. Supervisor Prof. Mgr. Tomáš Kruml, CSc.

Declaration

I declare that the dissertation thesis called ‘Damage mechanisms in multiaxial fatigue’ was written by myself under the supervision of Prof. Mgr. Tomáš Kruml, CSc. All presented results are original and all sources of information are listed in the References.

Brno, 16.8.2023 Ing. Ladislav Poczklán

Acknowledgment

I would like to thank to my supervisor Prof. Tomáš Kruml for the patient guidance throughout my studies. He always found the time for our countless discussions. I am also grateful to our technicians for teaching me how to control fatigue machines, to Dr. Ivo Kuběna who taught me how to use a scanning electron microscope as well as to Prof. Jaroslav Polák for valuable advice regarding critical plane models. Essentially, I would like to thank to all colleagues from the Low Cycle Fatigue Group for providing a very inspiring and friendly environment.

I would also like to thank to my colleague Dr. Ondrej Slávik who performed the finite element method simulations and to all people who participated in transmission electron microscopy observations.

Lastly, a huge thank you goes to my family and my girlfriend for their endless love, understanding and support.

Contents

1 Introduction

In spite of long and intense research effort, there is still a high likelihood of mechanical failure in common applications caused by fatigue damage [1]. Numerous researchers have investigated the fatigue behavior of many materials, including industrially widely applied 316L steel, over the past few decades [2–12]. However, most of these studies have only looked at uniaxial loading, even though actual loading conditions usually involve multiaxial stresses. The present manuscript is therefore devoted to multiaxial fatigue of austenitic stainless steel 316L. The three main topics of the thesis are i) microstructural changes caused by repeated loading and their influence on mechanical behavior; ii) life-predicting models based on the critical plane approach; iii) kinetics of short fatigue cracks.

The basis of the thesis consists of fatigue tests conducted in four strain-controlled loading modes. Two types of tests were selected, focused on fatigue life and fatigue crack growth. The purpose of 49 fatigue life tests was to obtain characteristics needed for life-predicting models and to study microstructural changes and their influence on the mechanical response. On the other hand, 34 fatigue crack growth tests were conducted to study the kinetics of short fatigue crack growth, to test several existing descriptions of fatigue crack kinetics and to verify the ability of critical plane models to predict the fatigue crack orientation.

Two aspects of microstructural changes during cyclic loading are studied: phase stability of austenite and development of 3D dislocation structures. The main element in austenitic steels which stabilizes the austenite at low temperatures is nickel. Since its price increased rapidly during the last years, manufacturers tend to add just the minimum content allowed by standard (10.0 wt.% in 316L steel). That makes the austenitic phase of 316L steel metastable when subjected to cyclic loading. Many papers have shown the effect of phase transformation from austenite to strain-induced α′ martensite on the mechanical response under uniaxial loading. The change in mechanical properties could be beneficial (α′ martensite is a cause of secondary cyclic hardening), however, the change in magnetic properties (α′ martensite is a magnetic phase) and corrosion resistance may be unacceptable in some applications. This manuscript aims to analyze the amount and distribution of α′ martensite induced in various loading modes.

The density and the spatial arrangement of dislocations influence the mechanical response of the material crucially. It is therefore of considerable interest to understand how the applied loading mode and strain amplitude affect the development of dislocation structures. The situation may be particularly complicated in the case of non-proportional loading because more than one slip system is active in each loading cycle. Dislocation structures were studied using the transmission electron microscopy technique.

Another topic is devoted to predictions of fatigue endurance under conditions of multiaxial loading. Even though there are more concepts on how to estimate fatigue life, the critical plane approach was adopted in the present study. Fifteen models were applied and compared including traditional criteria as well as recently proposed models. Some models contain an additional material parameter whose value has to be determined. Models containing the parameter are consequently less versatile but they should naturally produce more accurate predictions. Critical plane criteria may be also used for a prediction of fatigue crack orientation. This is often overlooked in the literature but the correctness of the crack path prediction can give additional hints for the estimation of the model validity.

The kinetics of short fatigue crack growth was studied using data from tests performed on specimens with an artificial crack starter. Micrographs of growing cracks were taken regularly during cycling and the crack length as a function of the number of loading cycles was estimated afterward. Experimental data in such form were used for further analysis. A universal parameter

describing the crack propagation in multiaxial low cycle fatigue loading conditions was sought in particular, because it is well known that traditional description using stress intensity factor is not applicable in such conditions. Two approaches were applied and compared – the description using crack growth coefficient k_g and the plastic part of the J-integral.

2 State of the art

Austenitic stainless steels are commonly used for the production of components in nuclear reactors as well as in the food, automotive, chemical, health and aerospace industries. They have excellent corrosion resistance and good mechanical properties in a wide range of temperatures [13]. The most commonly used austenitic stainless steels are 304 and 316 which are also known as 18/8 and 18/10 (content of Cr/Ni in wt.%) or A2 and A4. There are also alternatives with lowered content of carbon marked as 304L and 316L which are less susceptible to intergranular corrosion. The main difference in chemical composition between 304 and 316 steel is the content of molybdenum. Steel 316 contains 2 % of molybdenum which makes it more durable against corrosion in the environment with chlorides.

Fatigue of material is dealing with damage cumulated in the material due to cyclic loading. The cumulation of fatigue damage can lead to changes in mechanical properties. This process is usually described as the first stage of fatigue life. The next stages of fatigue life are the initiation and propagation of fatigue cracks which may cause a fracture of a specimen or components. The evolution of fatigue damage is schematized in detail in Fig. 1.

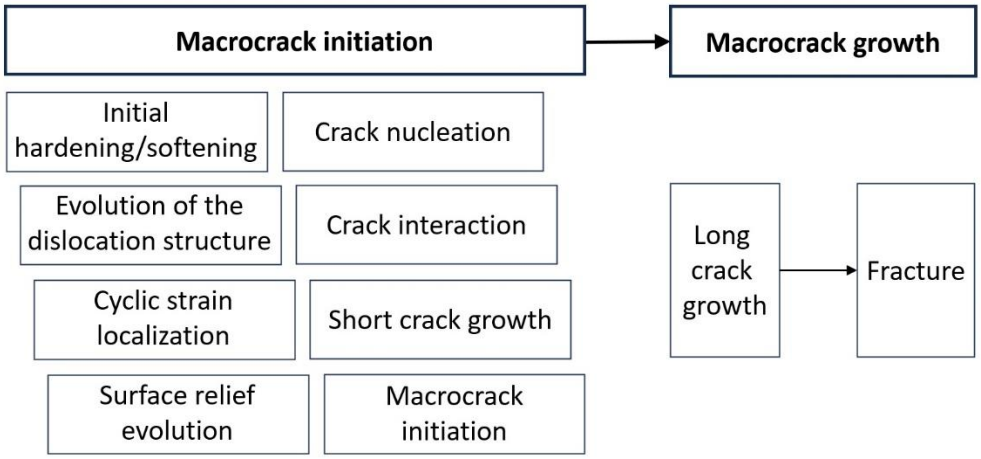

Fig. 1 Evolution of fatigue damage [14].

Since a lot of mechanical parts in the industry are subjected to repeated loading, it is essential to comprehend the mechanisms responsible for the fatigue damage within the process of fatigue life. The number of loading cycles needed for fatigue fracture is a parameter often used for the basic areas of fatigue – low cycle fatigue (up to 10^5 cycles), high cycle fatigue (10^5 – 10^9 cycles), and very high cycle fatigue (10^9 and more).

First historical fatigue studies were aimed only at uniaxial loading corresponding to Mode I (opening mode) of crack propagation, schematically depicted in Fig. 2. Such loading type is often in disagreement with reality – many mechanical components are loaded either in other modes i.e. Mode II (shearing mode) and Mode III (tearing mode) depicted also in Fig. 2 or by their combination.

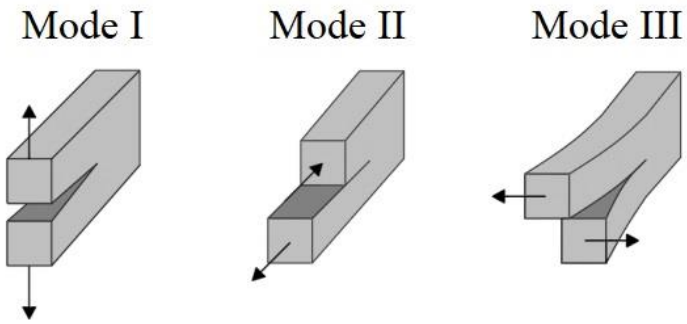

Fig. 2 Three basic loading modes of bodies with long cracks.

Studies dealing with multiaxial cyclic loading appeared throughout time. However, most of these studies were focused on a determination of fatigue life or the development of various life-predicting models. Systematic studies of microstructural changes caused by cyclic loading and studies of fatigue crack growth rates are still rather rare.

Fatigue tests may vary significantly, they can be therefore divided into several groups according to different criteria:

Controlled parameter of fatigue test

- Force or stress (soft regime)
- Total strain (hard regime)
- Plastic strain

Mean stress σ_m

- $\sigma_m = 0$; symmetrical cycle
- $\sigma_m \neq 0$; asymmetrical cycle

Temperature

- Constant (ambient/elevated/lowered)
- Changing (thermomechanical tests)

The shape of the loading curve

- Sinusoidal
- Triangular
- With dwells / without dwells

Loading axis

- Uniaxial
- Multiaxial

2.1 Fatigue of austenitic stainless steels and microstructural changes

Since the range of chemical composition of 316 austenitic steel is relatively large according the AISI standard (e.g. the content of nickel can be between 10 and 14 wt. %), the same type of steel manufactured by various producers can exhibit significantly different behavior. The evidence can be seen in Fig. 3a which shows hardening-softening curves measured on 316L steel provided by two manufacturers. The steel 316L-VZ contains 13.2 wt.% of nickel. The content of nickel in 316L-TH steel is 14.1 wt.% [15]. Curves corresponding to the plastic strain amplitude 5×10^{-4} and 5×10^{-5} are almost identical, however, they vary considerably in the case of the highest amplitude where more intense hardening was observed for the steel containing a lower amount of nickel. A more remarkable difference may be observed in the case of 316L

steel containing 10.0 wt.% of Ni [16] whose hardening-softening curves are shown in Fig. 3b. It is obvious that there is a strong tendency towards softening and secondary hardening. The occurrence of softening phase may be explained by distinct initial states. Both steels depicted in Fig. 3a were annealed while hot rolling preceded the cycling of steel shown in Fig. 3b. The propensity to secondary hardening is however caused by a lower endurance against the phase transformation of metastable austenite to strain-induced α′ martensite related to different chemical composition.

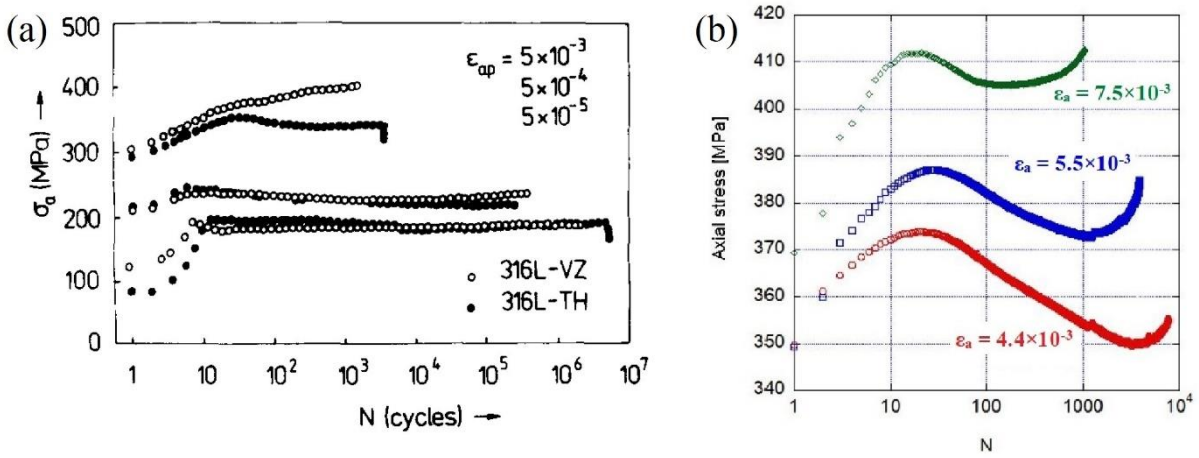

Fig. 3 Cyclic hardening-softening curves of 316L steel (a) annealed, containing 13.2 and 14.1 wt.% of Ni [15]; (b) hot rolled, containing 10.0 wt.% of Ni [16].

Microstructural changes caused by cyclic loading are discussed here from two points of view. The first one is aimed at the evolution of dislocation structures and at the factors which are affecting them. The second is devoted to the phase stability of austenitic stainless steels and to possible ways how to improve it.

2.1.1 Evolution of dislocation structure

A dislocation arrangement during fatigue life in fcc metals is substantially dependent on the value of stacking fault energy (SFE). Dislocations in metals with a high value of SFE can easily cross slip and tend to form spatial structures. On the contrary, planar dislocation structures are characteristic of metals with low SFE [15]. Since SFE of 316L is considered to be between high and low values, the arrangement of dislocations is also dependent on other factors like temperature, chemical composition (mainly on the content of interstitials), and plastic strain amplitude.

On top of that, the dislocation structure is evolving through the fatigue life. Gerland et al. [2] performed a series of transmission electron microscopic (TEM) observations using 316L steel. They cycled the specimen with $\varepsilon_{ap} = 5\times10^{-3}$ and prepared a TEM foil after 25, 300, 4200, 8100, and 10 540 loading cycles. They found out that cellular and wall structures are already developing after 25 cycles. Cells formed around 50 % of the volume while 15 % of the volume was occupied by walls. Both structures were however badly formed - their walls remained thick and a relatively high dislocation density between them was observed. Dislocation tangles were found to be fairly common as well, they covered up to 30 vol%. The number of walls increased after 300 cycles, it constituted up to 25 % of the volume while tangles become rare and filled around 15 vol%. The number of cells kept unchanged and the presence of a labyrinth structure was noted (5 vol%). As the cycling continued, the volume of tangles kept decreasing, and walls transformed into cells that become well-defined and more condensed. At the end of the fatigue life, around 70 % of the volume was covered by cells whose interior was almost free of dislocations.

Effect of plastic strain amplitude

The influence of plastic strain amplitude in tension/compression mode has been studied in several publications [2, 15, 17–19]. It was found that cycling with plastic strain amplitude $\varepsilon_{ap} < 1\times10^{-4}$ led to a planar slip. An example of a planar dislocation structure can be seen in Fig. 4, dislocation rich sheets are separated here by dislocation-free areas.

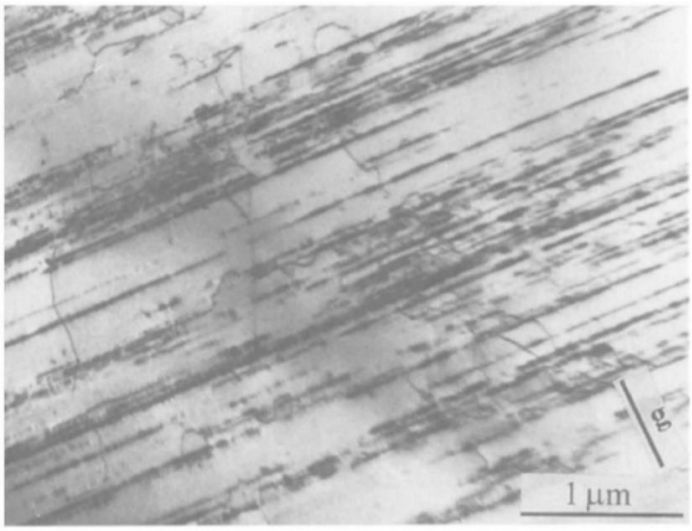

Fig. 4 Planar dislocation structure of sample cycled with plastic strain amplitude 5×10^{-5} [18].

Increasing plastic strain amplitude caused activation of multiple slip systems which led to the formation of spatial dislocation arrangements which prevail at very high amplitudes (higher than 1×10^{-3}). Fig. 5 shows a TEM micrograph taken from a sample after 100 cycles with $\varepsilon_{ap} = 7\times10^{-3}$. Reasonably uniform dislocation cells can be observed.

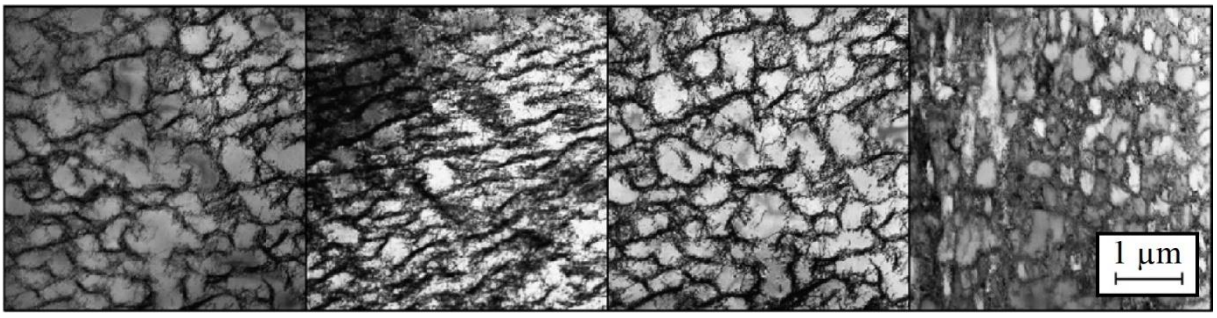

Fig. 5 Cellular dislocation structure after 100 cycles with plastic strain amplitude 7×10^{-3} [17].

Fig. 6 shows the influence of plastic strain amplitude on the arrangement of dislocations. Low loading levels produced planar structures while high amplitudes led to spatial (or 3D) dislocation arrangements. An intermediate level of loading caused the forming of dislocation structures mixed with planar and spatial arrangements. The authors did not find a specific dislocation structure corresponding to the planar–spatial transition [18]. Fig. 6 contains transition curves obtained from cycling of 316L steel and austenitic-ferritic duplex steel. Results reported in other papers [20, 21] are included in this comparison as well. All curves have the same shape but their position along the x-axis is different. It is caused by the differences in SFE mainly due to the various content of interstitials. In the case of duplex steel, only austenitic grains were analyzed and a higher tendency towards planar slip was revealed.

The authors explained it by a higher content of nitrogen in austenitic grains of duplex steel compared to 316L steel [18].

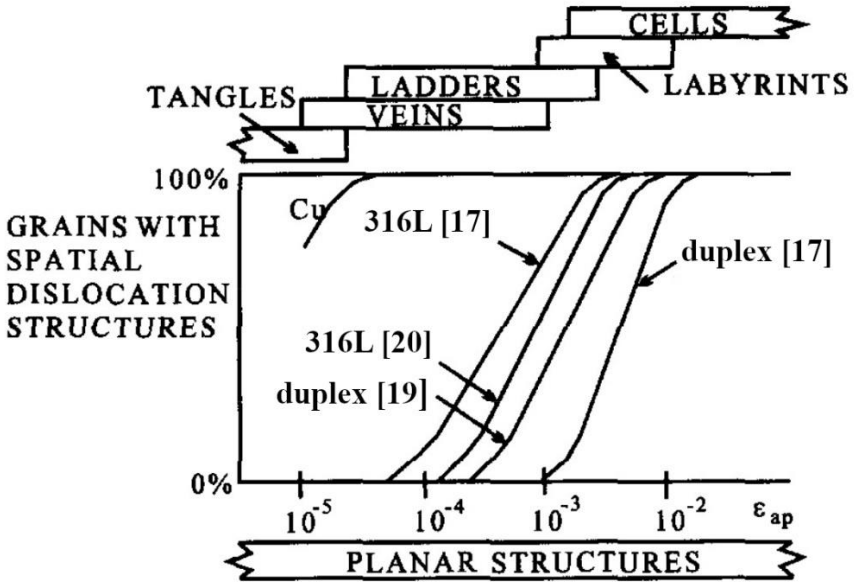

Fig. 6 Developed dislocation structures as a function of plastic strain amplitude [18].

Effect of nitrogen

It was observed, that nitrogen is the most effective interstitial alloying element in terms of solid solution strengthening [22]. It has a positive effect on static mechanical characteristics like yield strength and ultimate tensile strength [22]. The effect on fatigue properties and dislocation structures of austenitic stainless steels was studied as well [3, 4, 22–24]. Based on the given research it can be concluded that an increased amount of nitrogen improves fatigue life and crack growth rate of austenitic steels. The reason is the decreased value of SFE and increased tendency to planar slip. The evidence of more frequent planar slip in the case of steel containing a higher amount of nitrogen (marked as 316LN) can be seen in Fig. 7. Planar slip leads to slower evolution of dislocation structures during fatigue and better resistance towards localization of plastic strain into persistent slip bands. More homogenous plastic strain promotes slip reversibility and prolongs the initiation of fatigue cracks [22].

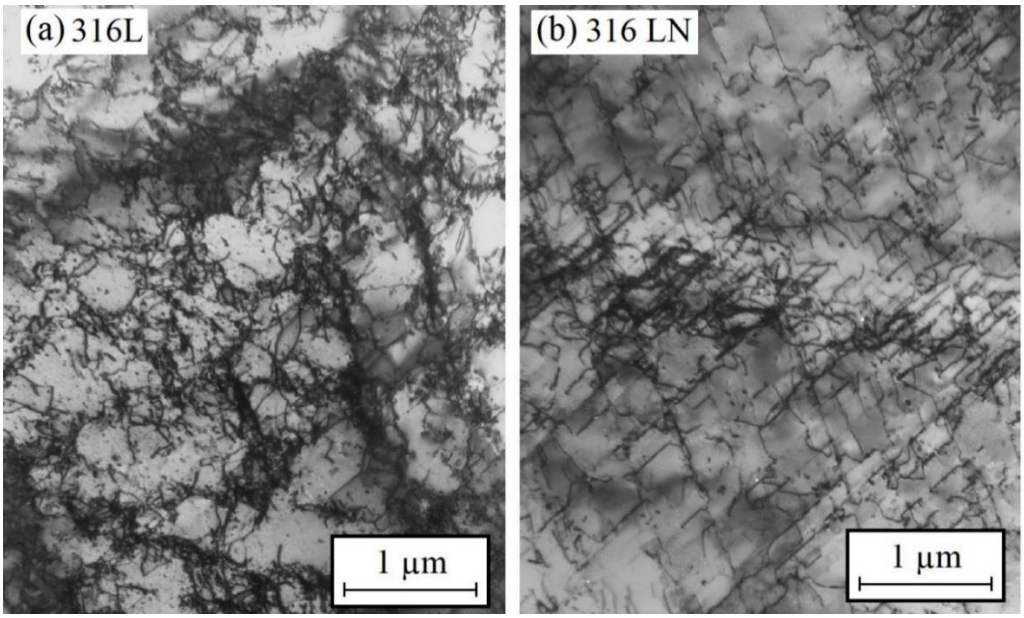

Fig. 7 Dislocation structure of austenitic steel with (a) 0.038 wt.% N (b) 0.14 wt.% N developed after cycling with the range of stress intensity factor 35 MPa$\sqrt{m}$ [3].

Effect of temperature

Vogt et al. [25] studied the influence of a decrease in temperature on dislocation structure. Samples from 316L and 316LN cycled with total strain amplitude 2.5×10^{-3} at 27 °C exhibited dislocations arranged into walls which were less condensed and less often misoriented in the case of 316LN. Observations of samples cycled at -196 °C revealed a lower tendency to cross slip in both materials although this feature was more obvious in the case of 316LN. This finding is in agreement with the study of Kruml et al. [5]. The main difference in microstructure of 316L and 316LN cycled at -196 °C was the amount of α′ martensite, this will be discussed later.

Papers dealing with cycling at elevated temperatures are much more frequent [6, 26–29]. The most important finding from these studies is the following: in the interval of temperature from room temperature (RT) up to 200 - 300 °C dislocations can cross slip more easily at increasing temperatures, since the cross-slip is a thermally activated mechanisms [30] (depending on strain amplitude) and form cellular and wall structures. However, cross slip is becoming more difficult with increasing temperature. Planar slip is again prevailing in the temperature interval of 300 - 500 °C, this results in a formation of a corduroy structure. Cycling at temperatures higher than 600 °C leads to dislocation structures similar to those observed at RT. Such behavior is considered to be a consequence of dynamic strain aging which occurs in a certain range of temperatures. Hong and Lee [31] found out that the upper limit of this interval is slightly dependent on strain rate (it increased from 550 °C to 650 °C with an increased strain rate from 1×10^{-4} s^{-1} to 1×10^{-2} s^{-1}).

Effect of loading mode

All papers mentioned so far in this chapter were aimed only at fully reversed tension-compression loading mode. Studies concerning multiaxial loading modes are relatively rare. One such study was made by Mazánová et al. [32], their goal was to compare dislocation structures developed in 316L steel by cycling in in-phase and 90° out-of-phase tension/torsion mode with equivalent strain amplitude 3.5×10^{-3}. Their results indicate that in-phase mode leads to the development of the cellular structure. Dislocations observed in the out-of-phase mode were arranged into walls – see Fig. 8.

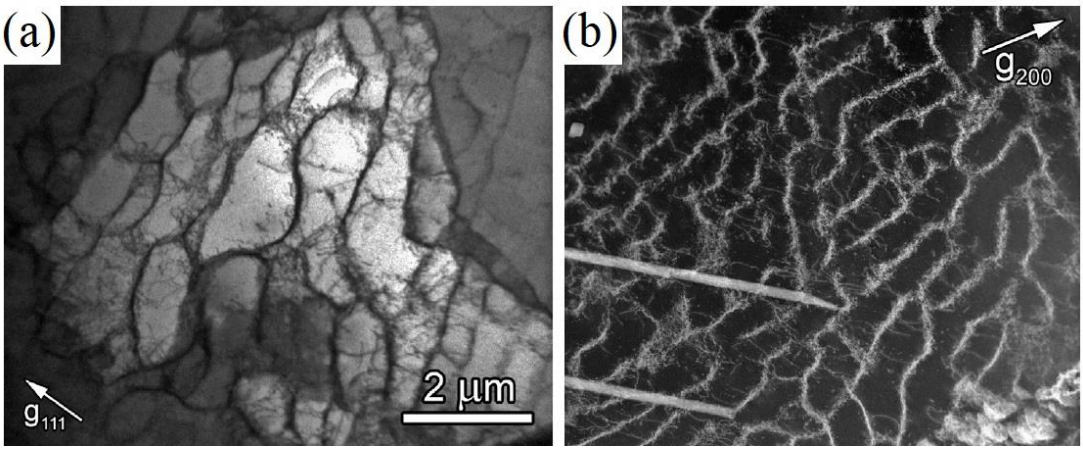

Fig. 8 TEM micrographs of dislocation structures developed by cycling with equivalent strain amplitude 0.35 % in (a) in-phase mode and (b) out-of-phase mode [32].

Dey et al. [33] performed similar tests with 304LN steel and equivalent strain amplitude 1×10^{-2}. TEM micrograph taken from a sample cycled in in-phase mode exhibited a planar arrangement of dislocations contrary to an out-of-phase mode wherein the dislocation structure consisted of well-defined dislocation cells. Doong et al. [34] performed a set of out-of-phase mode tests on 304 and 310-type steel. Their finding is that dislocations tend to form tangles in the case of small plastic strain amplitude but as the amplitude increases, walls, cells, and labyrinths were observed.

2.1.2 Strain-induced martensitic transformation

Another example of microstructural change during the fatigue life of austenitic stainless steels is phase transformation from austenite to martensite. A rising price of nickel forces steel manufacturers to lower its content. Since nickel is the main element stabilizing austenite in austenitic steels it has negative consequences on their phase stability. However, the occurrence of martensite can be both, positive and negative. The formation of ferromagnetic α′ martensite is for example a principle of TRIP (transformation-induced plasticity) steel sensor measuring the peak of strain during service [35]. On the other hand, the presence of a magnetic phase is strongly undesirable in the case of superconducting magnets [36]. The presence of α′ martensite also lowers the corrosion resistance of the steel.

Mechanism of strain-induced martensitic transformation

A mechanism of strain-induced martensitic transformation was studied in detail by Bogers and Burgers [37], and their work was later extended by Olson and Cohen [38–40]. There can be two types of martensite in austenitic steels. The first one is marked as α′ martensite (tetragonal structure) and the second one is marked as ε (HCP structure). The mechanism of formation of α′ martensite directly from austenite is shown in Fig. 9. A nucleation site of α′ martensite is an intersection of two shear bands parallel to (111) planes. One of these bands has to contain Shockley partial dislocation $\frac{a}{6}\{211\}$ on every second plane and the other one on every third plane.

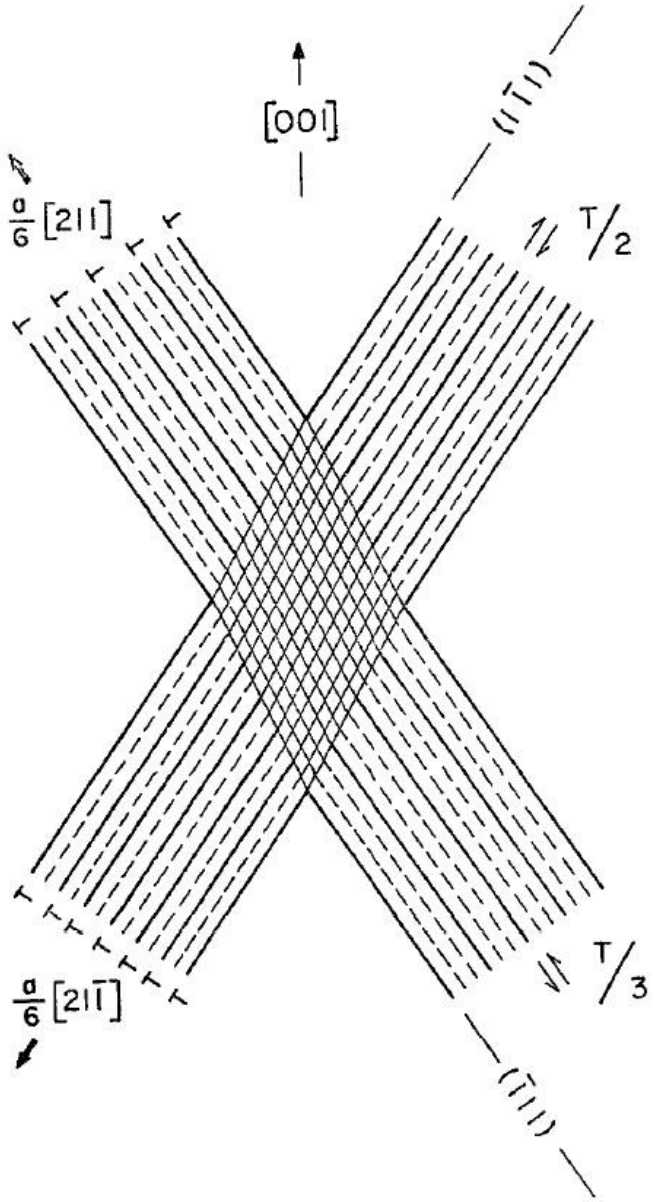

Fig. 9 Nucleation site of α′ martensite [40].

ε martensite forms in a similar way as α′ martensite, the only difference is that Shockley partial dislocations have to be placed on every second close-packed plane. α′ martensite can also develop in an intersection of two ε martensite plates. This situation can be observed in Fig. 10 which represents a TEM micrograph taken from a sample cycled with a total strain amplitude of 1.6×10^{-2} at the temperature of liquid nitrogen. ε martensite is present here in form of very thin plates which can be easily misinterpreted as deformation twins [5]. Analysis of diffraction patterns revealed that the majority of plates are ε martensite. It can be seen that α′ martensite develops at almost every intersection of two systems of plates [5].

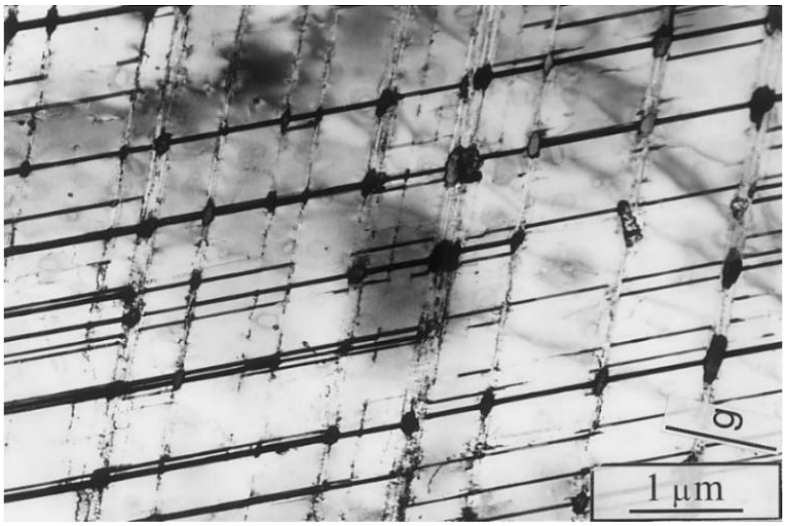

Fig. 10 Nucleation of α′ martensite in the intersection of ε martensite plates after cyclic loading with total strain amplitude 1.6×10^{-2} [5].

Effect of alloying on the stability of austenite

It is well known that due to the higher content of nickel and molybdenum, 316 steel exhibits better phase stability than 304 steel. The effect of nitrogen was studied by Vogt et al. [25] who compared 316L and 316LN steels cycled at -196 °C. X-ray diffractometry measurements found approximately 66 % of α′ martensite in a sample from 316L steel and only 4 % in 316LN steel. Smaga et al. [35] compared the phase stability of 304 steel with titanium alloyed 321 steel and niobium alloyed 348 steel. Their results of feritscope measurements indicate that 304 is more stable than 321 and the least stable is 348 steel. Krupp et al. [41] did a series of fatigue tests on 301 steel with different content of carbon, they conclude that lower content of carbon leads to better resistance against martensitic transformation. Talonen and Hänninen [42] and Olson and Cohen [40] concluded that increasing SFE causes more difficult nucleation of α′ martensite. The reason is that there is a critical size of α′ martensite embryo needed. It was calculated and also confirmed by TEM observations by Staudhammer et al. [43] as 27 close-packed layers. Since increasing SFE leads to decreasing length and width of stacking fault packets, the probability of the formation of sufficiently large α′ martensite embryos is lower as well [40]. Alloying elements increasing SFE hence improve phase stability of austenitic steels.

Effect of strain amplitude, strain rate, temperature, and grain size

Results of several studies [35, 42, 44, 45] agree that increasing strain amplitude promotes strain-induced martensitic transformation. Das et al. [45] performed fatigue tests with various strain amplitudes on 304LN steel and they explain this phenomenon as follows: increasing strain amplitude leads to a formation of larger dislocation cells which decreases its ability to accommodate plastic strain and therefore encourages the formation of α′ martensite. Pegues et al. [46] and Talonen et al. [47] investigated the effect of strain rate. Their results indicate that increasing strain rate reduces the formation of α′ martensite. The reason is according to both papers in adiabatic heating which is more intense in the case of higher strain rate and suppresses the development of strain-induced α′ martensite. The effect of temperature on strain-induced martensitic transformation has been studied in detail [41, 42, 44] and it is well known that decreasing temperature increases a driving force of this transformation. In other words, cyclic loading at higher temperatures results in lower content of martensite. The influence of grain size was studied as well. Varma et al. [48] found out that the amount of α′ martensite was higher in samples with coarser grains.

Effect of loading mode

Probably the most complex research concerning a relationship between loading path and content of α′ martensite so far was carried out by Li et al. [49]. They chose 304L steel as an experimental material and performed tests with eight different loading paths which are listed in Tab. 1. Equivalent total strain amplitude was always 5×10^{-3}. Values of non-proportionality of particular loading paths were calculated according to Itoh's definition [50] – see Eq. 1.

$$f_{NP} = \frac{1.57}{T\varepsilon_{1max}} \int_0^T (|\sin \xi(t)| \varepsilon_1(t))\, dt, \tag{1}$$

where f_{NP} is the factor of non-proportionality, T is the period, ε_{1max} is the maximum principle strain, $\varepsilon_1(t)$ is the principle strain at time t and $\xi(t)$ is the angle between ε_{1max} and $\varepsilon_1(t)$.

Tab. 1 Loading modes used by Li et al. [49].

Loading Path Name	Loading Path Sketch	Loading Path Name	Loading Path Sketch
Uniaxial	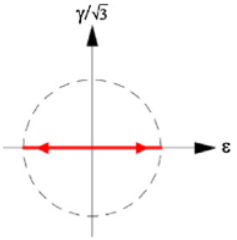	Torsional	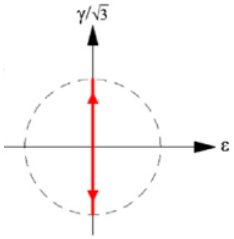
Proportional	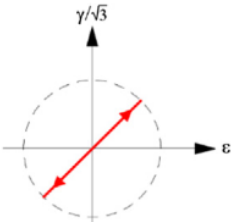	Ladder	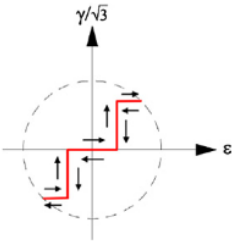
Cross	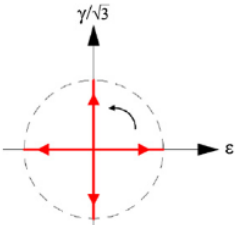	Rhombus	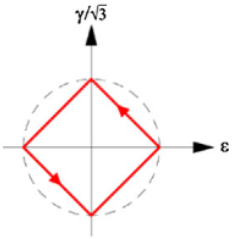
Square	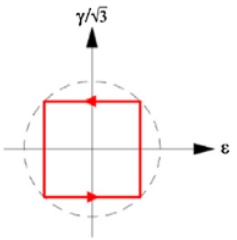	Circular	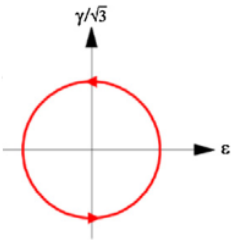

The content of α′ martensite was measured continuously during cycling via feritscope and its content is plotted as a function of cumulative plastic strain in Fig. 11. The shortest incubation period was observed in circular mode. This mode also had the highest value of non-proportionality (equal to 1.00). The second shortest incubation period was in square and rhombus mode. Non-proportionality value of these two modes was 0.77 which corresponds to the overlapping of their data points. Phase transformation began the latest in modes with zero value of non-proportionality (proportional, uniaxial, and torsional mode). The incubation period of ladder mode whose non-proportionality is 0.1 is only slightly shorter. The presented results

can be concluded as follows: the incubation period of strain-induced martensitic transformation is decreasing with increasing non-proportionality.

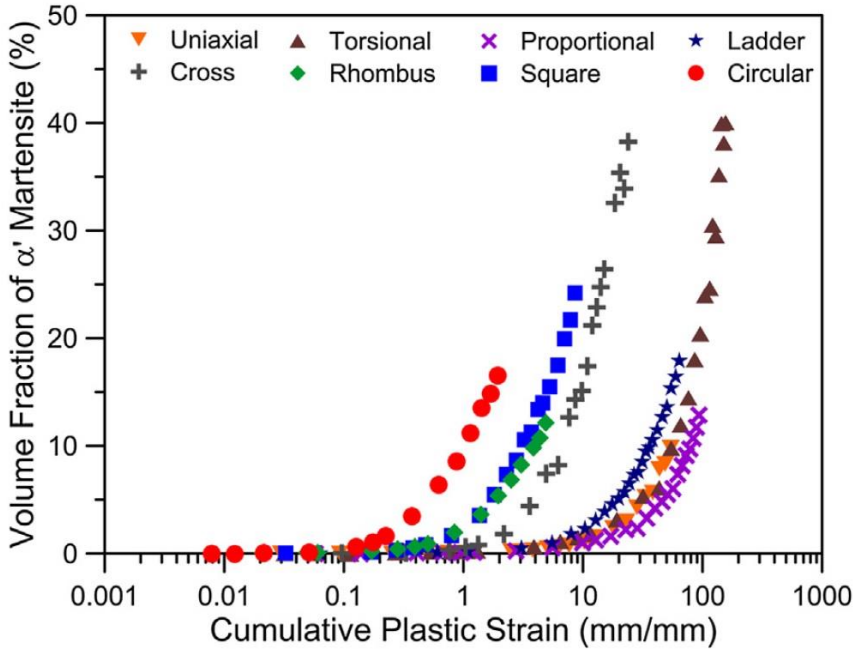

Fig. 11 Content of martensite as a function of cumulative plastic strain in 304L steel for various loading paths [49].

However, the highest content of α′ martensite at the end of fatigue life was in torsional and cross mode. The lowest content of α′ martensite measured post-mortem was in rhombus, proportional and uniaxial modes. Mazánová et al. [32] did similar series of tests on 316L steel with an equivalent strain amplitude of 3.5×10^{-3} for tests in in-phase and 90° out-of-phase mode and 4×10^{-3} strain amplitude in torsional mode. Loading modes used in their study correspond to torsional, proportional, and rhombus loading paths in Tab. 1. They measured the content of α′ martensite after the end of fatigue life and found out that the highest value was also in torsional mode (12.8 %). Values of in-phase and out-of-phase modes were 3.6 % and 1.6 %, respectively. Abovementioned results prove a more intense martensitic transformation in torsional mode. They also suggest a better phase stability of 316L steel in comparison with 304L steel.

Influence on fatigue behavior

Since both kinds of martensite exhibit higher strength and hardness compared to austenite, the formation of strain-induced martensite should lead to the strengthening of austenitic steels. The development of α′ martensite is also accompanied by a change in volume which is approximately 2 % for 304 steel [51]. Newly formed α′ martensite deforms surrounding austenite and thus influences its mechanical behavior.

Since cyclic hardening was confirmed as a direct consequence of α′ martensite formation in several studies [46, 52, 53] aforementioned assumptions seem to be justified. Baudry and Pineau [52] state that strain-induced martensitic transformation significantly decreases the number of cycles to fracture in the case of cycling with a given plastic strain amplitude. However, this effect is less intense when cycling with constant total strain amplitude is applied. The decrease of fatigue lives with the formation of α′ martensite was also observed by Lehnhoff and Findley [54] who were controlling total strain amplitude during tests. This finding is in agreement with fatigue strengths proclaimed by manufacturers for 304 and 316 steel. According

to Baudry and Pineau cycling with constant plastic strain amplitude also led to an acceleration of initiation and propagation of fatigue cracks. Mei and Morris [55] applied cyclic loading with constant load and concluded that martensitic transformation significantly reduces crack propagation rate, especially at reduced temperatures.

2.2 Multiaxial fatigue

There are two fundamental categories of multiaxial loading: proportional and non-proportional. Proportional loading is characterized by a consistent direction of principle stress and strain. On the contrary, the direction of principle stress and strain is continuously changing during the non-proportional loading cycle. There is an agreement in the literature that non-proportional cyclic loading is more damaging in terms of fatigue life [56]. The change of principle strain direction causes the development of multi-slip dislocation structures and additional cyclic hardening, leading to a decrease in plastic strain amplitude and a worse fatigue life endurance [57, 58]. Studies have been conducted to investigate the mechanism of fatigue crack initiation and early growth under multiaxial loading, as well as the development of dislocation structures [32, 59]. Additionally, other studies have explored the effects of internal pressure combined with applied tension-compression fatigue loading or exposed 316L steel to ratcheting paths [60–63].

Predicting fatigue endurance requires a sophisticated method due to the intricate structure of actual components and multiaxial loading conditions. The critical plane approach, first suggested by Stanfield in 1935 [64], is widely utilized because of its efficiency and applicability to diverse conditions. Criteria based on the critical plane approach assume that both the initiation and early growth of a fatigue crack happen on a particular plane every time. They determine a damage parameter using stress and/or strain components. These models can be grouped depending on damage parameter calculation into stress models, strain models, and energy models that combine stress and strain.

Findley [65] developed one of the earliest critical plane models in the late 1950s, which emphasized the role of shear stress in fatigue crack initiation and the promotion of crack growth by tensile stress normal to the plane of maximum shear stress. Wang and Brown (WB) [66] as well as Kandil et al. (KBM) [67] adapted a model initially developed by Brown and Miller (BM) [68], which considers shear and normal strain. Fatemi and Socie (FS) [69] proposed using the maximum shear strain and normal stress on the maximum shear strain plane to account for nonproportional hardening. Smith et al. (SWT) [70] designed a strain energy density model consequently adjusted by Socie [56] for multiaxial loading conditions. The SWT model is found to be convenient for materials that tend to crack according to Mode I. The FS and WB models, on the other hand, are suitable for materials that crack according to Mode II. Ince and Glinka [71] introduced a generalized strain energy (GSE) model, which uses normal and shear strain energy and can take into consideration mean stress as well as nonproportional hardening. Ince and Glinka also modified the elastic strain terms of GSE model to develop a generalized strain amplitude (GSA) criterion. Yu et al. [72] improved both models to enhance the accuracy of predictions under pure shear loading. Zhu et al. [73] included an additional material parameter to make the GSE model more versatile and applicable for different kind of materials.

Jiang [74] suggested a damage parameter derived from the SWT criterion, which was later related to fatigue life by Ma et al. [75]. Li et al. [57] developed a model that is based on KBM and FS criteria but does not require an additional material parameter. Zhu et al. [76] introduced an energy-based model that calculates a damage parameter by summing the elastic and plastic work per cycle, making predictions possible in both low and high cycle fatigue regimes. The authors Liu et al. [77] introduced two models, one for materials that experience tensile cracking and another for those that undergo shear cracking. Both of these models rely on the concept of energy strain density. The models created by Chen et al. [78] are comparable to Liu's models,

although the critical plane's characterization varies slightly. Lagoda et al. [79] put forward a model that is based on strain energy density and can be employed for random loading in both low and high cycle fatigue ranges. The critical plane determined by Varvani-Farahani [80] is the one with the highest Mohr's stress and strain circles. The damage parameter in his model was calculated by adding the normal and shear energy range, weighted by the normal and shear fatigue properties. Several papers have reviewed life-predicting models based on the critical plane approach [81–83]. A large survey of models predicting the fatigue limit was performed by Papuga [84]. The number of criteria has been constantly rising in the past few years [85–92].

Critical plane models are also utilized to determine the tilting of fatigue cracks paths. Bemfica et al. [58] conducted a study on the cyclic loading of 304L steel and determined the crack orientation with SWT, FS, and Jiang models. However, they discovered that none of these models could provide satisfactory predictions in every loading mode. In a similar study, Castro and Jiang [93] examined crack directions with the same criteria using extruded magnesium alloy as the experimental material and found that the Jiang model provided the most accurate predictions. Wang and Susmel [94] investigated the tilting of fatigue cracks initiated on samples subjected to constant and variable amplitude by comparing the shear strain maximum variance method and the maximum damage method, both of them generated satisfactorily precise results. Vantadori et al. [95] applied a Carpinteri model to explore the fatigue life and fatigue crack orientation of 316L steel in the high cycle fatigue regime.

The first part of this section is dealing with life-predicting models which are applicable for repeated multiaxial loading. Even though there are more ways how to predict fatigue life, only critical plane criteria are discussed. The second part is focused on short fatigue cracks, selected aspects - initiation, orientation, branching, and kinetics of early crack growth in conditions of multiaxial loading are discussed.

2.2.1 Critical plane models

Basquin-Manson-Coffin (BMC):

Critical plane criteria are usually described by an equation whose left side includes the damage parameter while the number of cycles to fracture N_f appears within the right side, typically derived from the BMC equation:

$$\varepsilon_{a,eq} = \frac{\sigma_f'}{E}(2N_f)^b + \varepsilon_f'(2N_f)^c, \tag{2}$$

where σ_f' is a fatigue strength coefficient, E is Young's modulus, b is a fatigue strength exponent, ε_f' is a fatigue ductility coefficient and c is a fatigue ductility exponent.

As the name suggests, the BMC equation was derived from the Basquin and Manson-Coffin law defined by Eq. 3 and Eq. 4, respectively.

$$\sigma_a = \sigma_f'(2N_f)^b, \tag{3}$$

$$\varepsilon_{ap} = \varepsilon_f'(2N_f)^c, \tag{4}$$

Wang-Brown model (WB):

The most recognized strain criterion was originally proposed by Brown and Miller [68] it was further modified by Kandil et al. [67] and by Wang and Brown [66]. WB criterion is suitable for loading conditions that result in significant plastic strain, this is a typical feature of low cycle fatigue regime [57]. Eq. 5 gives a form of WB model for crack Type A (definition of

crack Type A and B is shown in paragraph 5.2.2). It is believed that S becomes zero for crack Type B in the case of proportional loading. The main disadvantage of the WB model is that cyclic hardening or softening cannot be taken into account in strain-controlled fatigue tests. Strain-based damage parameters also cannot reflect the effect of mean stress [81].

$$\gamma_{a,max} + S\Delta\varepsilon_n = \left(1 + \nu_e + S(1-\nu_e)\right)\frac{\sigma_f'}{E}(2N_f)^b + \left(1 + \nu_p + S\left(1-\nu_p\right)\right)\varepsilon_f'(2N_f)^c, \quad (5)$$

where $\gamma_{a,max}$ and $\Delta\varepsilon_n$ are an amplitude of maximum shear strain and a range of normal strain in the critical plane, S is a coefficient of normal strain influence and it is determined by experiments, ν_e and ν_p are elastic and plastic Poisson's ratios, respectively.

Fatemi-Socie model (FS):

As mentioned before, since both controlling parameters in the BM criterion are of strain type, the additional cyclic hardening and mean stress cannot be considered. To solve this problem, Fatemi and Socie [69] used maximum normal stress instead of maximum normal strain. Fatemi-Socie (FS) damage parameter is a typical example of a criterion using stress and strain characteristics. This feature is generally considered an advantage compared to the BM criterion. FS equation for life prediction can be written in terms of shear strain properties (Eq. 6) but also in terms of uniaxial properties (Eq. 7).

$$\gamma_{a,max}\left(1 + k\frac{\sigma_{n,max}}{\sigma_y}\right) = \frac{\tau_f'}{G}(2N_f)^{b_0} + \gamma_f'(2N_f)^{c_0}, \quad (6)$$

where $\gamma_{a,max}$ and $\sigma_{n,max}$ are an amplitude of maximum shear strain and the maximum normal stress in the critical plane, k is a material constant, σ_y is the yield strength, τ_f' is a shear fatigue strength coefficient, G is shear modulus, b_0 is a shear fatigue strength exponent, γ_f' is a shear fatigue ductility coefficient and c_0 is a shear fatigue ductility exponent.

$$\gamma_{a,max}\left(1 + k\frac{\sigma_{n,max}}{\sigma_y}\right) = \left[(1+\nu_e)\frac{\sigma_f'}{E}(2N_f)^b + \left(1+\nu_p\right)\varepsilon_f'(2N_f)^c\right]\left(1 + n\frac{\sigma_f'}{2\sigma_y}(2N_f)^b\right), \quad (7)$$

Smith-Watson-Topper model:

Smith, Watson, and Topper (SWT) criterion [70] defines a damage parameter as stress and strain product $\sigma_{max}\varepsilon_a$. This damage parameter is used only for uniaxial tension-compression loading and is often successfully applied for prediction of fatigue life of uniaxial cycling with mean stress. Socie [56] modified it for multiaxial loading using parameters ε_1 and σ_n (see Eq. 8).

$$\sigma_{n,max}\ \frac{\Delta\varepsilon_1}{2} = \frac{\sigma_f'^2}{E}(2N_f)^{2b} + \sigma_f'\varepsilon_f'(2N_f)^{b+c}, \quad (8)$$

where $\frac{\Delta\varepsilon_1}{2}$ and $\sigma_{n,max}$ are the amplitude of maximum principal strain and maximum normal stress in the critical plane.

Such a form of SWT parameter can be used for a prediction of fatigue life in conditions of proportional and non-proportional multiaxial loading. SWT damage parameter gives more accurate results for materials in which cracks grow according to Mode I in contrast with FS model which is more suitable for fatigue life predictions of materials in which cracks grow according to Mode II.

MKBM model:

A criterion introduced by authors Li et al. [57] is based on FS and BM criteria, the critical plane is therefore the plane of maximum shear strain. Controlling parameters are shear strain and normal strain and stress - see Eq. 9:

$$\gamma_{a,max} + \left(1 + \frac{\sigma_{n,max}}{\sigma_y}\right)\frac{\Delta\varepsilon_n}{2} = \left[\frac{\sigma_f'}{E}(2N_f)^b + \varepsilon_f'(2N_f)^c\right]\left(1 + \frac{\sigma_f'}{\sigma_y}(2N_f)^b\right), \tag{9}$$

where $\sigma_{n,max}$ is determined by using Eq. 10 derived from Ramberg Osgood relation modified by Chen [96] who introduced the factor of non-proportionality:

$$\varepsilon_{n,max} = \frac{\sigma_{n,max}}{E} + \left[\frac{\sigma_{n,max}}{K\prime(1+L\phi)}\right]^{\frac{1}{n\prime}}, \tag{10}$$

where $\varepsilon_{n,max}$ is the maximum normal strain, K' is a coefficient of cyclic hardening, L is a coefficient of non-proportional hardening, ϕ is a non-proportionality factor and n' is an exponent of cyclic hardening. The coefficient K' and the exponent n' were derived from the cyclic stress strain curve defined by Eq. 11:

$$\sigma_a = K'\varepsilon_{ap}^{n'}, \tag{11}$$

It is also worth notice that the mean stress can be easily accounted for in this model. Li et al. used their criterion for fatigue life estimation of 20 materials including austenitic stainless steels 304L and 316L. They collected data from more than 600 fatigue tests performed by various authors and made a comparison with their predictions. Fig. 12 and Fig. 13 show results for proportional and non-proportional tests, it can be seen that the majority of data fell into the factor-three-band (dashed lines). However, the scatter of non-proportional data was proved to be larger.

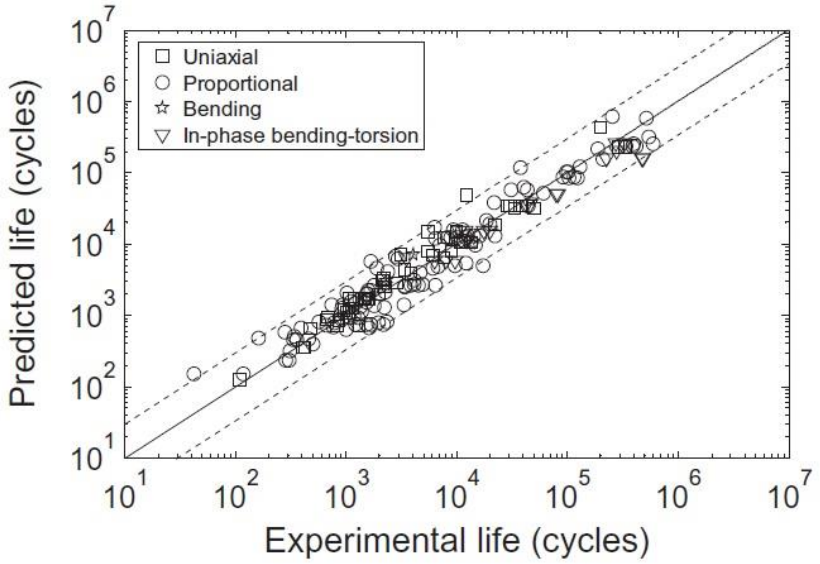

Fig. 12 Comparison of measured life and life predicted according to MKBM criterion – uniaxial and multiaxial proportional tests [57].

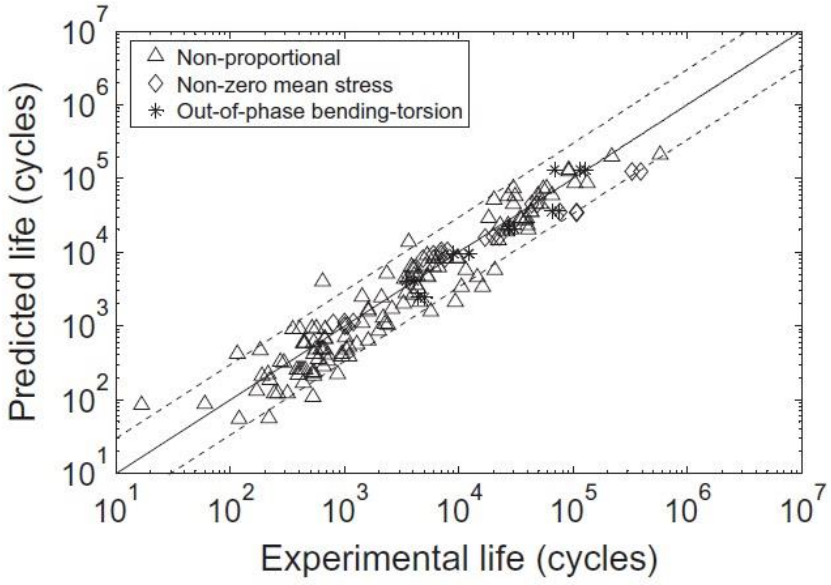

Fig. 13 Comparison of measured life and life predicted according to MKBM criterion for multiaxial non-proportional tests [57].

Li model:

A model proposed by Li et al. [86] is derived from a model designed by Chen et al. [78]. It is based on a calculation of strain energy density and the plane with maximum shear strain energy density is supposed to be critical. The stress-strain analysis revealed that there are at least two planes where shear strain energy density reaches the maximum value. The plane with a larger normal strain energy density is thus defined as critical. The model is defined by Eq. 12, where $\Delta\tau_t$ is the shear stress range acting on the maximum shear strain range plane and τ_m is the mean shear stress acting on the critical plane. It was observed that mean shear stress has a damaging effect on fatigue life [97, 98] as well as positive normal mean stress meanwhile negative normal mean stress is beneficial from a fatigue life view. It is therefore desirable to design a criterion that takes into account these factors.

$$\left(\frac{\Delta\tau_t}{2}+|\tau_m|\right)\frac{\Delta\gamma_{max}}{2}+L_{Li}\sigma_{n,max}\frac{\Delta\varepsilon_n}{2}=\frac{\tau_f'^2}{G}(2N_f)^{2b_0}+\tau_f'\gamma_f'(2N_f)^{b_0+c_0} \tag{12}$$

Weight index L_{Li} contained in the damage parameter considers the different impacts of shear and normal strain energy on the fatigue life. Its value is determined using parameter P_F which is calculated with Eq. 13, where m_F is the number of fully reversed uniaxial experiments. The authors suggest calculating P_F for every L_{Li} in the interval from 0 to 10 using a step size equal to 0.01. L_{Li} corresponding to the minimum P_F is the weight index L_{Li}.

$$P_F=\sum_{i=1}^{m_F}\left\{\frac{\tau_f'^2}{G}(2N_f)^{2b_0}+\tau_f'\gamma_f'(2N_f)^{b_0+c_0}-\frac{\Delta\sigma_i\Delta\varepsilon_i}{8}\left[(1+\nu_{eff})+L_{Li}\frac{1-\nu_{eff}}{2}\right]\right\}^2 \tag{13}$$

Li et al. collected experimental data from other authors. The data were obtained from testing eight materials in both loading modes – proportional and non-proportional. They calculated the fatigue lives for eight materials and compared them with experiments. They found out that 100 % of data points fell inside the factor-three-band in the case of proportional tests (Fig. 14). The number of data points lying inside the band was slightly lower when fatigue lives under non-proportional loading were predicted, 92.3 % of predictions fulfilled this condition (see Fig. 15).

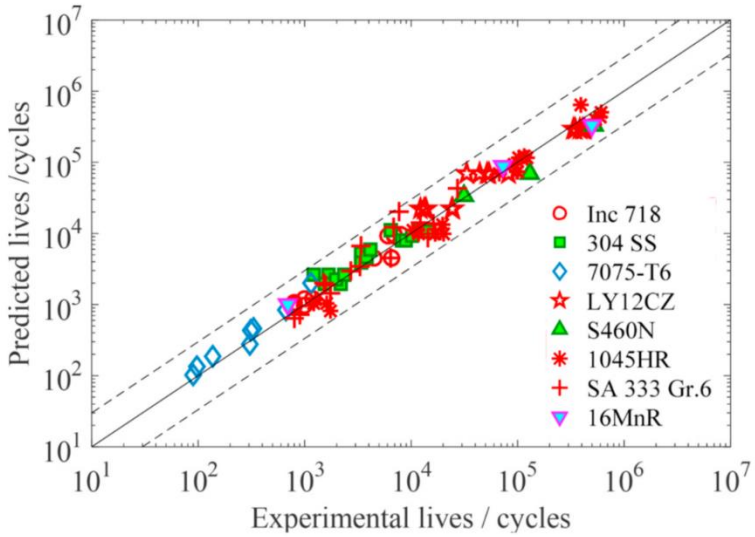

Fig. 14 Comparison of measured life and life predicted according to Li criterion for proportional tests [86].

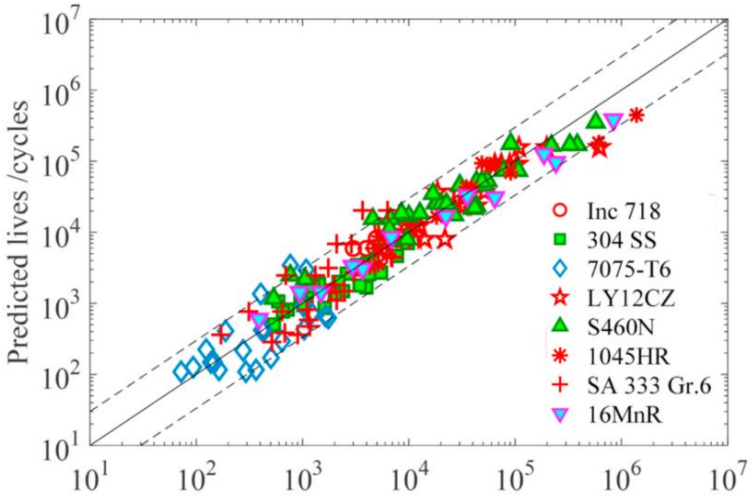

Fig. 15 Comparison of measured life and life predicted according to Li criterion for non-proportional tests [86].

GSE and GSA models:

The generalized strain energy (GSE) criterion was introduced by Ince and Glinka [71]. The GSE damage parameter adds elastic and plastic shear strain energy together with elastic and plastic normal strain energy. It takes into account the effects of mean stress and non-proportional hardening through elastic energy terms by including the maximum shear and normal stress. Shear energy terms are expected to represent the initiation and propagation of fatigue crack. Normal energy terms, on the other hand, are supposed to reflect the acceleration of the fatigue crack growth. The critical plane is defined as the plane where generalized strain energy (the left side of Eq. 14) reaches the maximum value.

$$\left(\tau_{max}\frac{\Delta\gamma^{e}}{2}+\frac{\Delta\tau}{2}\frac{\Delta\gamma^{p}}{2}+\sigma_{n,max}\frac{\Delta\varepsilon_{n}^{e}}{2}+\frac{\Delta\sigma_{n}}{2}\frac{\Delta\varepsilon_{n}^{p}}{2}\right)_{max}=\frac{\sigma_{f}'^{2}}{E}(2N_{f})^{b}+\sigma_{f}'\varepsilon_{f}'(2N_{f})^{c}, \qquad (14)$$

where τ_{max} is the maximum shear stress, $\Delta\gamma^{e}$ is a range of elastic shear strain, $\Delta\gamma^{p}$ is a range of plastic shear strain, $\Delta\varepsilon_{n}^{e}$ a range of elastic normal strain, $\Delta\varepsilon_{n}^{p}$ is a range of plastic normal strain, $\Delta\tau$ is a range of shear stress and $\Delta\sigma_{n}$ is a range of normal stress.

Authors Ince and Glinka [71] also developed the generalized strain amplitude (GSA) damage parameter. It was obtained by modification of their GSE damage parameter. Shear strain energy terms of the GSE damage parameter were normalized by factor $\Delta\tau/2$ whereas normal strain energy terms were normalized with factor $\Delta\sigma_n/2$. When further assumptions described in [71] were taken into account, the criterion can be described with Eq. 15. The interpretation of individual terms included in the left side of Eq. 15 is the following: elastic shear strain term helps to overcome sliding forces between crack surfaces, plastic shear strain initiate fatigue cracks by inducing dislocations along slip planes, elastic normal strain term accelerates the crack growth by opening the crack and plastic normal strain which causes a reduction of friction forces between crack surfaces by opening the crack. The critical plane is defined in the same way as in the case of the GSE model – the plane where the damage parameter reaches the maximum value.

$$\left(\frac{\tau_{max}}{\tau_f'}\frac{\Delta\gamma^e}{2}+\frac{\Delta\gamma^p}{2}+\frac{\sigma_{n,max}}{\sigma_f'}\frac{\Delta\varepsilon_n^e}{2}+\frac{\Delta\varepsilon_n^p}{2}\right)_{max}=\frac{\sigma_f'}{E}(2N_f)^b+\varepsilon_f'(2N_f)^c \tag{15}$$

The authors performed a series of proportional and non-proportional fatigue life tests using specimens from 1045 steel. They subsequently compared experimental and predicted fatigue lives and concluded that most of the predictions were within the factor-three-band (Fig. 16). They also revealed that the GSE model tends to overestimate fatigue lives greater than 10^5 meanwhile GSA model produced slightly conservative predictions for proportional loading.

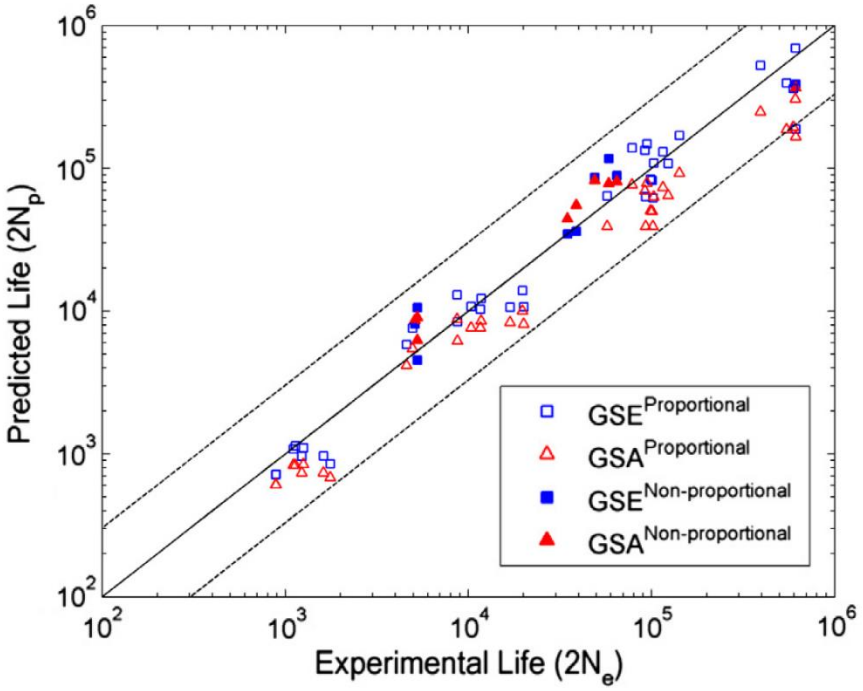

Fig. 16 Comparison of measured life and life predicted according to GSE and GSA criteria [71].

MGSE Yu model:

Modifications of the GSE damage parameter were proposed by Yu et al. [72] as it was found to have a limited ability to accurately predict the fatigue life in situations of pure shear loading and multiaxial loading governed predominantly by shear stresses. The MGSE criterion takes into account both shear and normal strain energy, as shown in Eq. 16. Shear strain energy is indicative of the crack initiation, while normal strain energy expresses the crack growth.

$$\tau_{max}\frac{\Delta\gamma}{2}+\sigma_{n,max}\frac{\Delta\varepsilon}{2}=\frac{\tau_f'^2}{G}(2N_f)^{2b_0}+\tau_f'\gamma_f'(2N_f)^{b_0+c_0} \tag{16}$$

The critical plane is located near the plane experiencing the maximum shear strain. The described approach can be used for most materials that are ductile and undergo shear cracking [72]. Since the maximum normal and shear stress are involved in the damage parameter, the model can take into account the influence of both mean stresses - normal and shear. The model's precision was tested when the fatigue endurance of titanium alloy TC4 was predicted. Data presented in Fig. 17 were obtained from symmetrical loading tests. Predictions corresponding to non-proportional loading proved to be over-conservative.

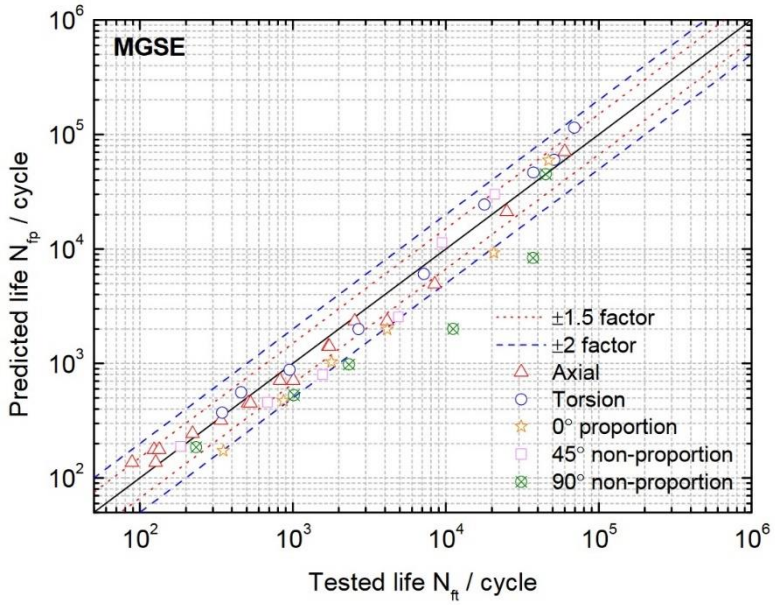

Fig. 17 Comparison of measured life and life predicted according to MGSE criterion [72].

The authors also examined the ability of their model to predict fatigue life under asymmetrical loading. Most of the predictions were inside the factor-three-band. Their model produced more accurate predictions than the FS model, the authors explained it by the fact that the FS model is not able to take into account the effect of mean shear stress.

MGSE Zhu model:

Zhu et al. [73] pointed out that the modification of the GSE model proposed by Yu et al. [72] produced good life predictions only for ductile materials. They decided to further modify the MGSE criterion to make it more robust and able to predict fatigue endurance for various types of materials. They included an additional material parameter k_{MGSE} describing normal strain energy sensitivity and reflecting the impact of normal strain energy on crack growth. The authors claim that the inclusion of the additional parameter significantly enhanced the precision of fatigue life predictions. The model is described by Eq. 17.

$$\tau_{max}\frac{\Delta\gamma}{2} + k_{MGSE}\sigma_{n,max}\frac{\Delta\varepsilon_n}{2} = \frac{\tau_f'^2}{G}(2N_f)^{2b_0} + \tau_f'\gamma_f'(2N_f)^{b_0+c_0} \tag{17}$$

MSWT model:

Jiang [74] introduced a damage parameter derived from the SWT model. It may be seen on the left side of Eq. 18. Ma et al. [75] then defined a correlation between this damage parameter and the fatigue life which gives the MSWT model defined by Eq. 18. The parameter a_{MSWT} included in the model has to lie in an interval from 0 to 1 depending on the material. If the value of parameter a_{MSWT} is less than 0.37, the material exhibits shear cracking behavior, whereas a_{MSWT} value greater than 0.5 suggests tensile cracking behavior. When parameter a_{MSWT} falls within the range of 0.37 to 0.50, mixed cracking behavior is anticipated.

$$2a_{MSWT}\Delta\varepsilon\langle\sigma_{max}\rangle + \frac{1-a_{MSWT}}{2}\Delta\gamma\Delta\tau = 4a_{MSWT}\frac{\sigma_f'^2}{E}(2N_f)^{2b} + 4a_{MSWT}\sigma_f'\varepsilon_f'(2N_f)^{b+c} \quad (18)$$

MSWT and MGSE Zhu models were used for predicting the fatigue endurance of titanium alloy TC4 [73]. Obtained predictions are shown in Fig. 18. The MGSE Zhu model yields sufficiently precise predictions for torsional loading (all of them are inside the factor-two-band). On the contrary, the MSWT model tends to substantially overestimate the fatigue life under torsional loading, especially in the case of low amplitudes. The MGSE Zhu model seems to underestimate the fatigue endurance under 90° non-proportional loading, however, fatigue life predictions corresponding to 45° non-proportional loading fell inside the factor-two-band. The authors also predicted fatigue lives of sintered porous iron and concluded that the MSWT model produced significantly more accurate predictions.

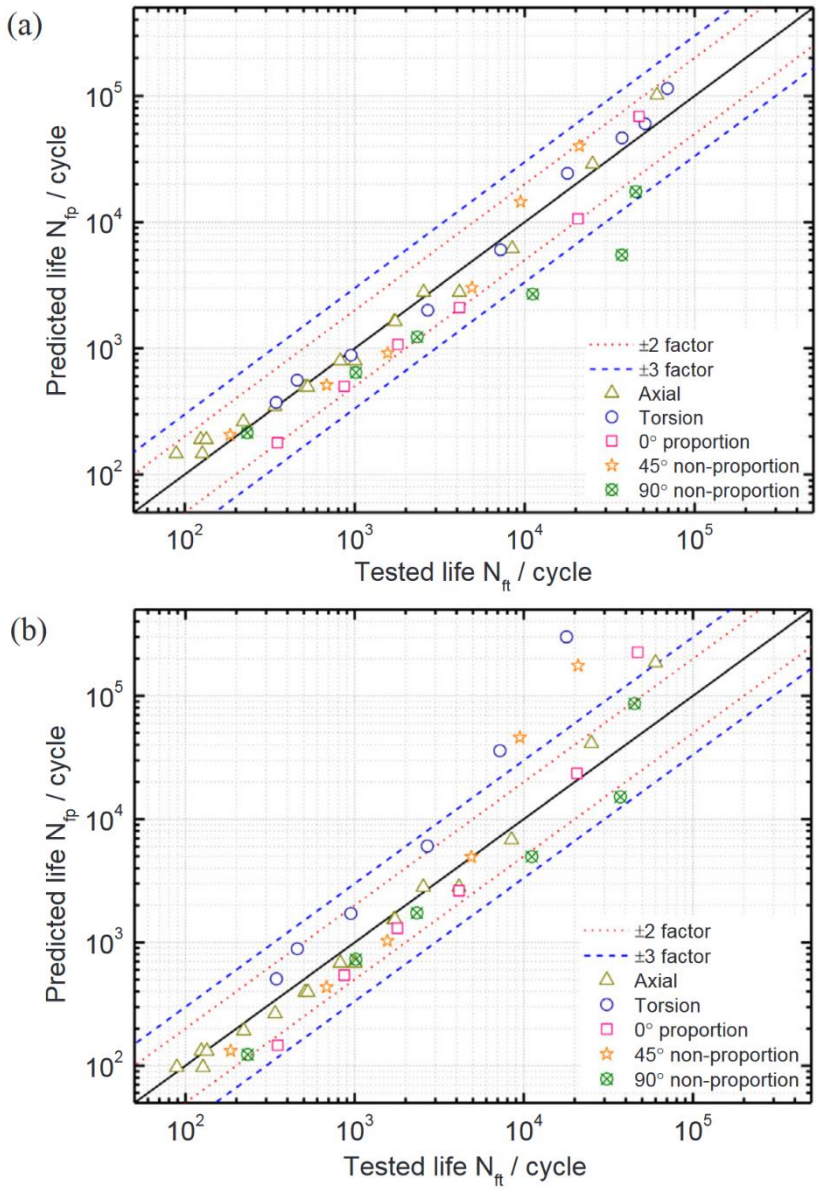

Fig. 18 Comparison of measured life and life predicted according to the (a) MGSE Zhu (b) MSWT criterion [73].

Chen model:

Two models based on energy density were introduced by authors Chen et al. [78]. The fundamental concept is that the material undergoes damage due to all the stresses and strains

applied on the critical plane. The first criterion, Chen I, applies to materials that have a tendency for tensile cracking and is expressed in Eq. 19. The second criterion, Chen II, is intended to be applied to materials with shear cracking behavior and is described by Eq. 20.

$$\Delta\varepsilon_1^{max}\Delta\sigma_1 + \Delta\gamma_1\Delta\tau_1 = 4\frac{\sigma_f'^2}{E}(2N_f)^{2b} + 4\sigma_f'\varepsilon_f'(2N_f)^{b+c}, \tag{19}$$

$$\Delta\gamma_{max}\Delta\tau + \Delta\varepsilon_n\Delta\sigma_n = 4\frac{\tau_f'^2}{G}(2N_f)^{2b_0} + 4\tau_f'\gamma_f'(2N_f)^{b_0+c_0}, \tag{20}$$

where $\Delta\varepsilon_1^{max}$ is a range of the maximum principle tensile strain, $\Delta\sigma_1$ is a range of normal stress on the maximum principle tensile strain plane, $\Delta\gamma_1$ is a range of shear strain on the maximum principle tensile strain plane, $\Delta\tau_1$ is a range of shear stress on the maximum principle tensile strain plane. In the case of proportional loading $\Delta\gamma_1$ and $\Delta\tau_1$ are equal to zero.

If a material with an unknown cracking behavior is analyzed, the authors recommend calculating the fatigue life using both criteria and selecting the more cautious prediction. The authors tried to predict fatigue lives of 45# and 42CrMo steel. The Chen I model proved to be more precise in the case of 45# steel while the Chen II model led to more accurate predictions when the fatigue endurance of 42CrMo steel was predicted. Both sets of predictions are depicted in Fig. 19

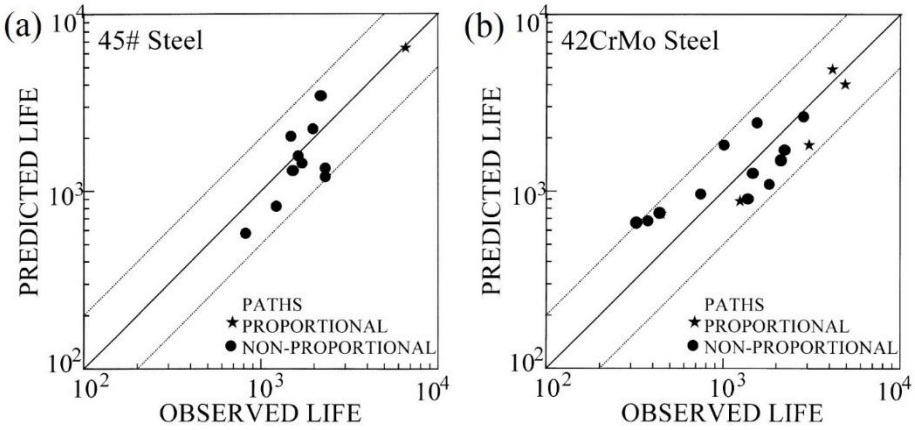

Fig. 19 Comparison of measured life and life predicted according to the (a) Chen I (b) Chen II criterion [78].

Liu model:

Liu's model [77] is similar to Chen's criteria as it also distinguishes between materials cracking according to Mode I and II. However, the distinction lies in the description of the critical plane. In the criterion denoted as Liu I (Eq. 21), which is designed for materials with Mode I cracking behavior, the critical plane is described as the plane with the maximum normal strain energy density. On the other hand, for materials cracking according to Mode II, the critical plane is defined as the plane with the maximum shear strain energy density. The model is then marked as Liu II and it is described by Eq. 22.

$$(\Delta\sigma_n\Delta\varepsilon_n)_{max} + (\Delta\gamma\Delta\tau) = 4\frac{\sigma_f'^2}{E}(2N_f)^{2b} + 4\sigma_f'\varepsilon_f'(2N_f)^{b+c} \tag{21}$$

$$(\Delta\sigma_n\Delta\varepsilon_n) + (\Delta\gamma\Delta\tau)_{max} = 4\frac{\tau_f'^2}{G}(2N_f)^{2b_0} + 4\tau_f'\gamma_f'(2N_f)^{b_0+c_0} \tag{22}$$

Zhu model:

The damage parameter in this model calculates the summation of elastic and plastic work per cycle for both normal and shear loading [76]. The damage parameter of this model may be thus

characterized as the cumulative work across all applied loading directions. The criterion is described by Eq. 23, it may be seen that a weighting factor ξ_{Zhu} is included. It is supposed to represent the damaging effect of shear loading. The value of the damage parameter ξ_{Zhu} depends on the cracking behavior of the material being analyzed. For materials exhibiting tensile cracking behavior, the value of ξ_{Zhu} is close to 0. In contrast, shear cracking materials require a value of ξ_{Zhu} that is close to 1.

$$\frac{\sigma_{max}^2}{2E} + \xi_{Zhu}\frac{\tau_{max}^2}{2G} + \Delta\sigma\Delta\varepsilon_p\frac{1-n'}{1+n'} + \xi_{Zhu}\Delta\tau\Delta\gamma_p\frac{1-n'}{1+n'} = \tag{23}$$
$$= \frac{\sigma_f'^2(2N_f)^{2b}}{2E} + \xi_{Zhu}\frac{\tau_f'^2(2N_f)^{2b_0}}{2G} + 4\frac{c-b}{c+b}[\sigma_f'\varepsilon_f'(2N_f)^{b+c} + \xi_{Zhu}\tau_f'\gamma_f'(2N_f)^{b_0+c_0}$$

Equations describing critical plane models chosen for the comparison in the present study are summarized in Tab. 2.

Tab. 2 Critical plane models

Model	Equation	Reference
BMC	$\varepsilon_{a,eq} = \frac{\sigma_f'}{E}(2N_f)^b + \varepsilon_f'(2N_f)^c$	-
WB	$\frac{\Delta\gamma}{2} + S\Delta\varepsilon_n = \left(1+\nu_e+S(1-\nu_e)\right)\frac{\sigma_f'}{E}(2N_f)^b + \left(1+\nu_p+S(1-\nu_p)\right)\varepsilon_f'(2N_f)^c$	[66]
FS	$\frac{\Delta\gamma}{2}\left(1+k\frac{\sigma_{n,max}}{\sigma_y}\right) = \frac{\tau_f'}{G}(2N_f)^{b_0} + \gamma_f'(2N_f)^{c_0}$	[69]
SWT	$\sigma_{n,max}\frac{\Delta\varepsilon_1}{2} = \frac{\sigma_f'^2}{E}(2N_f)^{2b} + \sigma_f'\varepsilon_f'(2N_f)^{b+c}$	[70]
MKBM	$\frac{\Delta\gamma}{2} + \left(1+\frac{\sigma_{n,max}}{\sigma_y}\right)\frac{\Delta\varepsilon_n}{2} = \left[\frac{\sigma_f'}{E}(2N_f)^b + \varepsilon_f'(2N_f)^c\right]\left(1+\frac{\sigma_f'}{\sigma_y}(2N_f)^b\right)$	[57]
Li	$\left(\frac{\Delta\tau_t}{2} + \lvert\tau_m\rvert\right)\frac{\Delta\gamma_{max}}{2} + L_{Li}\sigma_{n,max}\frac{\Delta\varepsilon_n}{2} = \frac{\tau_f'^2}{G}(2N_f)^{2b_0} + \tau_f'\gamma_f'(2N_f)^{b_0+c_0}$	[86]
GSA	$(\frac{\tau_{max}}{\tau_f'}\frac{\Delta\gamma^e}{2} + \frac{\Delta\gamma^p}{2} + \frac{\sigma_{n,max}}{\sigma_f'}\frac{\Delta\varepsilon_n^e}{2} + \frac{\Delta\varepsilon_n^p}{2})_{max} = \frac{\sigma_f'}{E}(2N_f)^b + \varepsilon_f'(2N_f)^c$	[71]
GSE	$(\tau_{max}\frac{\Delta\gamma^e}{2} + \frac{\Delta\tau}{2}\frac{\Delta\gamma^p}{2} + \sigma_{n,max}\frac{\Delta\varepsilon_n^e}{2} + \frac{\Delta\sigma_n}{2}\frac{\Delta\varepsilon_n^p}{2})_{max} = \frac{\sigma_f'^2}{E}(2N_f)^b + \sigma_f'\varepsilon_f'(2N_f)^c$	[71]
MGSE Yu	$\tau_{max}\frac{\Delta\gamma}{2} + \sigma_{n,max}\frac{\Delta\varepsilon}{2} = \frac{\tau_f'^2}{G}(2N_f)^{2b_0} + \tau_f'\gamma_f'(2N_f)^{b_0+c_0}$	[72]
MGSE Zhu	$\tau_{max}\frac{\Delta\gamma}{2} + k_{MGSE}\sigma_{n,max}\frac{\Delta\varepsilon_n}{2} = \frac{\tau_f'^2}{G}(2N_f)^{2b_0} + \tau_f'\gamma_f'(2N_f)^{b_0+c_0}$	[73]
MSWT	$2a_{MSWT}\Delta\varepsilon\langle\sigma_{max}\rangle + \frac{1-a_{MSWT}}{2}\Delta\gamma\Delta\tau = 4a_{MSWT}\frac{\sigma_f'^2}{E}(2N_f)^{2b} + 4a_{MSWT}\sigma_f'\varepsilon_f'(2N_f)^{b+c}$	[73]
Chen I	$\Delta\varepsilon_1^{max}\Delta\sigma_1 + \Delta\gamma_1\Delta\tau_1 = 4\frac{\sigma_f'^2}{E}(2N_f)^{2b} + 4\sigma_f'\varepsilon_f'(2N_f)^{b+c}$	[78]
Chen II	$\Delta\gamma_{max}\Delta\tau + \Delta\varepsilon_n\Delta\sigma_n = 4\frac{\tau_f'^2}{G}(2N_f)^{2b_0} + 4\tau_f'\gamma_f'(2N_f)^{b_0+c_0}$	[78]
Liu I	$(\Delta\sigma_n\Delta\varepsilon_n)_{max} + (\Delta\gamma\Delta\tau) = 4\frac{\sigma_f'^2}{E}(2N_f)^{2b} + 4\sigma_f'\varepsilon_f'(2N_f)^{b+c}$	[77]
Liu II	$(\Delta\sigma_n\Delta\varepsilon_n) + (\Delta\gamma\Delta\tau)_{max} = 4\frac{\tau_f'^2}{G}(2N_f)^{2b_0} + 4\tau_f'\gamma_f'(2N_f)^{b_0+c_0}$	[77]
Zhu	$\frac{\sigma_{max}^2}{2E} + \xi_{Zhu}\frac{\tau_{max}^2}{2G} + \Delta\sigma\Delta\varepsilon_p\frac{1-n'}{1+n'} + \xi_{Zhu}\Delta\tau\Delta\gamma_p\frac{1-n'}{1+n'} = \frac{\sigma_f'^2(2N_f)^{2b}}{2E} + \xi_{Zhu}\frac{\tau_f'^2(2N_f)^{2b_0}}{2G} + 4\frac{c-b}{c+b}[\sigma_f'\varepsilon_f'(2N_f)^{b+c} + \xi_{Zhu}\tau_f'\gamma_f'(2N_f)^{b_0+c_0}]$	[76]

2.2.2 Short fatigue cracks

The typical fatigue process can be divided into two phases – initiation and growth of fatigue crack. Crack growth is usually further separated into Stages I and II. Stage I means early growth of the crack along a slip band, i.e. along a plane with high shear stress. Stage II is characterized by the crack growth perpendicularly to maximum tensile stress – see Fig. 20. Selected issues concerning this topic are described in the following chapter.

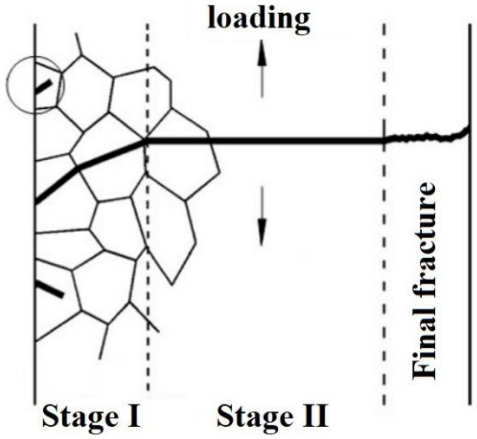

Fig. 20 Fatigue crack propagation stages.

Crack Type A and B

Brown and Miller suggested terms crack Type A and B (Fig. 21). Since they are frequently used by many authors it is appropriate to define them here as well. In the case of crack Type A, shear stress acts in the direction parallel to the crack length, and no shear acts along the crack depth. As a consequence, crack Type A is shallow and it is growing along the free surface. On the contrary, in the case of crack Type B, shear stress acts along the depth which results in the growth through the thickness. Crack Type B is therefore considered to be more dangerous. Which crack type is going to form is dependent mainly on the loading mode. Tension loading can lead to both types of crack, however, Karolczuk and Macha [81] conclude that Type A dominates in ductile material whereas Type B is characteristic for brittle materials. Torsion or tension/torsion loading always leads to Type A crack [99]. They also mention that ductile materials tend to crack according to Modes II and III whereas cracks in brittle materials tend to grow in Mode I.

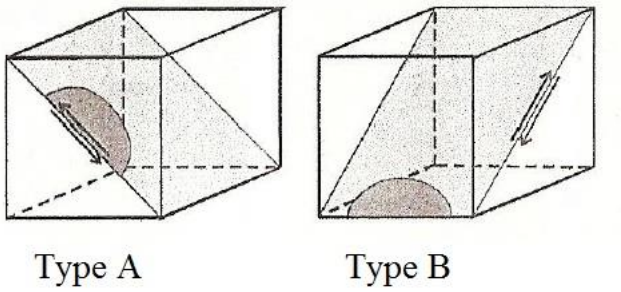

Fig. 21 Crack Type A and B [99].

Initiation of fatigue cracks

Mazánová et al. [59] investigated the mechanism of fatigue crack initiation in torsional, in-phase, and out-of-phase modes. Their experimental material was austenitic steel 316L. The sample from each loading mode exhibited a localization of plastic deformation into persistent

slip bands and a formation of persistent slip markings (PSM) on surface which turned out to be the initiation site of fatigue cracks. Fig. 22 represents a cut through PSM on the surface of the specimen cycled in in-phase mode, the cut was made by the focused ion beam technique (FIB). PSMs consist of extrusions and intrusions, the height of extrusions varies along the PSM length. Detail B revealed a crack initiated from the sharp intrusion, presumably on the (111) plane. The same mechanism was observed in torsional and out-of-phase modes.

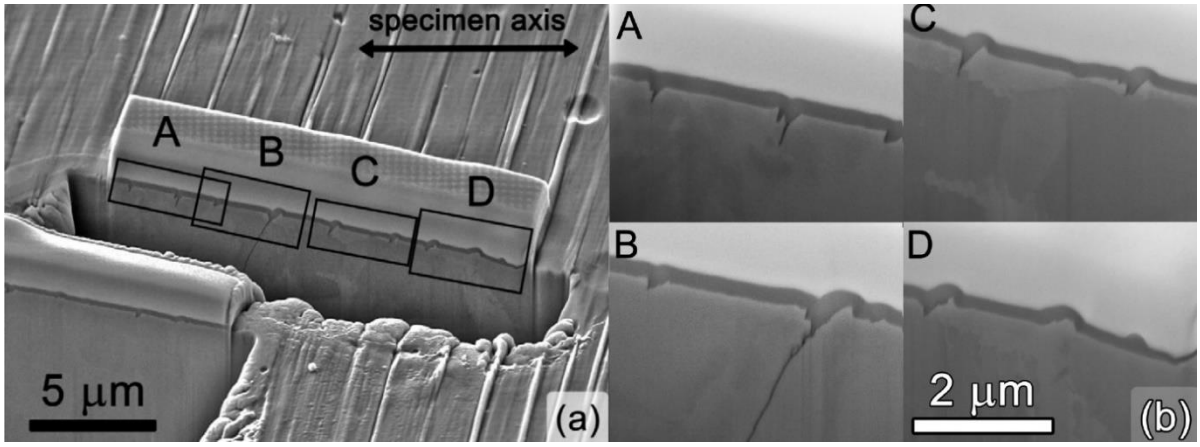

Fig. 22 (a) FIB cut through PSMs on specimen surface cycled in in-phase mode with equivalent strain amplitude 4.2×10^{-3} (b) details of PSM profiles and initiated cracks [59].

Crack orientation

Bannantine and Socie performed a complex study regarding the fatigue crack orientation in torsional mode [100]. They prepared a series of tests with various amplitudes on austenitic steel 304. Results are summarized in form of a damage map in Fig. 23. Cracking behavior is categorized here into two regions – A and B which are separated by the dashed line. Region A corresponds to the crack growth on planes with maximum shear stress (Mode II), meanwhile, region B represents the crack growth on planes with maximum principal strain (Mode I). As can be seen, shear cracks were observed in the case of high amplitudes (short fatigue lives), and tensile cracks developed in specimens cycled with low amplitude (long fatigue lives). Characteristics of region A are a high density of cracks, fast nucleation, a small number of branched cracks, and main crack growth by linking of previously initiated cracks. Regions B features are the following: reduced number of cracks, a larger portion of fatigue life spent in the nucleation period, and cracks initiated on shear planes but quickly branched into principle planes. Branched cracks further grew by propagation rather than linking small cracks.

Sakane and Itoh [101] performed a detailed study of the transition area outlined by the dashed line in Fig. 23. They found that cracks developed in this range of amplitude consisted of central shear crack (Mode II) which branches at both ends into two tensile cracks (Mode I). The length of the central shear crack is increasing with increasing strain amplitude. The limits of the transition area were roughly estimated in terms of strain amplitude range as 2.1×10^{-2} and 2.6×10^{-2}. Further crack observations revealed the fact that shear cracks propagate near the specimen surface meanwhile tensile cracks extends deeper into the specimen.

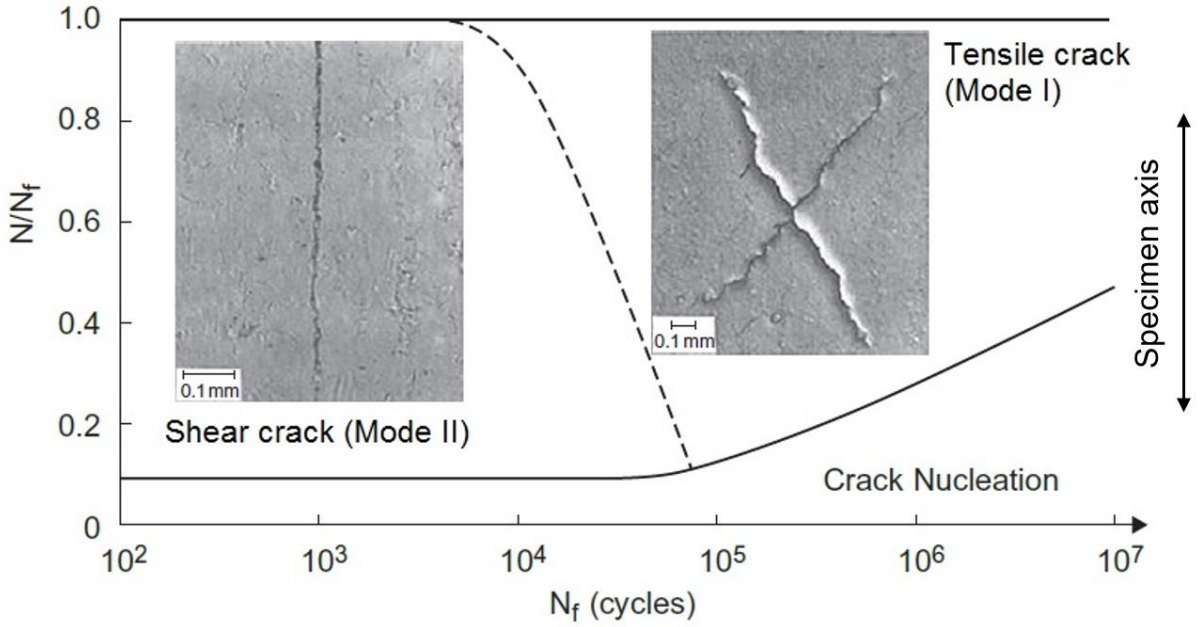

Fig. 23 Crack path map of 304 steel fatigued in torsional mode [99].

Bannantine and Socie [100] defined the damage map also for tensile mode, they found out that cracks grow always in Mode I regardless of the amplitude. The nucleation period of axial mode is significantly longer compared to torsional (in terms of N/N_f). Even in the case of very high amplitudes ($N_f = 10^2$) the number of cycles corresponding to the crack nucleation exceeded half of the total fatigue life (0.5 N/N_f). Such behavior may be interpreted as follows: cyclic loading in torsional mode is characteristic for a short portion of fatigue life spent in the nucleation period, subsequent crack growth is therefore substantially slower. On the contrary, cycling in axial mode results in later nucleation and faster propagation of fatigue crack.

The aforementioned research of Mazánová et al. [59] was also aimed at studying the directions of cracks developed during in-phase, out-of-phase, and torsional loading. Observations of the torsional specimen surface revealed cracks consisting of a short central part with a direction close to maximum shear stress (Mode II). The crack bifurcated during its further growth and two cracks on both ends formed. The direction of branched cracks coincided with the direction of maximum principal strain (Mode I). This observation is in agreement with the results from Sakane and Itoh [101]. In-phase loading resulted in the growth of cracks whose direction was corresponding to the plane of maximum shear stress. Cracks are initiated usually inside the grain. As the crack grew, it ran into the grain boundary and a small tendency to bifurcation appeared. However, the crack was just locally bent and continued in the same direction. The bending at the intersection of two grains was usually accompanied by the initiation of a secondary small crack whose length was negligible. Cracks observed in out-of-phase mode exhibited the same features as those in in-phase mode. Any cruciform cracks were observed neither in in-phase nor in out-of-phase mode. The substantial difference was in the density of cracks and their growth rate. Out-of-phase mode produced fewer cracks however their growth was faster [59].

Crack deflection and branching

Sistaninia and Niffenegger [102] observed a significant decrease in stress intensity factor after branching which resulted in a decrease of crack growth rate. Research by Qian et al. [103] was focused on the cycling of pre-cracked specimens in Mode II and mixed Mode. They concluded that branching occurred in all studied cases. Calculations of the stress intensity factor revealed that branched cracks grew in Mode I. They outlined a possible reason for crack Mode II

bifurcation: friction force between Mode II crack surfaces reduces Mode II stress intensity factor. Micro-cracks developed inside the so-called damage zone located around the crack tip represent possible nucleation sites for branching.

Even though there are crack directions that are characteristic of particular loading conditions, the real crack path may be significantly different. The reason is that it can be influenced by far-field stress, variable loading amplitude in form of overload, embrittlement from an aggressive environment, or by an interaction of crack tip with structural inhomogeneities (grain boundaries, precipitates, etc.). The stress intensity factor of deflected crack can be considerably lower (just like in the case of branched cracks) compared to a straight crack with the same length. Repeated changes in the crack path, therefore, lead to a slower crack growth rate and longer fatigue life. The crack deflection also causes an increase in surface roughness which promotes the crack closure effect during unloading, as a consequence, the crack growth rate is further suppressed [104].

An example of a branched and deflected crack may be seen in Fig. 24. It was captured by SEM after 5100 loading cycles of austenitic-ferritic duplex steel SAF 2507. The growing crack was branched after approximately 500 cycles at location A. Another branching occurred after 3800 cycles at location B. There is also well-visible deflection at location C. The observed branching and deflection are caused by the microstructure. The crack propagated transgranular within ferritic grains. The distribution of austenite in the ferritic matrix was not homogeneous and when the crack tip encountered an austenitic dominant region, the crack path was significantly deflected or branched [105].

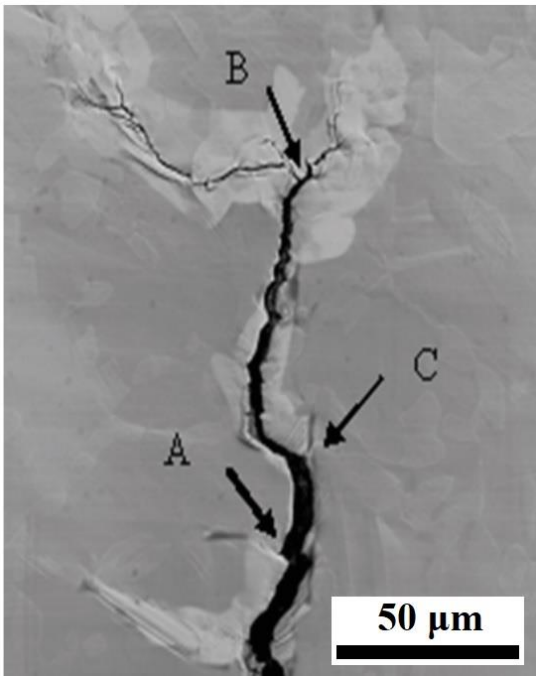

Fig. 24 Fatigue crack path in austenitic-ferritic duplex steel [105].

Description of short fatigue crack growth kinetics

It is a well-known fact, that the crack propagation stage plays a minor role in high cycle fatigue régime since most of the lifetime is consumed by the crack initiation. The plastic zone at the crack tip is small (comparable to the grain size) and small-scale yielding conditions are fulfilled. The stress intensity factor range ΔK and the Paris-Erdogan law are commonly applied to describe fatigue crack propagation.

The situation is however different in the case of low cycle fatigue. The plastic zone is substantially larger and the linear elastic fracture mechanics is not valid. Two elastic-plastic fracture mechanics concepts have been successfully adopted for the description of fatigue crack growth under conditions of large-scale yielding: crack tip opening displacement (CTOD) and J-integral. The length of the propagation stage in low cycle fatigue is comparable to the initiation period when smooth specimens are examined. Cycling of notched specimens may even cause the crack growth stage becomes dominant. It is therefore of considerable interest to find a tool enabling analyzing and predicting the growth of fatigue crack.

Jíša et al. [106] applied a crack growth analysis initially proposed by Polák and Zezulka [107], they fitted the exponential dependence of the crack length *a* on the number of loading cycles *N* with a power law. Their experimental data were acquired from cyclic loading of wrought aluminum alloy EN-AW 6082. Three stress amplitudes and two specimen directions (longitudinal *L* and transverse *T*) were examined. Their results led them to a presumption that the crack growth rate *da/dN* increases linearly with *a*. The obtained crack growth coefficient k_g corresponds to the relative increment of the crack length after applying one loading cycle. The authors declared that the value of coefficient k_g is determined by plastic strain amplitude and loading conditions (*R* ratio and temperature). When k_g was plotted against plastic strain amplitude measured at the half-life $\varepsilon_{ap\ 0.5Nf}$, all data points could be reasonably approximated with a power law, and two material parameters defining the growth of small fatigue cracks were derived – k_{g0} and *d*.

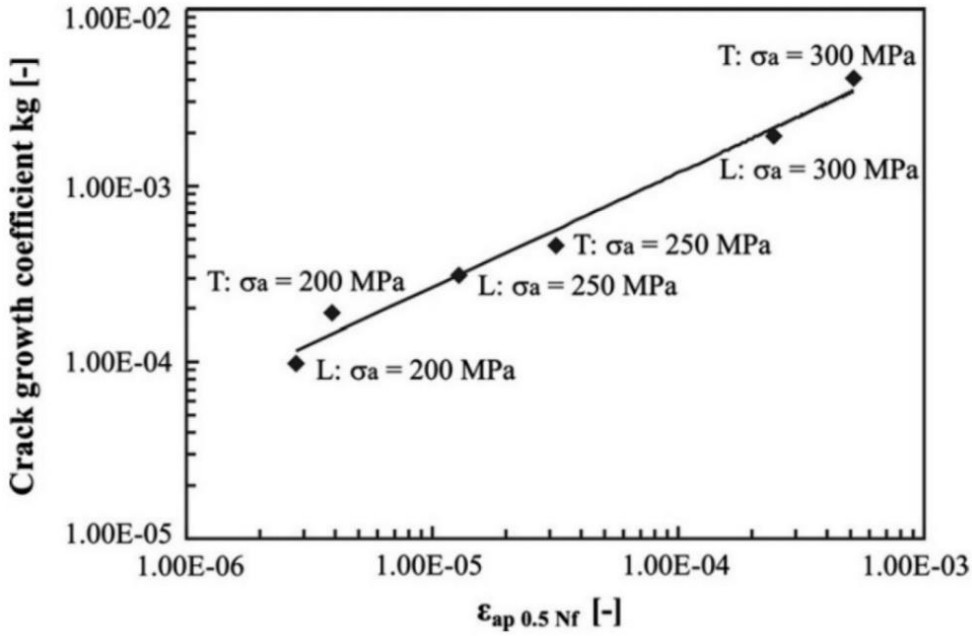

Fig. 25 Crack growth coefficient k_g as a function of plastic strain amplitude measured at half-life $\varepsilon_{ap\ 0.5\ Nf}$ [106].

It was confirmed that the fatigue crack growth mechanism requires cyclic plastic deformation near the crack tip [108]. Since the CTOD, originally proposed by Burdekin and Stone [109], measures a displacement near the crack tip and hence provides a characterization of the crack tip strain field, it was utilized to describe the fatigue crack propagation rate. Dong et al. [110] introduced an analytical model giving a linear correlation between the crack growth rate *da/dN* and *ΔCTOD*. Their model was verified using experimental data acquired from cycling a sample of Q345 steel. Vasco-Olmo et al. [111] and Antunes et al. [112] suggested using only the plastic part of CTOD. This approach offers certain benefits – the crack closure effect is included and the elastic part of CTOD which is not supposed to contribute to the crack growth is excluded.

The *da/dN* - $\Delta CTOD_p$ model is a material property and its independence on loading conditions was confirmed by Vasco-Olmo et al. [111] by receiving the same linear relationship for two *R* ratios – see Fig. 26.

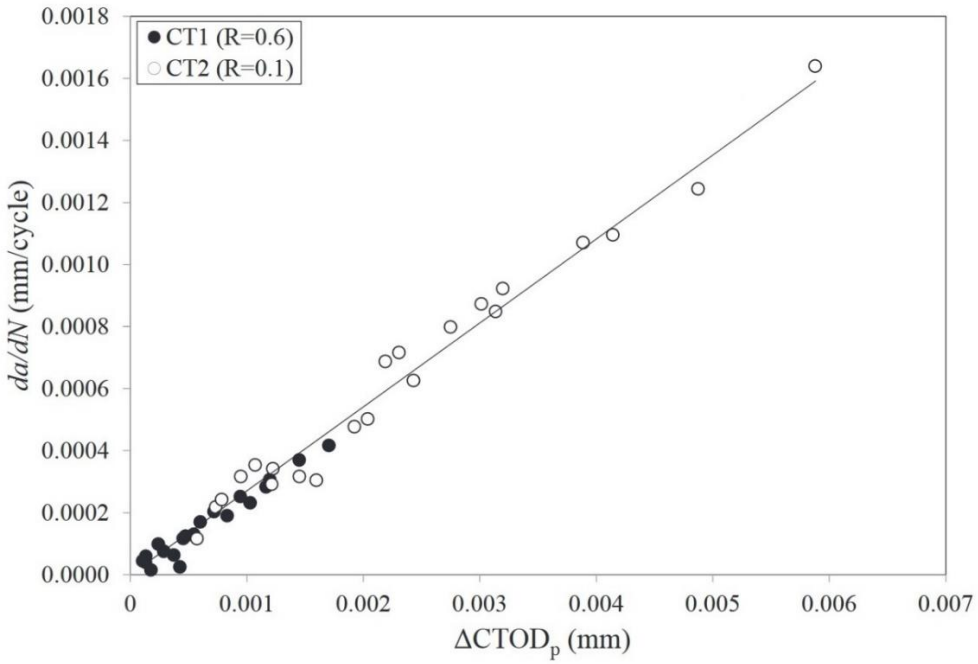

Fig. 26 Linear dependence of da/dN on $\Delta CTOD_p$ *for two stress ratios [111].*

Another characterizing parameter correlating the crack growth rate under large-scale yielding is the J-integral. The application of this fracture mechanics concept for the fatigue crack growth analysis was studied by Beretta et al. [113] and Rabbolini et al. [114] who utilized a range of total J-integral. Further studies of Hutař et al. [115, 116] however revealed that using the amplitude of the plastic part of J-integral $J_{a,pl}$ generated a better description of the crack growth propagation than the amplitude of total J-integral J_a. It is well demonstrated in Fig. 27 where data from cyclic straining with five loading levels of austenitic-ferritic duplex steel 2205 are examined. There is a visible difference among fitting curves of particular strain amplitudes when J_a is applied while all data can be reasonably fitted with a unique curve in the case of $J_{a,pl}$.

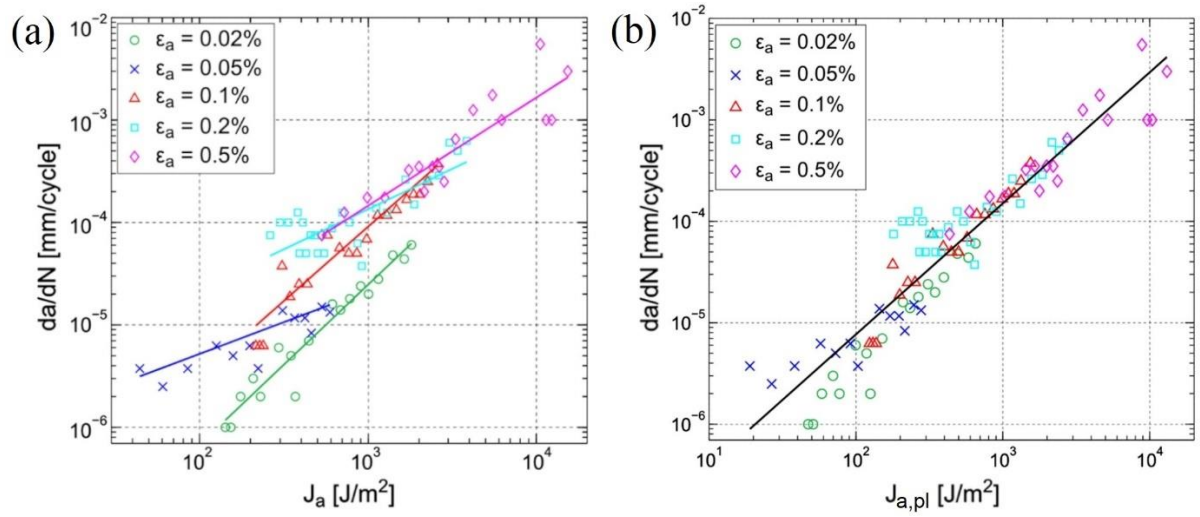

Fig. 27 Dependence of da/dN on the amplitude of (a) total J-integral (b) plastic part of J-integral. Data were measured on samples from austenitic-ferritic duplex steel 2205 [115].

3 Main goals of the Thesis

1. Performing systematic fatigue tests on smooth bodies for determining the fatigue life, cyclic stress-strain curves, and cyclic hardening-softening behavior in uniaxial, torsional, in-phase, and out-of-phase axial/torsional cycling;
2. comparison of the accuracy of existing fatigue life models based on the critical plane approach;
3. measuring the kinetics of fatigue crack growth on designated specimens using the same loading modes and strain amplitudes as the fatigue life tests;
4. assessing the existing methods of crack growth analyses;
5. evaluation of phase stability of 316L steel in conditions of various loading modes;
6. observation and analysis of microstructural changes in multiaxial fatigue, especially the formation of dislocation structures;
7. discussing the macroscopic fatigue behavior and fatigue life in relation to the microstructure, its evolution and to the fatigue crack growth kinetics.

4 Description of the experiment

4.1 Experimental material

Austenitic stainless steel 316L was chosen as an experimental material for the present study. The steel was delivered as 20 mm thick hot rolled sheets. Fig. 28 shows the microstructure resulting from color etching, which consists primarily of austenitic grains that are equiaxial in shape and have an average size of around 40 μm. However, a few delta ferrite bands can be seen as well (gray lines in Fig. 28).

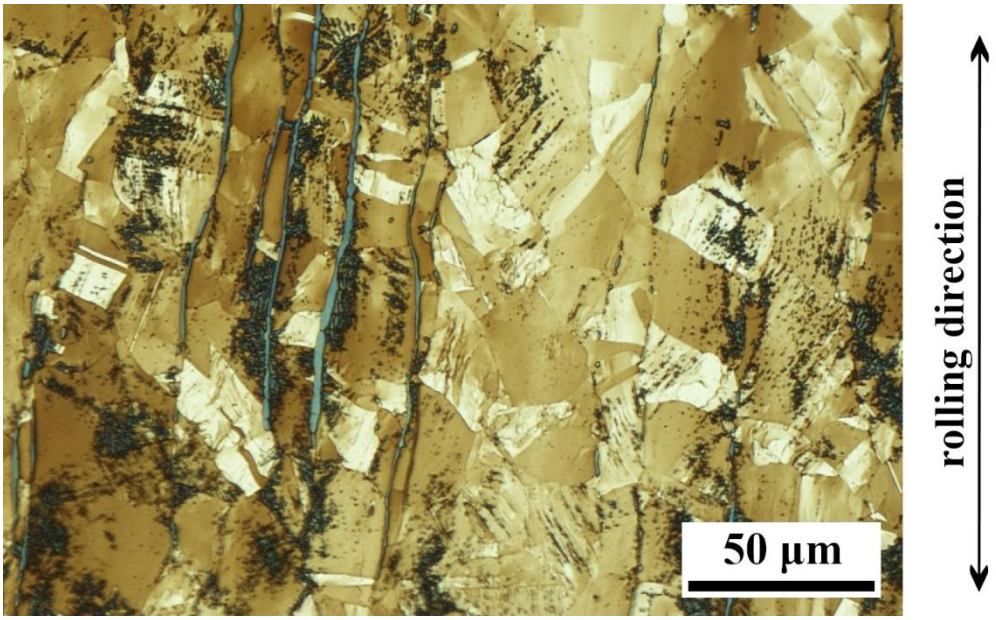

Fig. 28 Color etched microstructure of 316L steel.

The manufacturer - Acerinox company guaranteed the following mechanical properties: 0.2 % proof stress $R_{p0,2}$ = 336 MPa, ultimate tensile stress R_m = 586 MPa, and fracture elongation A = 57 %. Tab. 3 contains information regarding the chemical composition of the material. Based on the values listed in this table we can say that the most important alloying elements of 316L steel are chromium, nickel, molybdenum, and manganese.

Tab. 3: The chemical composition of austenitic steel 316L in wt. %.

C	Cr	Mn	Mo	N	Ni	P	S	Si	Fe
0.018	16.631	1.261	2.044	0.042	10.000	0.032	0.001	0.380	bal.

4.2 Geometry of specimens

Specimens designed for our experiments had a cylindrical shape and were machined from the sheet without any following heat treatment. The specimen axis coincides with the rolling direction. As can be seen in Fig. 29, two specimen types were designed. The inner hole was fabricated by spark erosion technique. Specimen (a) was used for fatigue life (FL) tests and specimen (b) for crack growth rate (CGR) tests. The only difference between them is a hole with a diameter 0.3 mm fabricated in the middle of the gauge length by an electro-erosion. The gauge section's exterior surface underwent mechanical grinding and subsequent electrolytic polishing.

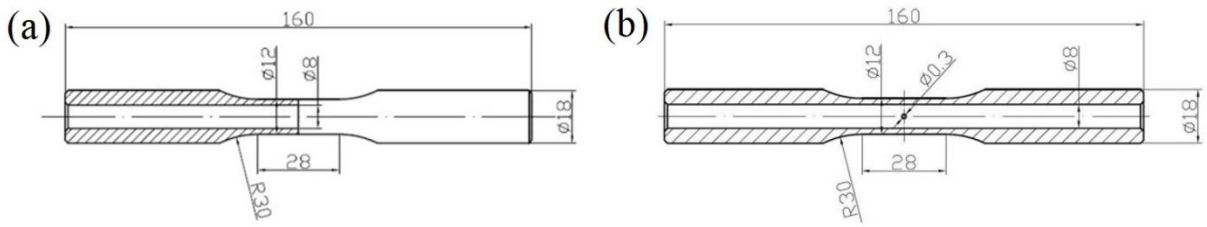

Fig. 29 Design of specimens used for (a) fatigue life tests; (b) crack growth rate tests.

FL tests were performed to obtain essential fatigue characteristics such as the S-N curve, Manson-Coffin curve, cyclic stress-strain curve, and cyclic hardening/softening curves. Results from FL tests are going to be used for the prediction of fatigue life by critical plane models. The main purpose of CGR tests is to measure the kinetics of small fatigue crack growth. As mentioned before, specimens designed for CGR tests had a small hole in the gauge length. This hole served as an artificial crack starter for CGR tests. Light microscope Navitar was aimed at the hole and micrographs of the growing crack were taken regularly after a certain number of cycles. The crack length *a* was determined as shown in Fig. 30. It equals half of the distance connecting both ends of the crack. Another output of CGR tests was the angle of crack deflection α measured at the moment when the crack length surpassed 1000 μm. Measured angles were subsequently compared with predictions based on critical plane models.

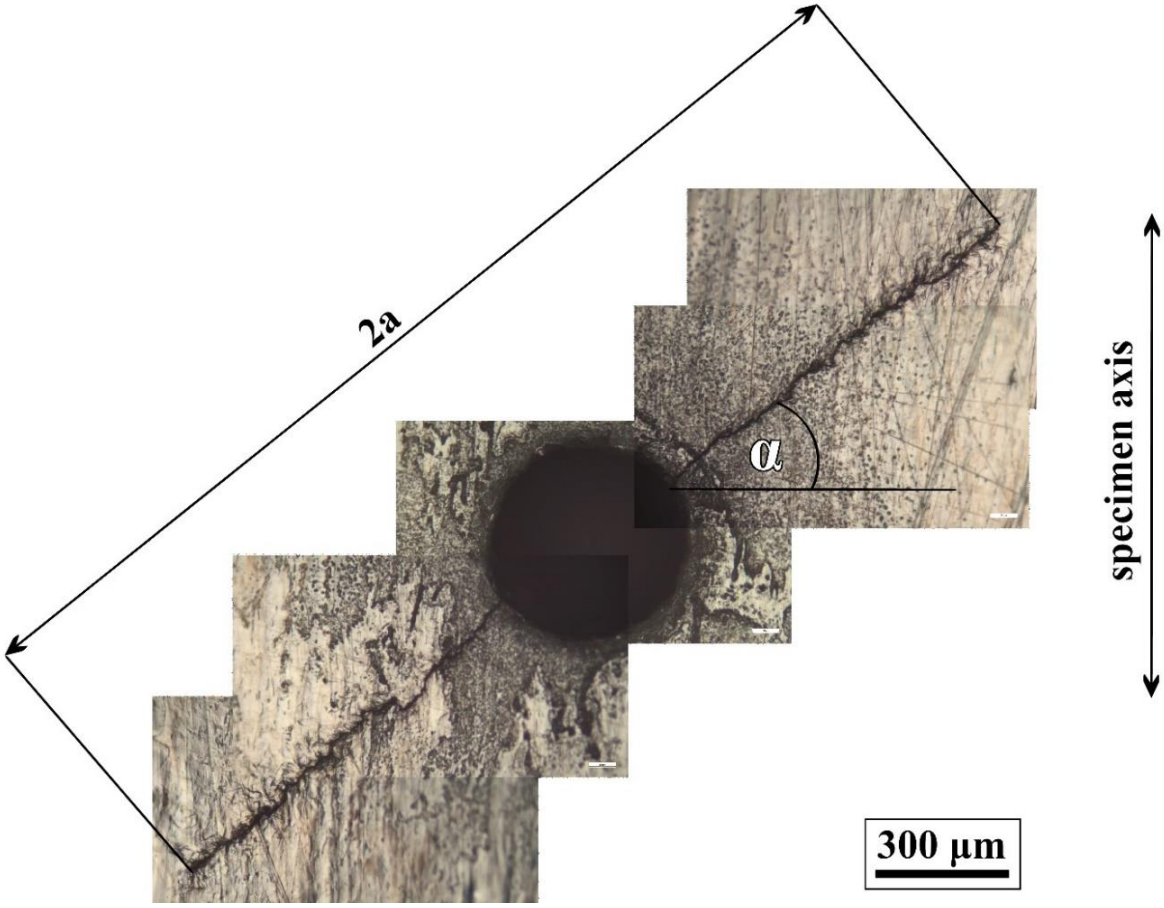

Fig. 30 Micrograph of artificial crack starter with growing fatigue crack.

4.3 Loading conditions

Both types of tests were performed in the following loading modes:

- Axial mode (A)
- Torsional mode (T)
- Axial/torsional in-phase mode (IP)
- Axial/torsional 90° out-of-phase mode (OP)

They are outlined in Fig. 31 in ε_a-γ_a coordinates, ε_a represents the amplitude of normal strain controlled in the A-test while γ_a is the shear strain amplitude in the T-test.

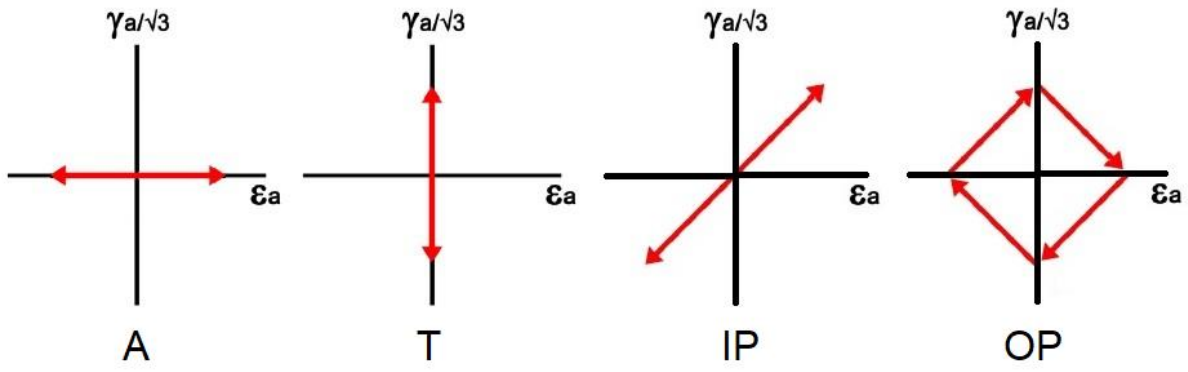

Fig. 31 Testing modes in ε - γ coordinates.

The ratio between the axial and torsional strain components ε_a and $\gamma_a/\sqrt{3}$, respectively, which is defined as the A/T ratio, was equal to 1 for the majority of tests in IP and OP loading modes. However, for equivalent strain amplitude $\varepsilon_{a,eq}$ = 0.44 %, five different A/T ratios were selected, they may be found in Tab. 6.

All tests were performed at ambient temperature, in symmetrical total strain controlled mode with a constant equivalent strain rate equal to 3×10^{-3} s^{-1} (the definition of equivalent strain is provided in the following section). The value of strain rate had to be chosen considering the relatively low thermal conductivity of 316L steel. The temperature of the sample was measured by thermocouple and the cooling of grips was adapted to keep the sample temperature constant, approximately 23° C. Tests were performed on the machine MTS 809 which enables independent and combined cycling in tension/compression and torsion. The strain was measured by a combined axial–torsional extensometer and the amplitude of the total equivalent strain was controlled.

In strain-controlled fatigue, it is necessary to choose a criterion for the end of fatigue life. When the principal crack develops in A, IP, and OP cycling, the stress maximum in the tensile half cycle decreases. The fatigue life N_f was equal to the number of cycles when:

$$\left|\frac{\sigma_{max}}{\sigma_{min}}\right| < -0.9 \tag{24}$$

Since the maximum and minimum of shear stress were usually decreasing at the same rate in T-tests, it was necessary to use another approach. The fatigue life in T-tests was equal to the number of cycles when the stress amplitude τ_a decreased to 90 % of the maximum shear stress amplitude determined in the secondary hardening phase τ_{SHmax} , i.e.:

$$\frac{\tau_a}{\tau_{SHmax}} < 0.9 \tag{25}$$

4.4 Equivalent strain and stress

To compare results from various loading paths, it is a common practice to simplify the characterization of full strain and stress tensors into a single scalar value, known as equivalent strain ε_{eq} and equivalent stress $\sigma_{eq.}$ The von Mises formula was utilized to determine the

amplitudes of equivalent strain and stress for each loading mode, which can be found in Tab. 4. The procedure is however more complex when dealing with OP mode since the maximum axial and torsional strain and stress occur at different times. To calculate the equivalent stress amplitude, one must use the amplitude of normal stress σ_a and the shear stress τ_{corr}, which corresponds to the moment of maximum normal stress. Since IP and OP loading paths have the same length in schematics in Fig. 31, it is assumed that it is acceptable to use the same equation for determining the amplitude of equivalent strain in both loading modes [32].

Tab. 4 Equivalent strain and stress amplitudes for applied loading paths.

	A	T	IP	OP
$\varepsilon_{a,eq}$	ε_a	$\frac{\gamma_a}{\sqrt{3}}$	$\sqrt{\varepsilon_a^2 + \gamma_a^2/3}$	$\sqrt{\varepsilon_a^2 + \gamma_a^2/3}$
$\sigma_{a,eq}$	σ_a	$\tau_a\sqrt{3}$	$\sqrt{\sigma_a^2 + 3\tau_a^2}$	$\sqrt{\sigma_a^2 + 3\tau_{corr}^2}$

The equivalent plastic strain amplitude $\varepsilon_{ap,eq}$ for A, T, and IP modes was ascertained by taking half the width of the hysteresis loop depicted in equivalent coordinates, as shown in Fig. 32.

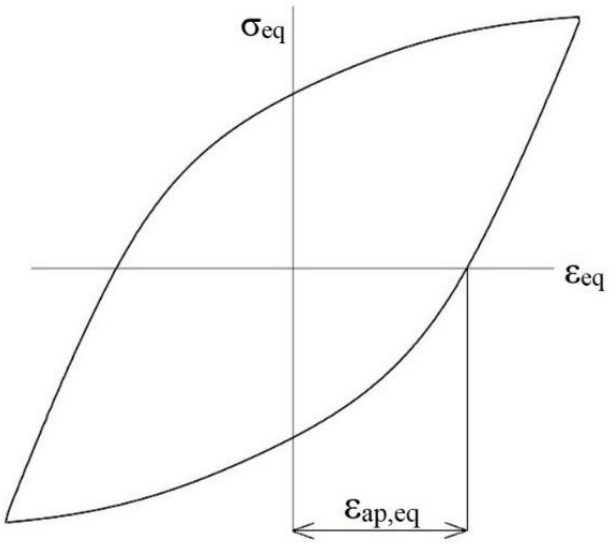

Fig. 32 Determining of $\varepsilon_{ap,eq}$ from equivalent hysteresis loop.

For OP mode, a different method was employed to compute the plastic strain amplitude, involving the use of Eq. 26, which involved subtracting the elastic equivalent strain amplitude from the total equivalent strain amplitude. The effective Young's modulus E_{eff} was determined using the elastic slope of the very first half cycle of the IP test.

$$\varepsilon_{ap,eq} = \varepsilon_{a,eq} - \frac{\sigma_{a,eq}}{E_{eff}} \tag{26}$$

4.5 Microstructural analysis

Transmission electron microscope JEOL JEM-2100F was used for the microstructural description, in particular for studying α′ martensite formation and dislocation structures developed during cyclic loading. Oriented foils determined for TEM observations were prepared in the following manner. A thin plate parallel to the specimen axis was cut from the fatigue specimen gauge length by an electric discharge machine. The plate was subsequently mechanically ground until its thickness reached approximately 0.1 mm. A disc of 3 mm diameter was punched out of the plate afterward. The disc was electrolytically polished using the TenuPol device. The electropolished disc was fixed in a TEM holder concerning its

orientation. The specimen was observed using classical TEM mode or STEM mode with the bright (BF) and high angle annular dark field (HAADF) detectors. Phase analysis and crystallographic orientation of grains were done using diffraction patterns and Kikuchi lines.

The phase stability of austenite was tested after the end of chosen fatigue life tests. The specimens were first analyzed with the Feritscope Fischer MP30. The measurements were performed at a reasonable distance from the fracture surface where no signs of plastic deformation due to the magistral crack propagation were apparent and no macroscopic crack was visible. The content of α′ martensite was systematically measured on twelve equidistant spots around the perimeter of the gauge length and an arithmetic mean of measured values was calculated afterward. An appropriate correction factor dependent on the specimen geometry was provided by the manufacturer.

The same fatigue life specimens were cut in the gauge length area for the SEM observation. Two cuts perpendicular to the specimen axis were performed and a 10 mm height cylinder was uniaxially pressed into the mounting material so the surface perpendicular to the specimen axis could be observed. The mounted specimen was then mechanically ground, polished with oxide polishing suspension as well as electrolytically. The scanning electron microscope Tescan Lyra 3 XMU FEG was used for the EBSD analysis to quantify the process of strain induced martensitic transformation and to map the distribution of newly formed α′ martensite.

4.6 Critical plane models

A survey of the literature was performed and fifteen critical plane models were applied to predict the fatigue life of 316L steel. The purpose was to discover which model generates the most precise predictions compared to experimental data. Another purpose was to reveal whether models containing additional material parameter yield better predictions than those without the parameter. The precision of predictions was evaluated with the error ER defined by Eqs. (27) and (28). ER larger than 100 % means that the data point is outside the factor-two-band.

$$\mathrm{ER} = 100 \times \frac{\mathrm{N_f predicted} - \mathrm{N_f observed}}{\mathrm{N_f observed}} \quad \text{if } \mathrm{N_f} \text{ predicted} > \mathrm{N_f} \text{ observed} \tag{27}$$

$$\mathrm{ER} = 100 \times \frac{\mathrm{N_f observed} - \mathrm{N_f predicted}}{\mathrm{N_f predicted}} \quad \text{if } \mathrm{N_f} \text{ predicted} < \mathrm{N_f} \text{ observed} \tag{28}$$

As already mentioned, some criteria in Tab. 2 include an additional material parameter. Its value was obtained by fitting the experimental data. The fitting process was performed to acquire the smallest achievable average error AER defined by Eq. 29.

$$\mathrm{AER} = \frac{1}{\mathrm{n}} \sum_{\mathrm{i}=1}^{\mathrm{n}} \mathrm{ER_i} \tag{29}$$

As the gauge length of the specimen used in this study has the form of a thin-walled tube, a state of plane stress is assumed. Eqs. 30 - 33 can be used to calculate the normal and shear stress and strain on any plane inclined at an angle α at a given time t. Fig. 33 explains the terms used in Eqs. 30 - 33.

$$\sigma_\alpha(t) = \frac{\sigma_x(t)}{2} + \frac{\sigma_x(t)}{2}\cos(2\alpha) + \tau_{xy}(t)\sin(2\alpha) \tag{30}$$

$$\tau_\alpha(t) = \frac{\sigma_x(t)}{2}\sin(2\alpha) - \tau_{xy}(t)\cos(2\alpha) \tag{31}$$

$$\varepsilon_\alpha(t) = \frac{(1-\nu_{eff})}{2}\varepsilon_x(t) + \frac{(1+\nu_{eff})}{2}\varepsilon_x(t)\cos(2\alpha) + \frac{\gamma_{xy}(t)}{2}\sin(2\alpha) \tag{32}$$

$$\gamma_\alpha(t) = \left(1+\nu_{eff}\right)\varepsilon_x(t)\sin(2\alpha) - \gamma_{xy}(t)\cos(2\alpha) \tag{33}$$

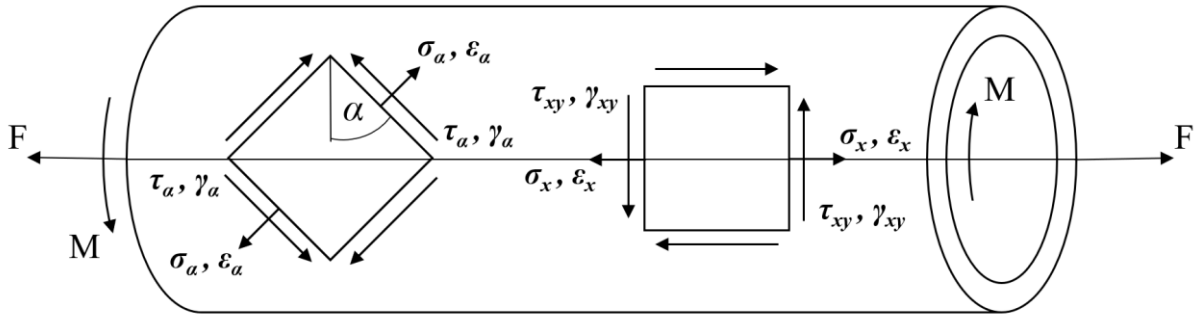

Fig. 33 Stresses and strains of thin-walled specimen. [117]

The value of the effective Poisson's ratio ν_{eff} was determined using Eq. 34, with elastic and plastic Poisson's ratios of 0.3 and 0.5, respectively.

$$\nu_{eff} = \frac{\nu_e \varepsilon_e + \nu_p \varepsilon_p}{\varepsilon_e + \varepsilon_p} \tag{34}$$

The process of analyzing stress-strain conditions and the following determination of the critical plane involved separating each loading into 400 data points. Normal/shear stress/strain on the given plane inclined by angle α were computed for each data point using Eqs. 30 - 33. This procedure was performed for every plane in the range from 0° to 180°. Similarly, the damage parameter, whose definition depends on the life predicting model, was also calculated for each plane in this range. The critical plane was localized based on the chosen model. It is typically defined as the plane with the maximum damage parameter/shear strain/principal strain, etc.

4.7 Finite element analysis

The concept of plastic J-integral J_p was adopted for the analysis of fatigue crack kinetics. The dependence of J_p on crack length a was determined using extensive finite element modeling which takes into account non-linear material behavior under large-scale yielding. The 3D modeling was performed in ANSYS software and its detailed description may be found in [118].

To assess J_p, two individual issues were addressed. The initial step involved solving the linear model with a linear elastic material model to obtain the elastic component of J-integral J_{el}. The second step involved solving the elastic-plastic model derived from the cyclic stress-strain curve to acquire the total J-integral J_{total} which is the sum of J_{el} and J_p. The desired J_p could be therefore determined from Eq. 35.

$$J_p = J_{total} - J_{el} \tag{35}$$

The analysis was performed for several crack lengths according to experimental data. Four strain amplitudes from A, T, and IP loading modes listed in Tab. 5 were examined.

Tab. 5 Equivalent strain amplitudes $\varepsilon_{a,eq}$ [%] of specimens evaluated using J_p concept.

A	T	IP
0.33	0.28	0.24
0.44	0.37	0.28
0.55	0.44	0.44
0.75	0.55	0.55

5 Results

The chapter is divided into five sections. The first section is devoted to the response of the material to cyclic deformation that is presented in form of Manson-Coffin, S-N, hardening/softening, and cyclic stress-strain curves. The second section is dealing with the microstructural characterization of specimens subjected to fatigue life tests. Selected specimens were analyzed by EBSD and TEM techniques. Results of crack growth rate kinetics are shown in the section three. Crack growth is characterized by the coefficient k_g and by the plastic part of the J-integral. The last two sections are aimed at critical plane models. Predictions of fatigue life and crack orientation are presented in particular.

5.1 Fatigue life tests

A list of performed fatigue life tests along with their parameters and results is shown in Tab. 6. It is worth noting that IP and OP tests with $\varepsilon_{a,eq} = 0.44$ % were conducted with five various A/T ratios.

Tab. 6 List of performed fatigue life tests.

mode	A/T	$\varepsilon_{a.eq}$ [%]	ε_a [%]	γ_a [%]	$\varepsilon_{ap.eq}$ [%]	$\sigma_{a.eq}$ [MPa]	σ_a [MPa]	τ_a [MPa]	N_f [-]
A	100/0	0.249	0.249	0	0.085	307	307	0	208 687
	100/0	0.279	0.279	0	0.112	311	311	0	37 635
	100/0	0.319	0.319	0	0.145	320	320	0	25 154
	100/0	0.369	0.369	0	0.186	333	333	0	18 522
	100/0	0.427	0.427	0	0.236	346	346	0	10 088
	100/0	0.439	0.439	0	0.245	350	350	0	7 846
	100/0	0.549	0.549	0	0.338	373	373	0	3 950
	100/0	0.748	0.748	0	0.510	408	408	0	1 715
	100/0	0.997	0.997	0	0.729	451	451	0	1 001
T	0/100	0.200	0	0.347	0.048	316	0	182	705 000+
	0/100	0.234	0	0.406	0.071	336	0	194	548 820
	0/100	0.239	0	0.415	0.077	332	0	192	346 210
	0/100	0.278	0	0.482	0.108	346	0	200	200 690
	0/100	0.320	0	0.555	0.145	354	0	205	100 340
	0/100	0.349	0	0.604	0.170	359	0	207	77 212
	0/100	0.440	0	0.762	0.251	383	0	221	28 365
	0/100	0.568	0	0.984	0.349	424	0	245	15 100
	0/100	0.750	0	1.299	0.506	460	0	266	6 260
	0/100	0.750	0	1.299	0.515	463	0	268	5 057
	0/100	0.797	0	1.381	0.569	423	0	244	6 950
	0/100	1.008	0	1.746	0.735	512	0	296	2 807
IP	50/50	0.239	0.170	0.291	0.081	319	222	132	68 223
	50/50	0.273	0.197	0.329	0.111	320	226	131	51 466
	50/50	0.319	0.227	0.388	0.146	334	241	134	26 079
	50/50	0.348	0.248	0.423	0.173	341	249	134	19 206
	27/73	0.437	0.154	0.708	0.249	362	131	195	17 596

	46/54	0.438	0.286	0.575	0.248	357	235	155	12 534
	50/50	0.433	0.312	0.522	0.245	351	253	141	11 410
	65/35	0.441	0.388	0.364	0.245	353	311	97	13 640
	80/20	0.441	0.428	0.185	0.261	334	325	43	7 454
	50/50	0.501	0.354	0.613	0.303	374	273	147	7 000
	50/50	0.568	0.404	0.692	0.358	385	283	151	6 900
	50/50	0.754	0.531	0.928	0.523	431	310	173	2 892
	50/50	0.848	0.600	1.039	0.608	432	319	168	1 966
	50/50	0.999	0.707	1.221	0.735	471	344	186	1 650
OP	50/50	0.239	0.169	0.293	0.092	297	294	183	73 736
	50/50	0.280	0.198	0.342	0.125	321	318	198	48 375
	50/50	0.320	0.226	0.392	0.158	339	331	208	39 254
	50/50	0.350	0.247	0.428	0.176	363	355	223	24 276
	27/73	0.442	0.152	0.719	0.281	339	262	233	20 113
	46/54	0.441	0.285	0.582	0.239	426	404	263	9 517
	50/50	0.440	0.312	0.538	0.235	423	410	259	10 492
	65/35	0.440	0.388	0.361	0.241	398	395	213	11 695
	80/20	0.440	0.428	0.181	0.268	346	346	114	11 544
	50/50	0.570	0.404	0.698	0.339	490	464	292	5 524
	50/50	0.753	0.532	0.923	0.485	557	525	325	3 054
	50/50	1.007	0.707	1.242	0.690	667	630	398	1 378

** + run-out test*

5.1.1 Fatigue life curves

The most basic result of fatigue life tests is a dependence of the number of cycles to fracture on total equivalent strain amplitude (controlled parameter of fatigue life tests) and it is shown in Fig. 34. It can be seen that the highest numbers of cycles to fracture were obtained in T-tests. On the other hand, the shortest fatigue lives were observed in A mode. Fatigue lives in T mode are approximately five times longer in the case of low amplitudes although the difference is getting smaller with increasing amplitude and the ratio is around three in the case of high amplitudes. Curves representing IP and OP mode lie between A and T curves although they are much closer to the A curve and all three of them overlap with decreasing value of total strain amplitude.

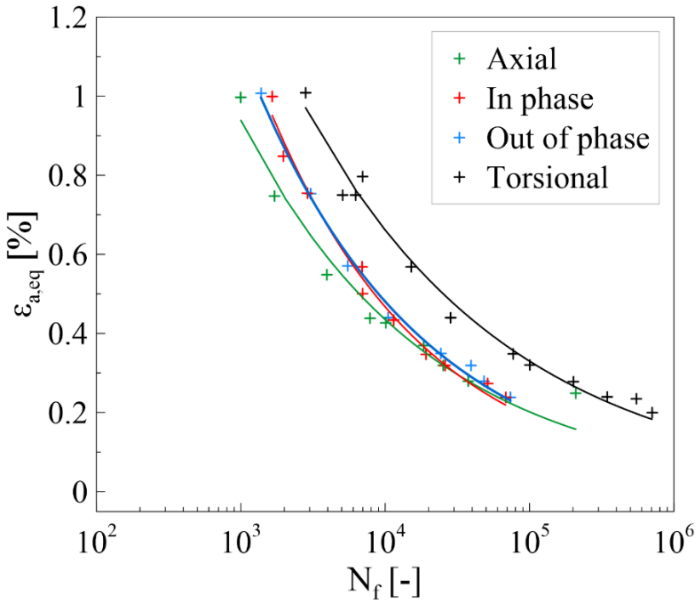

Fig. 34 Number of cycles to fracture as a function of total equivalent strain amplitude [117].

5.1.2 Cyclic hardening-softening curves

An evolution of equivalent stress amplitude during the fatigue life can be seen in Fig. 35. Four amplitudes from every loading mode were chosen to demonstrate that the material response is dependent on the type of loading as well as on the applied strain amplitude. The same three phases of fatigue life may be identified in most cases, their intensity is; however, distinct. There is a primary cyclic hardening caused by an increasing dislocation density. The phase of primary hardening is very short, in fact, it did not exceed one hundred loading cycles in any test. In the following softening phase, the stress amplitude is continuously decreasing with the increasing number of cycles. The cyclic softening is supposed to be caused by a formation of dislocation structures which require a lower applied stress needed for the movement of dislocations. The softening phase ends when the phase transformation of metastable austenite results in secondary cyclic hardening.

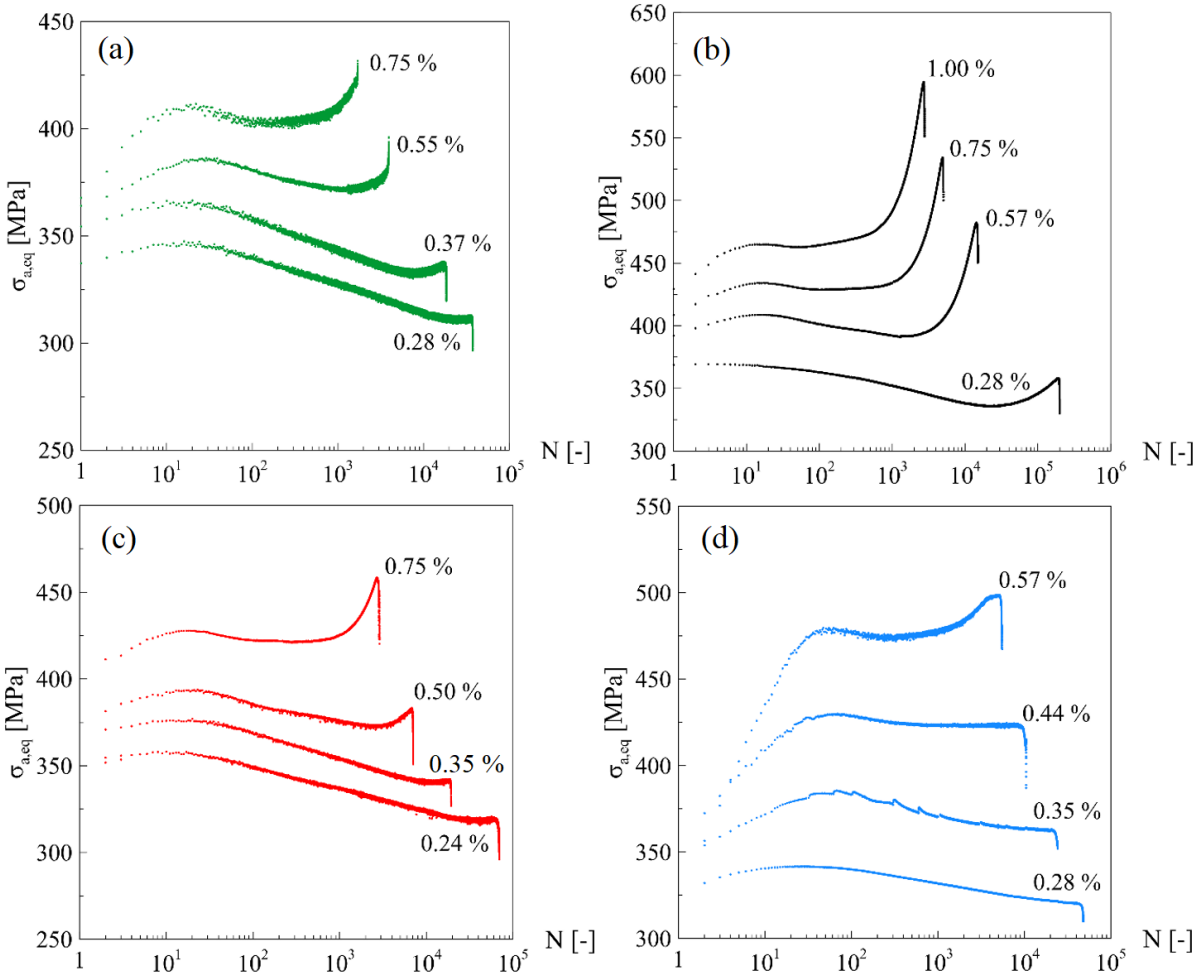

Fig. 35 Hardening-softening curves obtained from (a) A (b) T (c) IP (d) OP fatigue life tests.

Fig. 36 shows a comparison of hardening-softening curves obtained from different loading modes with the same $\varepsilon_{a,eq}$, particularly speaking about amplitudes 0.28 %; 0.44 %; 0.57 %, and 1.00 %. Curves corresponding to cycling in A and IP mode with $\varepsilon_{a,eq}$ = 0.28 % are close to each other and their shape is comparable, the only difference is more intense secondary hardening in IP mode. OP curve is close to A and IP curves but there are few distinctions – the primary hardening phase lasts longer, softening is less intense and there is no secondary hardening. The curve representing T mode is above the rest. Its characteristic feature is no primary hardening and significantly more intense secondary hardening.

The situation is substantially different with increasing loading amplitude. The curve of OP mode is clearly above the other modes. It is caused by the primary hardening phase that is particularly intense and lasts longer when compared to other curves. A and IP modes exhibit almost the same behavior and their curves overlap in the case of $\varepsilon_{a,eq}$ = 0.44 % and $\varepsilon_{a,eq}$ = 1.00 %. There is a disparity of more intense secondary hardening observed in IP mode and a higher endurance against fracture. Increased $\varepsilon_{a,eq}$ also caused apparent primary hardening in T mode and secondary hardening in OP mode.

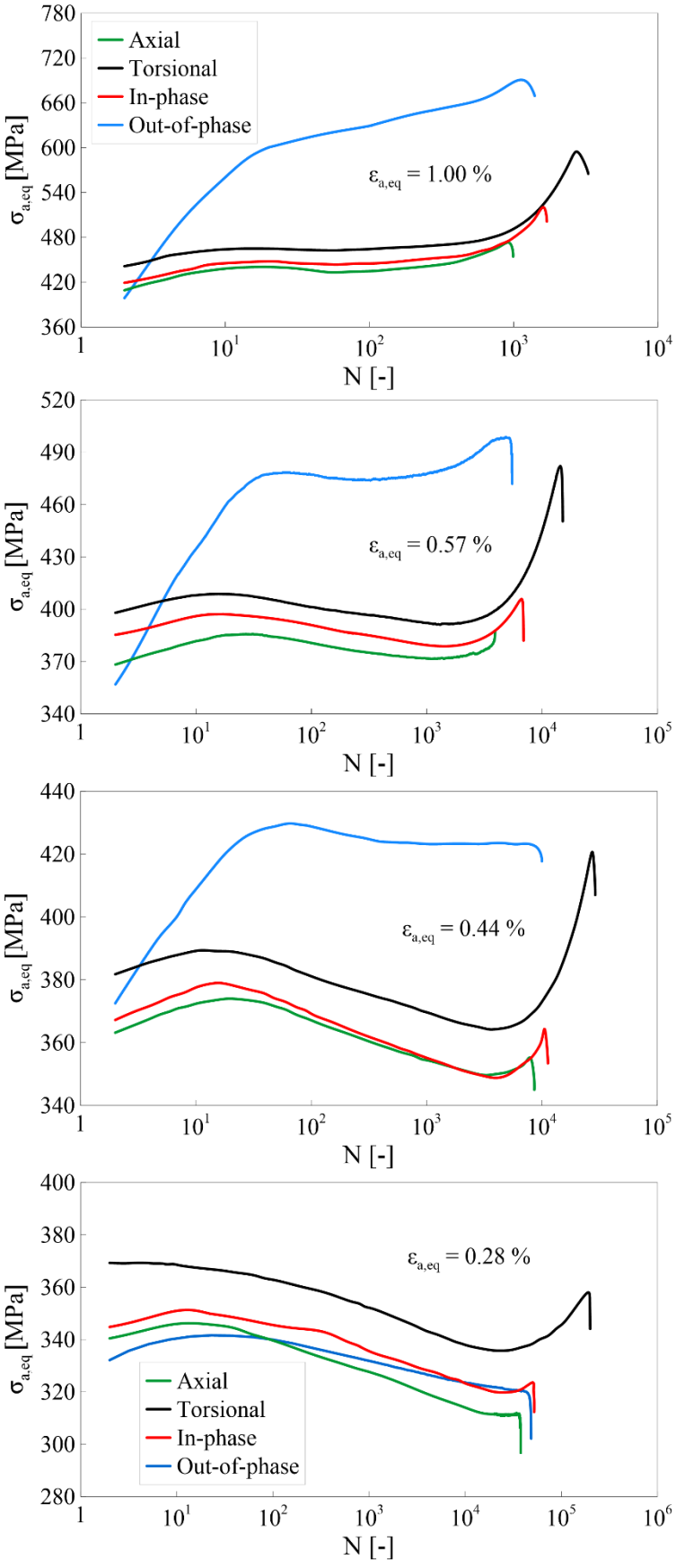

Fig. 36 Comparison of hardening-softening curves from tests with equivalent strain amplitudes $\varepsilon_{a,eq}$ 1.00 %; 0.57 %; 0.44 % and 0.28 %.

The intensity of particular fatigue life phases was quantified and is listed in Tab. 7. Following equations were used for the quantification:

$$PH_I = 100 \times \frac{\sigma_{maxPH} - \sigma_{fc}}{\sigma_{fc}} \tag{36}$$

$$S_I = 100 \times \frac{\sigma_{maxPH} - \sigma_{minS}}{\sigma_{maxPH}} \tag{37}$$

$$SH_I = 100 \times \frac{\sigma_{maxSH} - \sigma_{minS}}{\sigma_{minS}} \tag{38}$$

where PH_I is the intensity of primary hardening, S_I is the intensity of softening, SH_I is the intensity of secondary hardening, σ_{fc} is the equivalent stress amplitude in the very first loading cycle, σ_{maxPH} is the maximum equivalent stress amplitude during primary hardening, σ_{minS} is the minimum equivalent stress amplitude during softening and σ_{maxSH} is the maximum equivalent stress amplitude during secondary hardening – see Fig. 37.

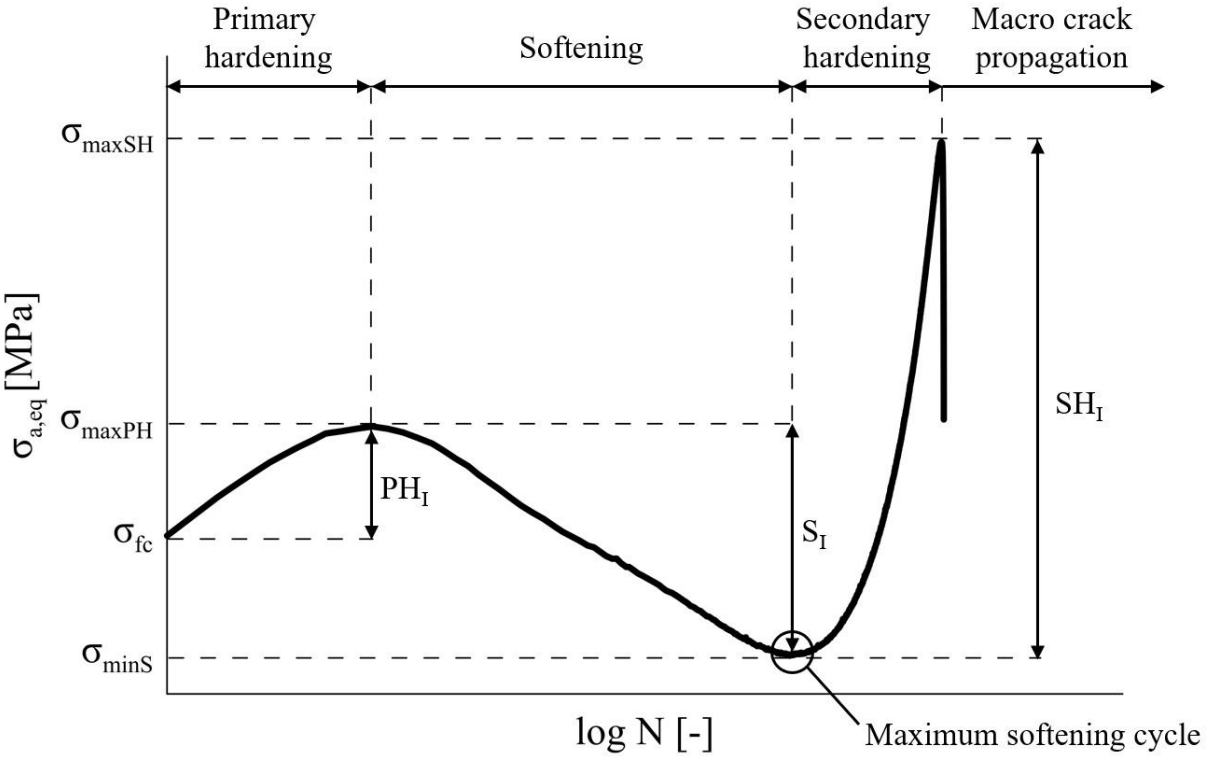

Fig. 37 Definition of fatigue life stages and maximum softening cycle.

Based on Fig. 36 and Tab. 7 it is obvious that there are common trends for every loading mode: PH_I as well as SH_I is getting larger with increasing $\varepsilon_{a,eq.}$ On the contrary, the softening phase is much more significant in the case of low amplitudes and the value of S_I goes down with increasing strain amplitude. S_I is almost negligible in the case of $\varepsilon_{a,eq}$ = 1.00 %. A combination of mentioned trends caused curves obtained from tests with high strain amplitudes reached their maximum value of $\sigma_{a,eq}$ just during the secondary hardening phase. On the other hand, curves corresponding to low strain amplitudes reached the maximum value of $\sigma_{a,eq}$ during the primary hardening phase.

The highest values of PH_I were observed in OP mode. The reason for this phenomenon is in activation of other slip systems that interact. It is also the reason for the less intense softening phase in OP mode because the formation of persistent slip bands is more difficult when more slip systems are active in each loading cycle. S_I in other loading modes reaches almost identical values.

The value of SH_I is dependent on the loading mode. The lowest SH_I was observed in A mode. On the other hand, the largest SH_I was measured in T mode. The superiority of secondary hardening in T mode can be well demonstrated by results obtained from tests with an equivalent strain amplitude of 0.44 %. Data from the OP test with this amplitude did not indicate any secondary hardening. Values of SH_I measured in A and IP were 1.4 % and 2.6 %, respectively. On the contrary, SH_I measured in T mode was 15.4 %. The difference between T and other loading modes gets lower in the case of an equivalent strain amplitude 1.00 %.

Tab. 7 The intensity of particular stages of fatigue life.

	A			T		
$\varepsilon_{a,eq}$ [%]	PH_I [%]	S_I [%]	SH_I [%]	PH_I [%]	S_I [%]	SH_I [%]
0.28	3.1	10.1	-	-	9.1	6.7
0.44	4.4	6.3	1.4	3.2	6.4	15.4
0.57	6.1	3.5	2.4	4.3	4.2	23.2
0.75	11.9	1.9	5.0	6.3	1.2	24.3
1.00	11.5	1.1	8.6	8.3	0.5	28.5

	IP			OP		
$\varepsilon_{a,eq}$ [%]	PH_I [%]	S_I [%]	SH_I [%]	PH_I [%]	S_I [%]	SH_I [%]
0.28	3.3	11.7	0.6	2.9	6.4	-
0.44	4.5	6.3	2.6	17.2	1.5	-
0.57	6.4	4.8	6.7	34.5	1.6	5.6
0.75	5.7	1.6	8.9	36.9	1.3	10.2
1.00	10.1	0.4	17.3	45.6	-	20.0

5.1.3 Manson-Coffin, S-N, and cyclic stress-strain curves

Since the tests were performed with a constant amplitude of total equivalent strain, the plastic strain amplitude and stress amplitude were changing during cycling as the material hardened or softened. Results in this section are depicted using data from both the half-life and maximum softening cycle. The maximum softening cycle was determined from the hardening-softening curve. It is defined as the cycle at the end of softening phase where the secondary hardening phase begins. It is marked by a circle in Fig. 37. Since the hardening-softening curve corresponding to the specimen cycled in OP mode with $\varepsilon_{a,eq}$ = 1.00 % did not show a sign of cyclic softening, this test is not included in the maximum softening versions of the following graphs.

Manson-Coffin curves are shown in Fig. 38. The situation here is very similar to fatigue life curves shown in Fig. 34. It means that the most damaging is cyclic loading in A mode while the least detrimental is T mode. IP and OP modes are between them but they are much closer to the A curve, especially in the case of low amplitudes.

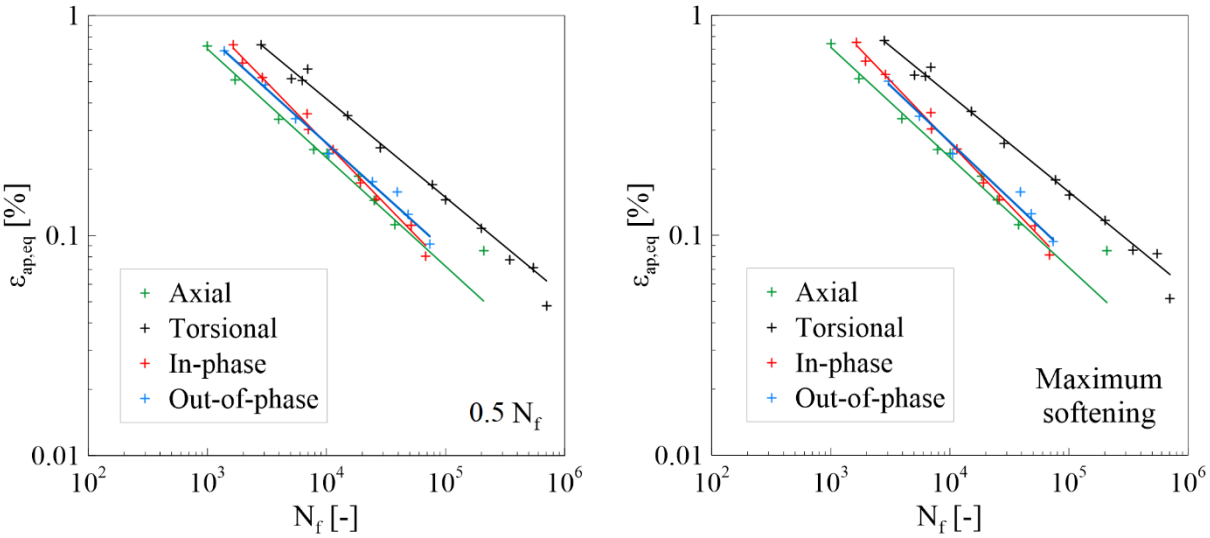

Fig. 38 Manson-Coffin curves based on half-life (left) and maximum softening cycles (right).

S-N curves are depicted in Fig. 39. Half-life curves of A and T modes exhibit a common trend. Meaning they have the same shape but T mode is shifted to longer fatigue lives. Datapoints of IP mode are almost identical to A mode in the case of low-stress amplitudes but A mode gets more detrimental with increasing stress amplitude. The material response to OP loading distinguishes significantly. The material is enduring to substantially higher stresses in the case of high $\varepsilon_{a,eq}$ (or low N_f), however, the difference gets lower with decreasing $\varepsilon_{a,eq}$ (increasing N_f) until OP, IP and A mode coincide. It is in agreement with the observation shown in Fig. 36: the material's response to cyclic loading in OP mode is similar to the other modes at low loading amplitudes but differs substantially for higher loading levels.

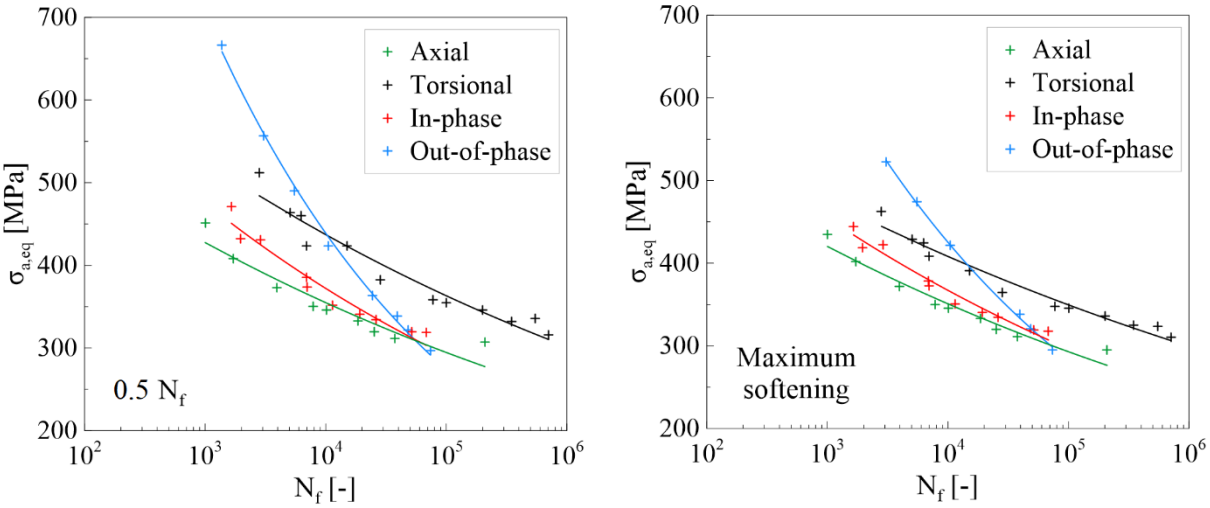

Fig. 39 S-N curves based on half-life (left) and maximum softening cycles (right).

Cyclic stress-strain curves (CSSC) are shown in Fig. 40. They can be well approximated by a power law (i.e. linear curves in a double logarithmic plot). Their arrangement is analogous to S-N curves, which means that A and IP modes are close to each other while the T mode is shifted. OP mode is essentially identical to A and IP modes in the region of low $\varepsilon_{ap,eq}$ but it reaches considerably higher stress amplitudes when higher $\varepsilon_{ap,eq}$ is applied.

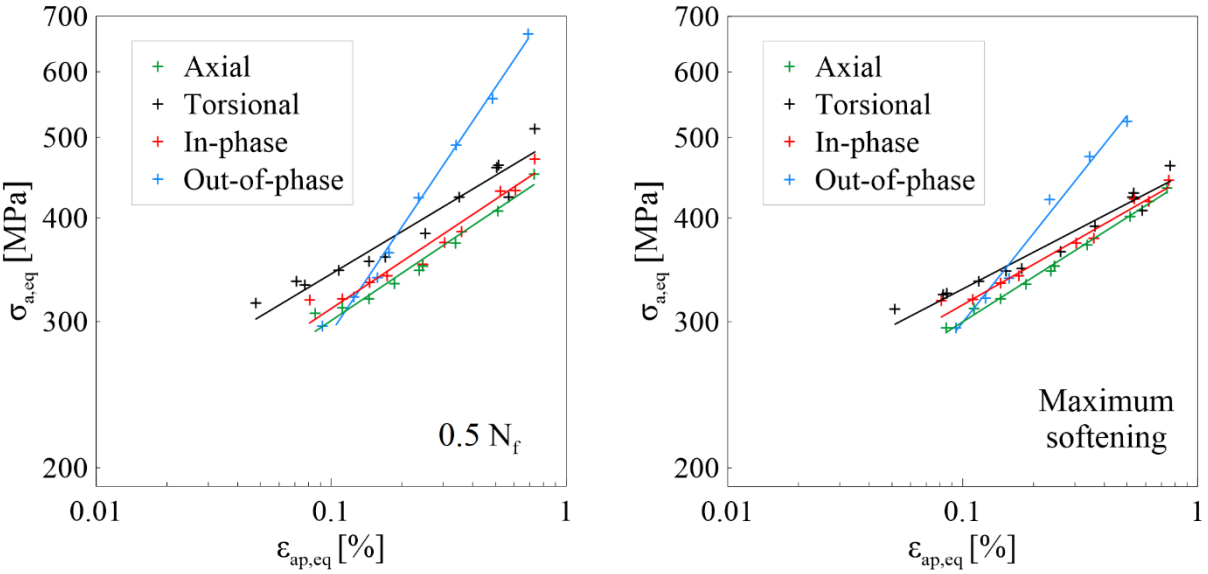

Fig. 40 Cyclic stress-strain curves based on half-life (left) and maximum softening cycles (right).

It is noteworthy that A, T, and IP curves get closer when they are plotted using the data from the maximum softening cycle. This phenomenon can be explained by Tab. 8 containing information about when the maximum softening occurred. The corresponding cycle is denoted as N_{min} and a relative value N_{min}/N_f in percent is included in Tab. 8. There is a well-visible trend in A, IP, and OP modes. The maximum softening cycle appeared in an early stage of the fatigue life when high levels of $\varepsilon_{a,eq}$ were applied. On the contrary, the maximum softening cycle was located near the end of the fatigue life when low $\varepsilon_{a,eq}$ was applied. T mode, on the other hand, does not exhibit such a tendency. The sample cycled with $\varepsilon_{a,eq}$ = 0.24 % reached the maximum softening after 10.4 % of N_f. The data for the half-life CSSC of T mode were therefore derived during the secondary hardening phase while the data for other modes were obtained during the softening phase. T mode CSSC acquired from half-life is thus shifted to higher stress amplitudes. On the contrary, the curve corresponding to maximum softening is located lower and it is getting closer to IP and A curves.

Tab. 8 A relative location of the maximum softening cycle N_{min} in relation to N_f.

$\varepsilon_{a,eq}$ [%]	A	T	IP	OP
0.24	87.3	10.4	60.4	89.5
0.28	67.3	11.7	57.3	78.2
0.32	60.5	6.7	68.1	49.9
0.35	49.3	13.8	68.8	80.7
0.44	41.5	13.1	38.6	24.0
0.57	28.1	8.5	21.8	4.4
0.75	5.5	7.6	4.0	3.9
1.00	6.9	2.0	2.3	-

Tab. 9 presents the material parameters obtained from the Manson-Coffin (Eq. 3), S-N (Eq. 2), and cyclic stress-strain curves (Eq. 11). Parameters σ_f', b, ε_f', c, K', and n' were received from analysis of A tests while parameters τ_f', γ_f', b_t, and c_t correspond to T tests. The Young modulus E and shear modulus G were determined from the initial cycle of each axial and torsional test, respectively. The mean value of the measured data was used for presenting E and G in Tab. 9.

Tab. 9 Material parameters of 316L steel.

E	G	σ'_f	τ'_f	b	c	ε'_f	b_t	c_t	γ'_f	K'	n'
GPa	GPa	MPa	MPa	-	-	-	-	-	-	MPa	-
197.5	75.5	846	471	-0.090	-0.509	0.343	-0.069	-0.442	0.584	1059	0.183

5.1.4 Hysteresis loops

Hysteresis loops corresponding to the maximum softening cycle from every loading mode are shown in Fig. 41. In the case of OP loading mode, only T loops are presented (it is not possible to show hysteresis loops depicted in equivalent strain and stress in OP mode). Loops are shifted so their left bottom apex is placed at the origin of the coordination system. Such a configuration enables us to see whether the material exhibits Masing behavior or not. If it does, the rising half-loops of different amplitudes lie on the same curve. Masing behavior can be typically observed in materials whose microstructure developed during cyclic loading is not dependent on the amplitude [119]. It is not the case with 316L steel because the martensitic transformation is getting more intense with increasing amplitude of loading (see section 5.2.1). To eliminate secondary hardening caused by α′ martensite, only loops corresponding to the maximum softening cycle were considered. Masing behavior was observed only in the case of low amplitudes in A mode (up to $\varepsilon_{a,eq}$ = 0.44 %).

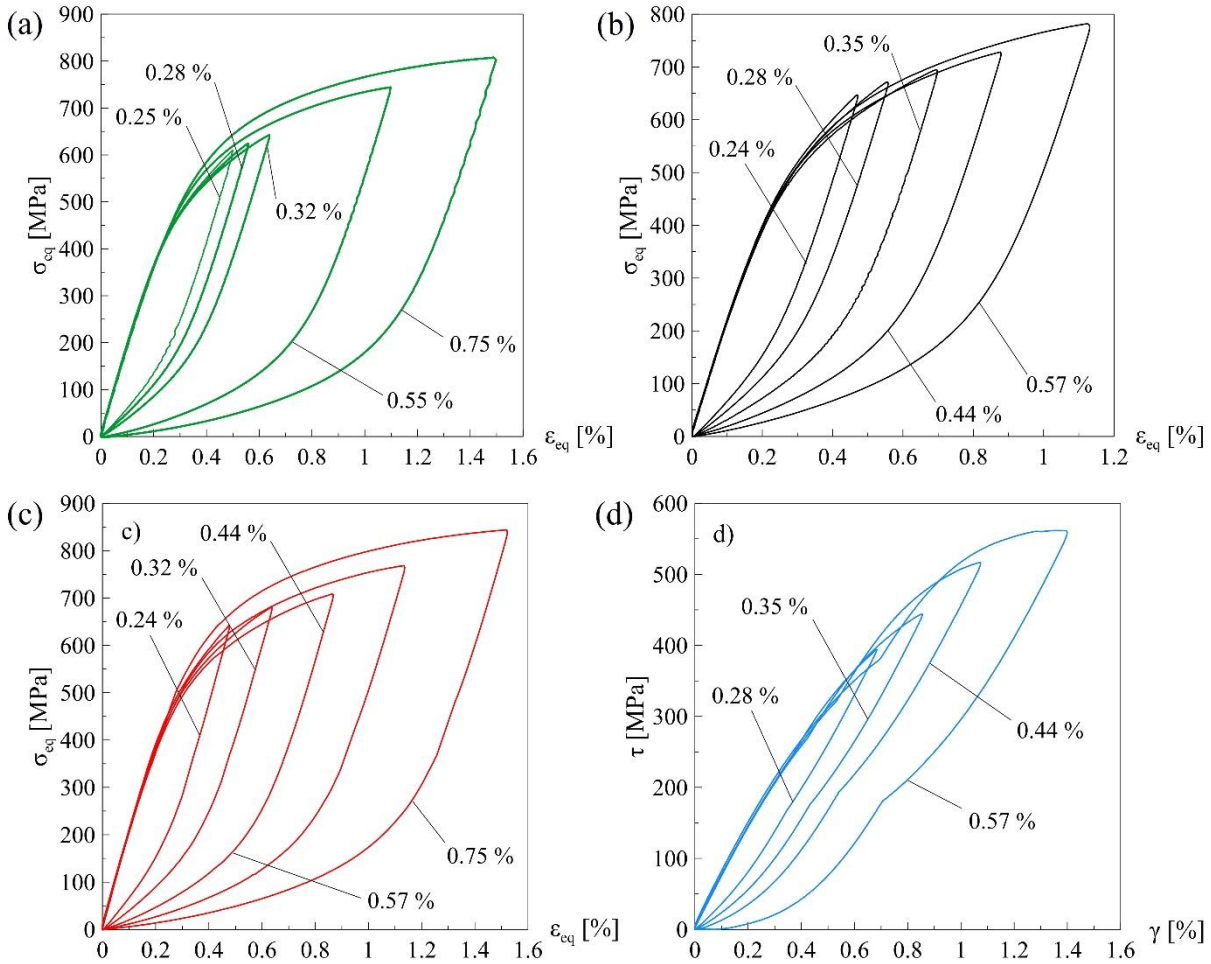

Fig. 41 Hysteresis loops from maximum softening cycle shifted to common origin (a) A (b) T (c) IP (d) T loops from OP mode.

5.2 Microstructural analysis

The first section of the following chapter is devoted to an EBSD analysis revealing the phase stability of 316L steel. The second section deals with dislocation structures developed due to cyclic loading.

5.2.1 Diffraction of backscattered electrons

EBSD maps from a cross-section perpendicular to the specimen axis were performed to analyze the phase stability of 316L steel. Unfortunately, the EBSD technique is not able to distinguish between δ ferrite and strain-induced α′ martensite. Both phases - δ ferrite, existing in the as-received material, and α′ martensite, induced during cyclic straining, are therefore represented by the same red color in phase maps while the blue color represents the austenitic matrix. The as-received microstructure is shown in Fig. 42 in form of an inversed pole figure and a phase map. Well-visible hot rolling bands may be seen in Fig. 42(a) while thin δ ferrite bands formed along hot rolling bands are depicted in Fig. 42(b). The measured amount of δ ferrite in the as-received microstructure was 1.45 %. The amount of α′ martensite was evaluated as the difference between the measured value and the content of δ ferrite in the as-received microstructure.

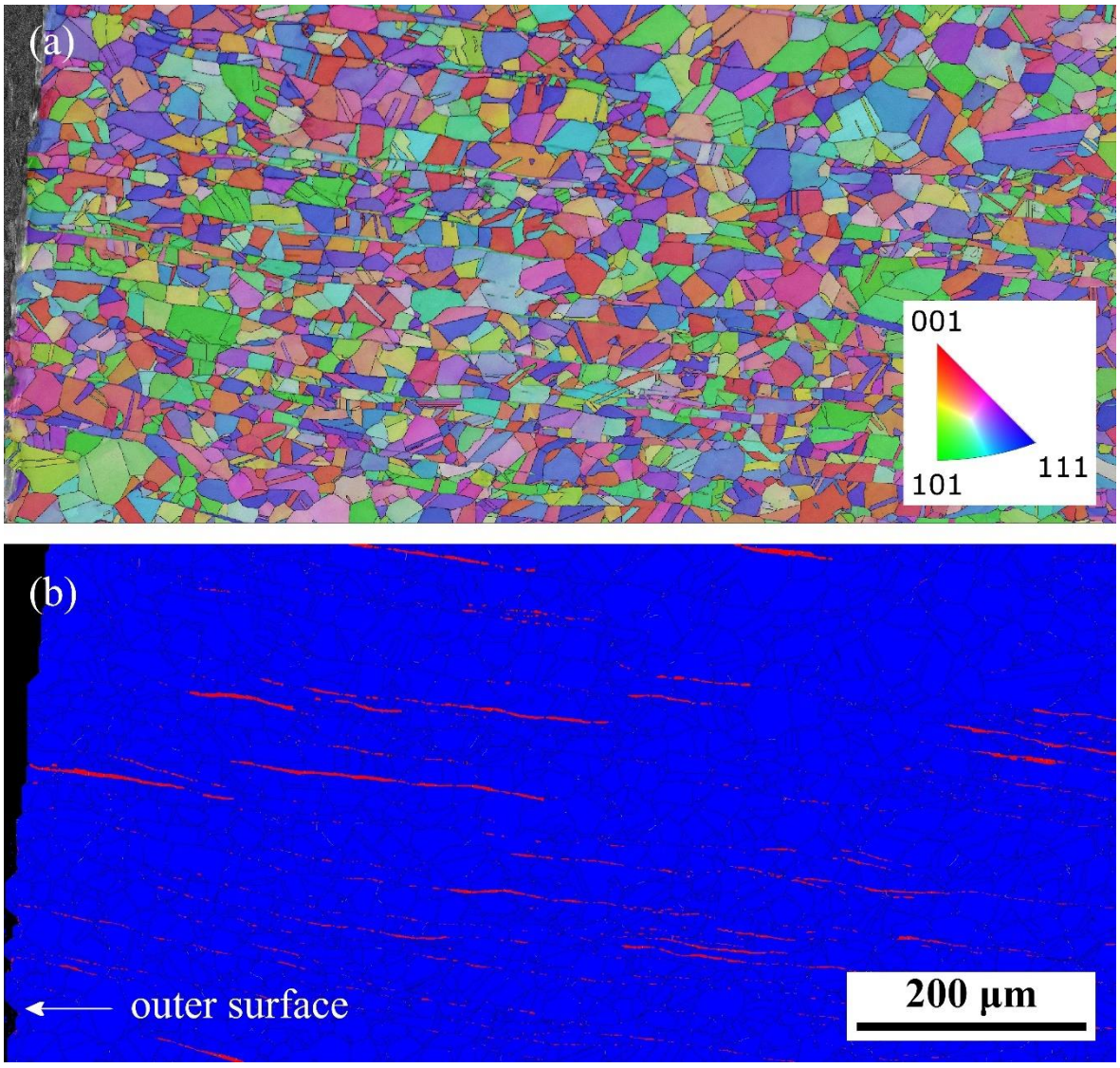

Fig. 42 The as-received microstructure of 316L steel (a) an inversed pole figure (b) a phase map where the red color represents δ ferrite and the blue color represents austenite.

The EBSD analysis was performed on specimens cycled with $\varepsilon_{a,eq}$ = 0.24; 0.57, and 1.00 %. Acquired phase maps from every loading mode are shown in Fig. 43 - Fig. 45. The measured amount of α′ martensite is listed in Tab. 10. The analysis of specimens cycled with $\varepsilon_{a,eq}$ = 0.24 % revealed that there are no signs of α′ martensite in A, T, and OP mode and only 0.7 % of α′ martensite was induced in IP mode. The orientation of phase maps in Fig. 43 - Fig. 45 is random as well as the orientation of δ ferrite bands.

Tab. 10 The percentage of α′ martensite measured by EBSD.

$\varepsilon_{a,eq}$ [%]	A	T	IP	OP
0.24	0	0	0.7	0
0.57	0.5	6.0	1.0	0
1.00	0.8	12.0	12.1	18.4

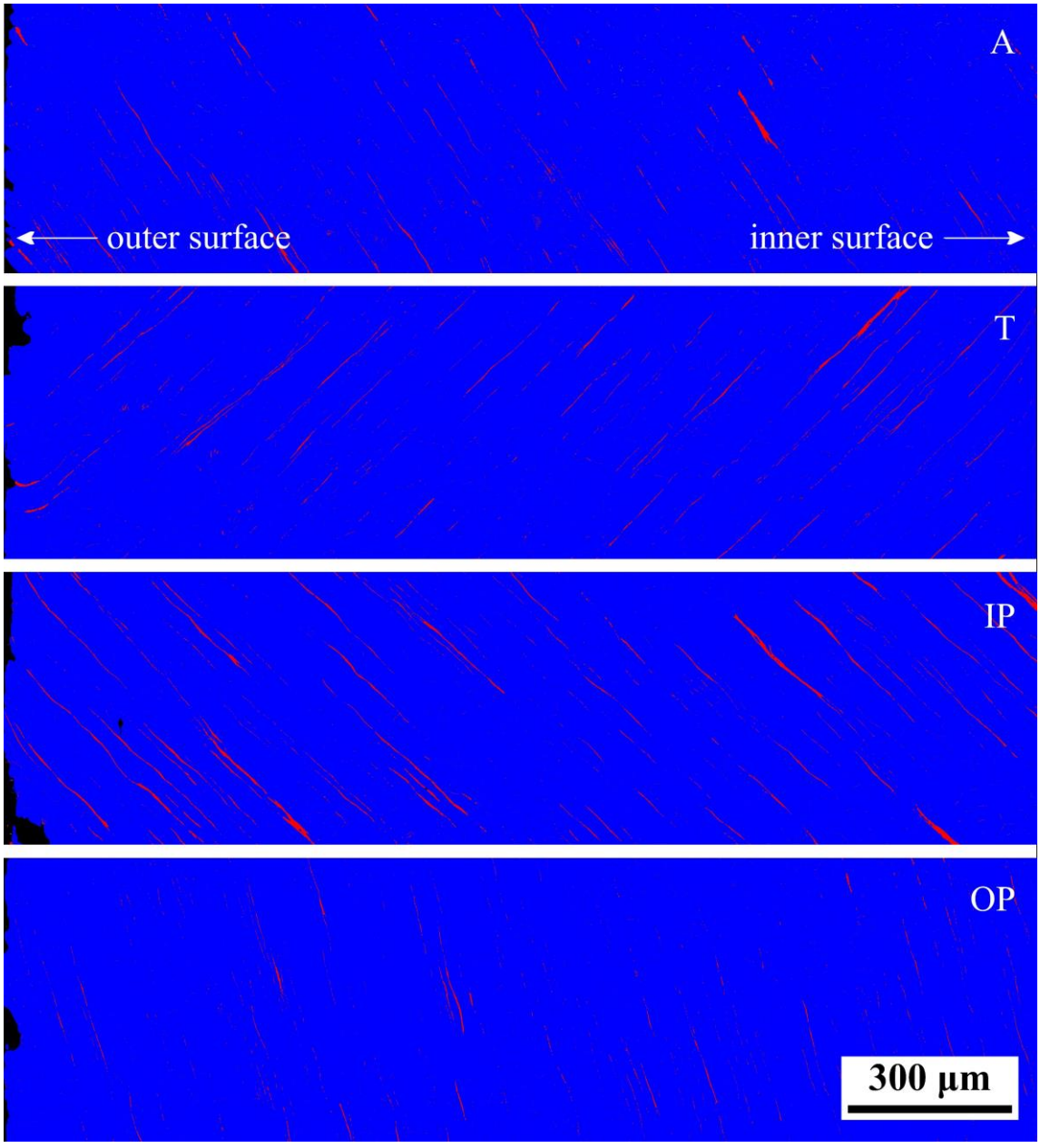

Fig. 43 Post-mortem EBSD phase maps of a cross-section perpendicular to the specimen axis. Specimens were cycled in A, T, IP, and OP mode with $\varepsilon_{a,eq}$ = 0.24 % . The red color represents α′ martensite or δ ferrite and the blue color represents austenite.

A negligible amount of α′ martensite in A, IP and OP mode was detected also in samples cycled with $\varepsilon_{a,eq}$ = 0.57 %. A significant change was observed in T mode where 6.0 % of α′ martensite was found. The distribution of α′ martensite was strongly inhomogeneous. The preferential sites of α′ martensite formation are close to the outer specimen surface. This is caused by an inhomogeneous strain field in torsion (the largest strain is located on the outer specimen surface and it decreases with decreasing distance from the specimen axis).

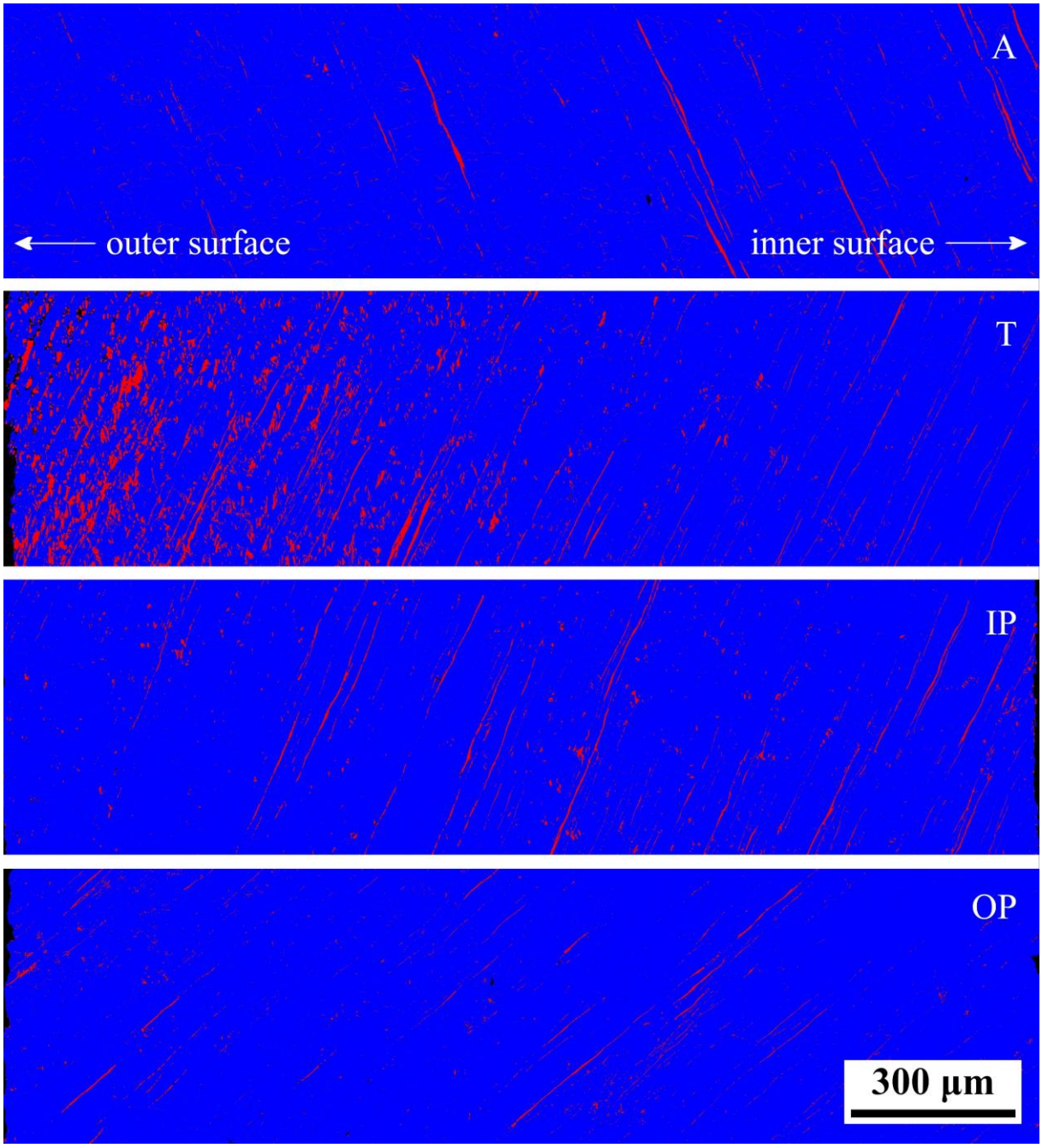

Fig. 44 Post-mortem EBSD phase maps of a cross-section perpendicular to the specimen axis. Specimens were cycled in A, T, IP, and OP mode with $\varepsilon_{a,eq}$ = 0.57 % . The red color represents α′ martensite or δ ferrite and the blue color represents austenite.

The analysis of specimens cycled with $\varepsilon_{a,eq}$ = 1.00 % discovered 0.8 % of α′ martensite in A mode, 12.0 % in T mode, 12.1 % in IP mode, and 18.4 % in OP mode. The amount of developed α′ martensite is therefore conclusively the lowest in the specimen cycled in A mode and its

distribution is homogeneous. The even distribution of α′ martensite across the specimen cross-section is due to a homogeneous strain field during uniaxial loading. A common feature of T, IP, and OP samples is the formation of α′ martensite along hot rolling bands presented in the as-received microstructure.

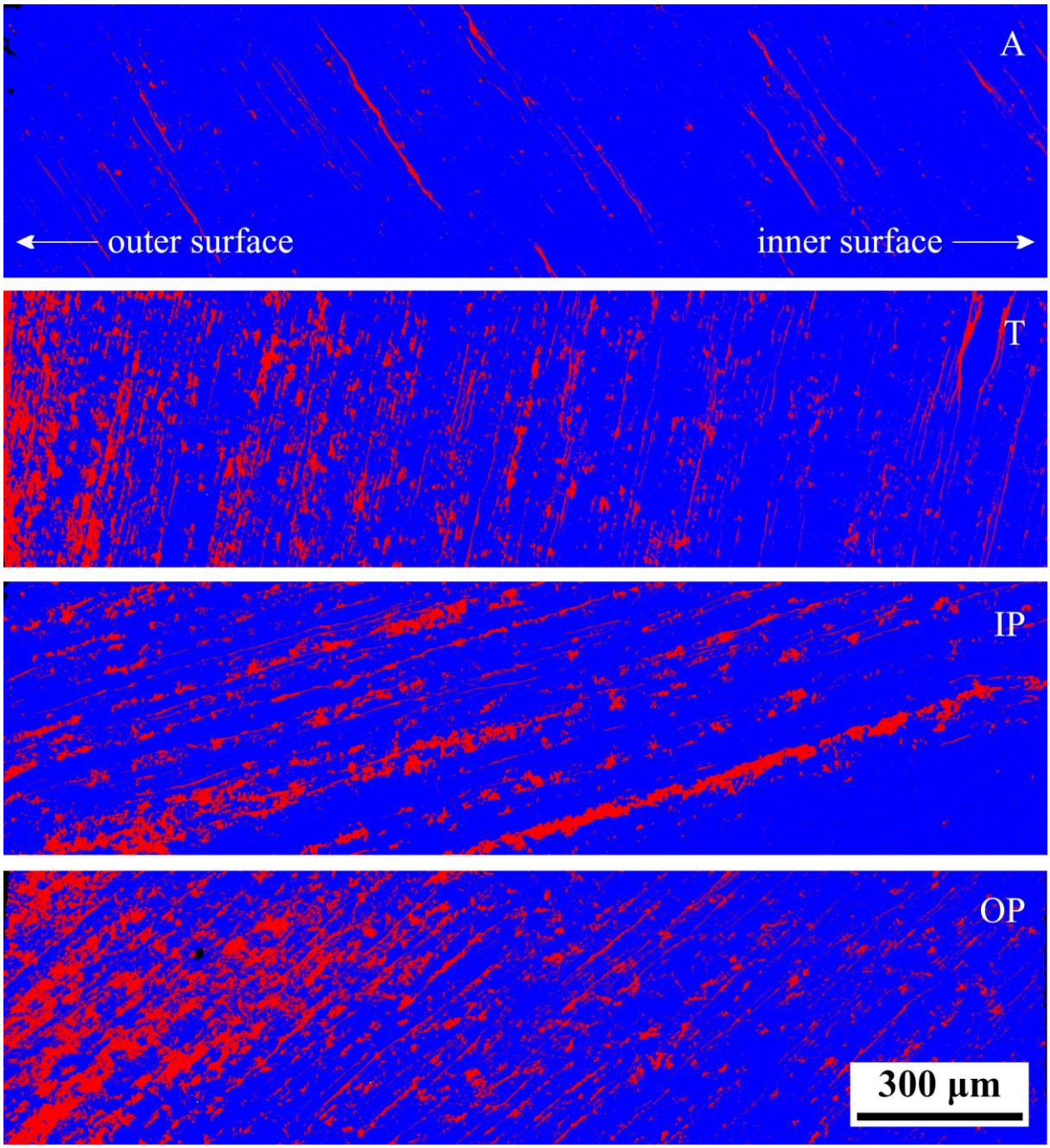

Fig. 45 Post-mortem EBSD phase maps of a cross-section perpendicular to the specimen axis. Specimens were cycled in A, T, IP, and OP mode with $\varepsilon_{a,eq}$ = 1.00 % . The red color represents α′ martensite or δ ferrite and the blue color represents austenite.

The α′ martensite distribution in T and OP specimens is comparable – α′ martensite was induced predominantly near the outer surface. A comparison of values measured in A and T mode reveals that a higher amount of α′ martensite develops under T loading. It is, therefore, reasonable to expect the same behavior in the case of OP mode, meaning that most of α′ martensite was induced during the T dominated part of the loading cycle and its distribution is resembling the distribution observed in the case of T mode.

A different distribution of α′ martensite was observed in the case of IP loading. A and T loading increase and decrease simultaneously during the IP loading cycle. The contribution of A loading makes the strain distribution more homogeneous therefore the α′ martensite distribution is also more homogeneous when compared to OP and T loading.

As mentioned earlier, the content of α′ martensite was measured also with the Feritscope on the outer surface of the specimens. The arithmetic means of measured volume fractions of magnetic phases reduced by the amount of δ ferrite are listed in Tab. 11.

Tab. 11 The increase of percentual volume fraction of α′ martensite due to cyclic loading as measured by Feritscope.

$\varepsilon_{a,eq}$ [%]	A	T	IP	OP
0.24	1.1	5.4	0	0
0.57	2.0	24.9	5.1	7.5
1.00	4.9	42.0	11.8	46.6

5.2.2 Transmission electron microscopy

A systematic study of 20 TEM foils from specimens loaded to fracture by various modes and strain amplitudes was performed to analyze the relationship between dislocation structures developed during cyclic loading and the mechanical response of the material. In the following, dislocation arrangements (or structures) formed during cycling are presented. Classification of individual structures follows papers dealing with dislocation structures in Cu [120] and 316 steel [18]. The structures are shown starting from those formed at the lowest strain amplitudes to the highest strain amplitudes. To be more specific, when low $\varepsilon_{a,eq}$ was applied, grains with low dislocation density, a planar slip arrangement, and a vein structure were observed. Dislocations were arranged into wall and labyrinth structures when $\varepsilon_{a,eq}$ increased and finally, dislocation cells were found to be a significant feature of high $\varepsilon_{a,eq}$ level. The maximum applied $\varepsilon_{a,eq}$ led to a disorientation of dislocation cells. More details concerning geometry and comparison with other papers are given in the Discussion. The observed structures are not always very typical – the transition arrangements between two different structures are often found. Also, close to grain boundaries, the influence of neighboring grains often causes a change in the local dislocation arrangements.

The microstructure of *as received material* is presented in Fig. 46. As mentioned earlier, the material was supplied in form of hot rolled plates. The dislocation density was measured at two sites and it's average value was revealed to be 3.5×10^{13} m^{-2}. Dislocation tangles may be seen in the left right corner of Fig. 46. Otherwise, there is no apparent arrangement of dislocations.

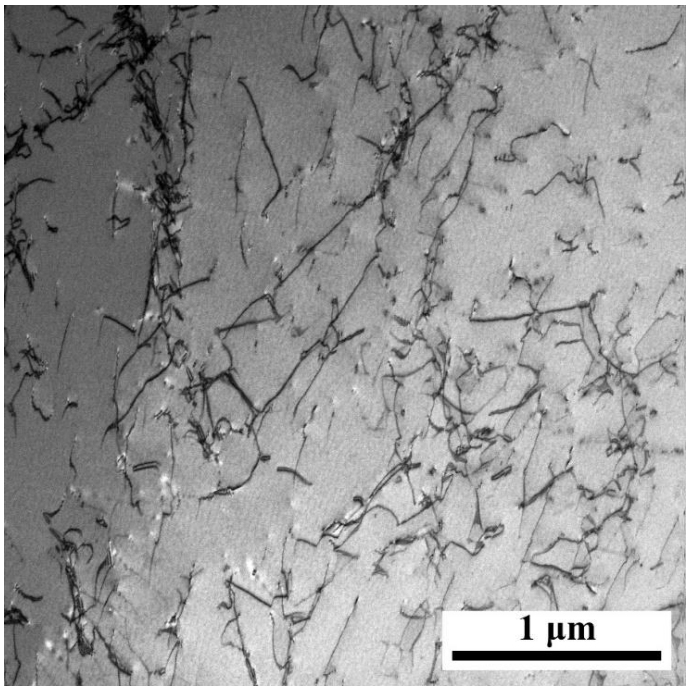

Fig. 46 Microstructure of as received material.

Low dislocation density may be seen in Fig. 47 as well as in Fig. 48. These structures can be observed in grains where only very limited plasticity took part in cycling so the dislocation density did not increase significantly and there is no spatial arrangement of dislocations.

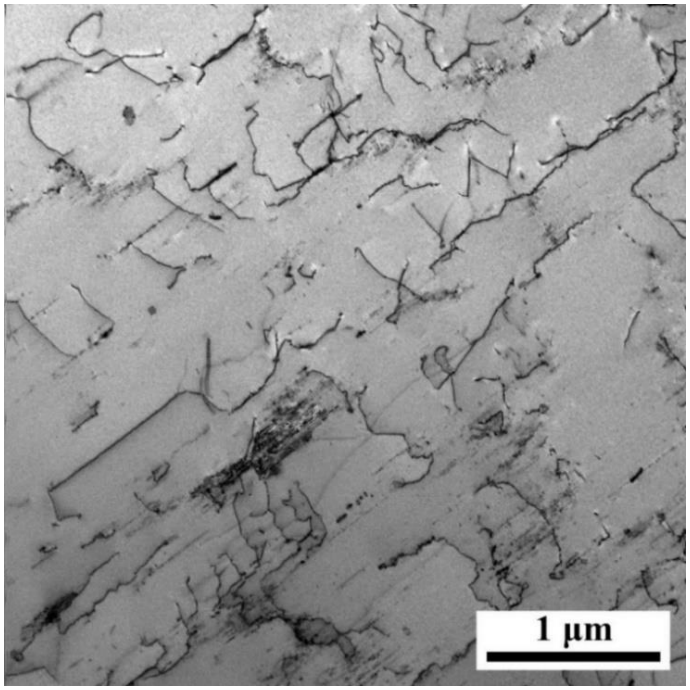

Fig. 47 Low dislocation density observed in the sample cycled in A mode using $\varepsilon_{a,eq}$ = 0.24 %.

An example of *planar arrangement* is depicted in Fig. 48. It is a characteristic feature of materials where the cross-slip mechanism is difficult and only planar slip of dislocations occurs. It means that the dislocations slip only in one plane back and forth during cycling. The structure is formed by dislocation-rich planes, where a dislocation source has operated, separated by layers with low dislocation density. The trace of the slip plane is highlighted in Fig. 48. Planar

arrangement is typical for fcc metals exhibiting low stacking fault energy when subjected to cyclic loading with low strain amplitude.

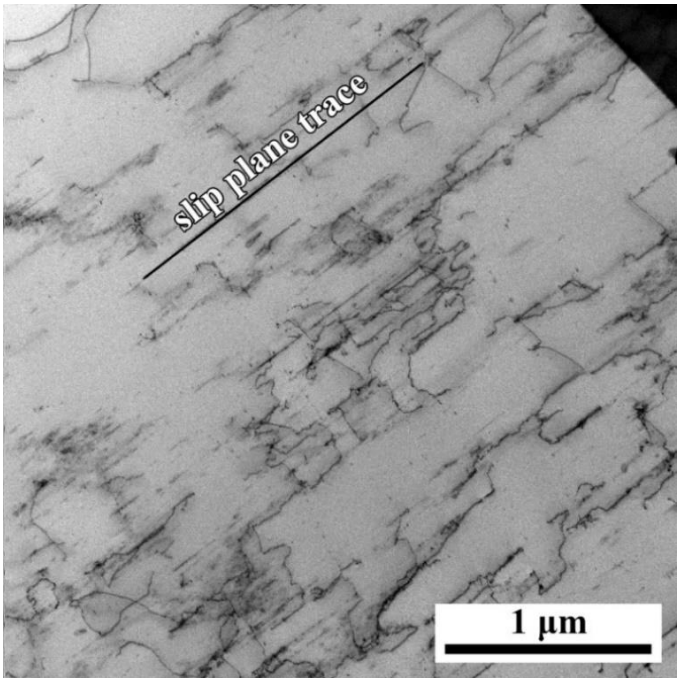

Fig. 48 M18 - Low dislocation density and planar slip observed in the sample cycled in A mode using $\varepsilon_{a,eq}$ = 0.24 %.

Vein structure: planar aspect of the slip is not observed which indicates that stress level and crystallographic orientation enable the operation of the cross-slip mechanism. Dislocation tangles exhibiting high dislocation density are visible in Fig. 49 and Fig. 50. Tangles are not mutually connected and they are not condensed as in the case of primary walls. An area between tangles is characteristic of low dislocation density – see Fig. 49. The vein structure develops when low loading amplitude is applied. Planar slip may be therefore seen in the neighboring grain in Fig. 50.

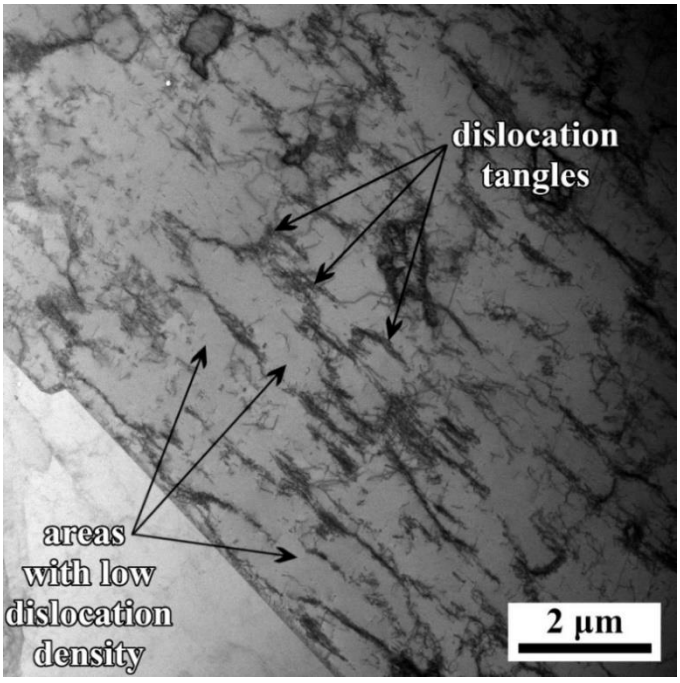

Fig. 49 Vein structure observed in the sample cycled in IP mode using $\varepsilon_{a,eq}$ = 0.32 %..

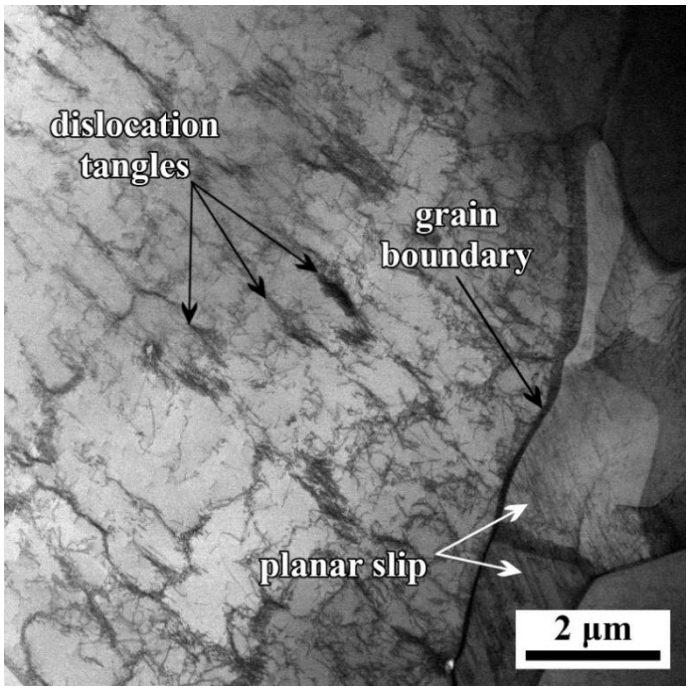

Fig. 50 Vein structure and planar slip observed in the sample cycled in IP mode using $\varepsilon_{a,eq}$ = 0.32 %..

Primary walls schematically shown in Fig. 52 are formed by edge dislocations from the primary slip system. Edge dislocations are arranged in Taylor´s network, i.e. they are placed close to the equilibrium positions according to mutual stress interactions – see Fig. 51. For creating such walls, cross-slip is necessary for filling the whole grain by dislocations.

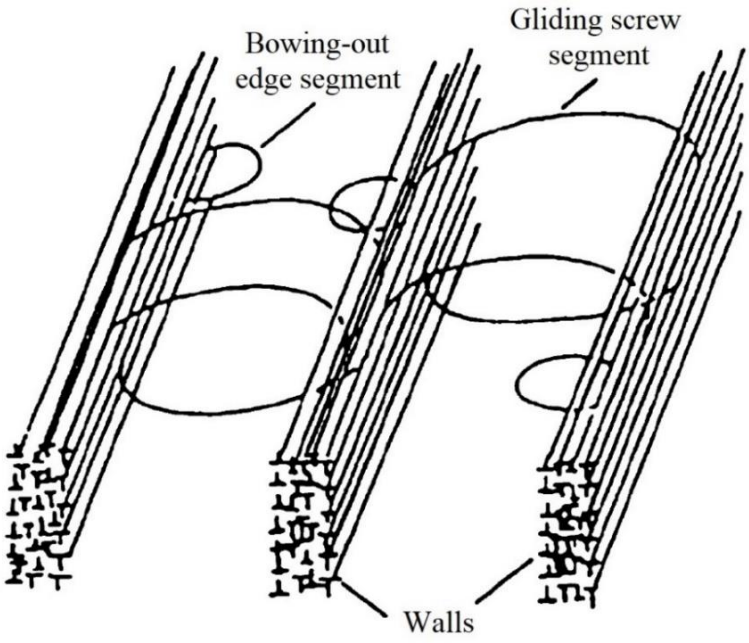

Fig. 51 Taylor's network forming dislocation walls [121].

Primary walls are considered to be relatively stable. Plastic deformation is therefore transmitted by the slip of screw and mixed dislocations in channels between the walls where dislocation density is low and the movement of dislocations is easier, contrary to dislocation-rich walls (Fig. 52).

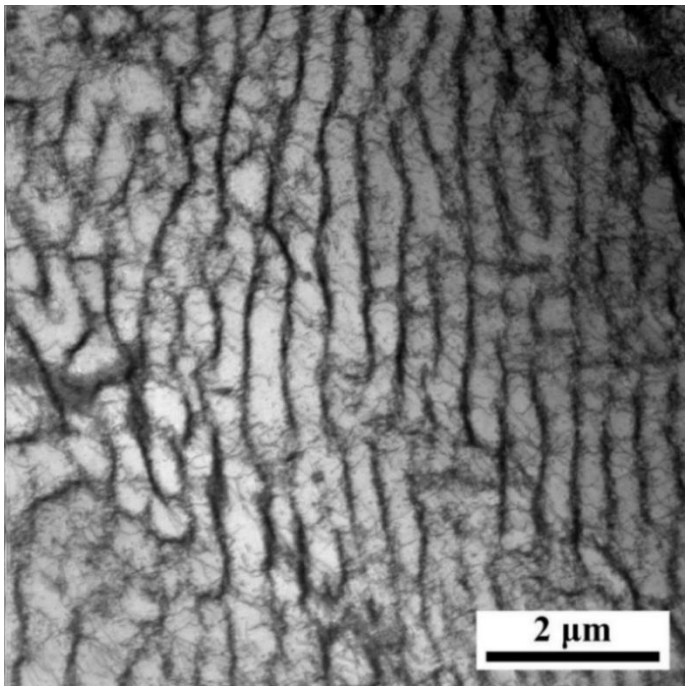

Fig. 52 Primary walls observed in the sample cycled in OP mode using $\varepsilon_{a,eq}$ = 0.44 %..

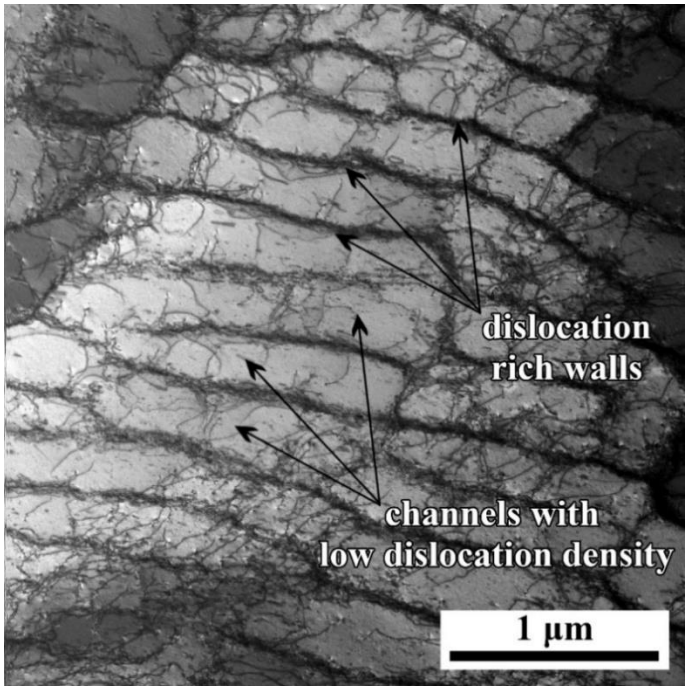

Fig. 53 Primary walls observed in the sample cycled in A mode using $\varepsilon_{a,eq}$ = 1.00 %..

Labyrinth/secondary walls are depicted in Fig. 54 and Fig. 55. Walls are developed as a consequence of an interaction of dislocations from two different slip systems. This is the main difference compared to primary walls which are formed by dislocations from the primary slip system only. The wall direction is given by active slip systems as it halves the angle between long dislocation segments from both systems [122] – see Fig. 54 and Fig. 55. Because there are dislocations from two different slip systems in the channels, the slip of individual dislocations is not as easy as in the case of the primary wall structure. The consequence of the labyrinth structure is thus the cyclic hardening of the material.

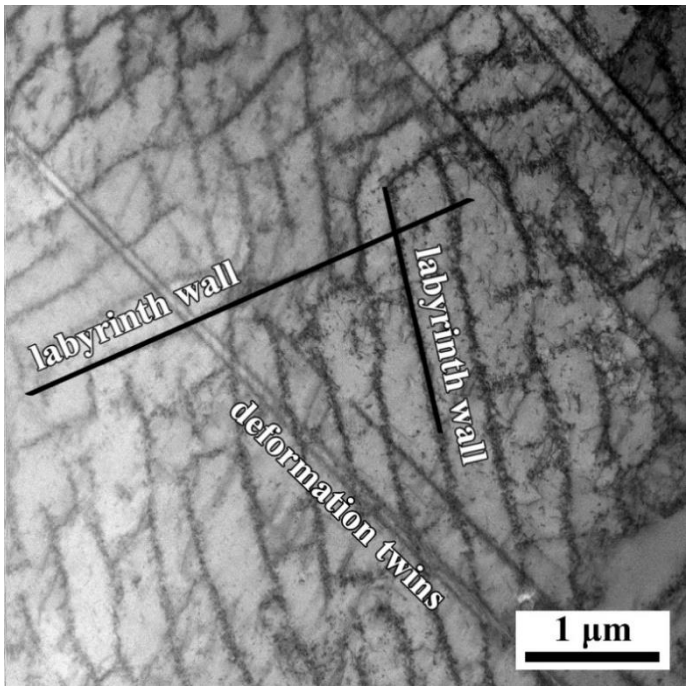

Fig. 54 Labyrinth structure and deformation twins observed in the sample cycled in OP mode using $\varepsilon_{a,eq}$ = 1.00 %.

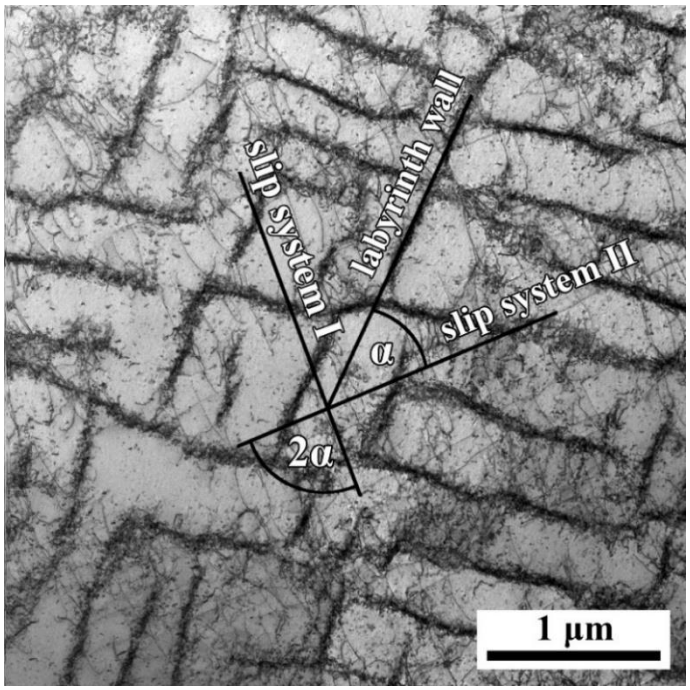

Fig. 55 Slip systems and labyrinth structure observed in the sample cycled in A mode using $\varepsilon_{a,eq}$ = 1.00 %..

Equally oriented cells: at high loading levels, where more slip systems are active, dislocations produce spatially closed, approximately equiaxial cells. The cell walls concentrate most dislocations while low dislocation density is found inside the cells. Fig. 56 and Fig. 57 show well-developed cells as well as not fully closed cells. Deformation twins may be seen in Fig. 56 while islands of α′ martensite are found in Fig. 57.

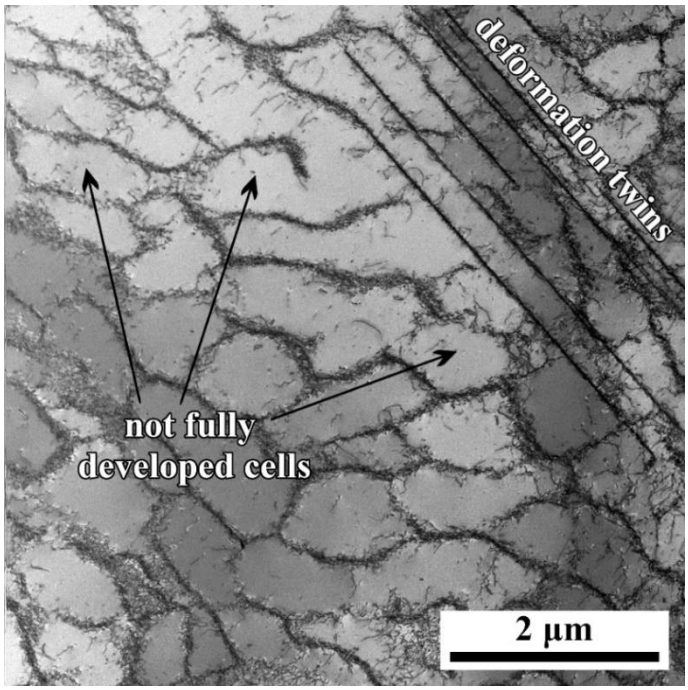

Fig. 56 Equally oriented dislocation cells and deformation twins observed in the sample cycled in IP mode using $\varepsilon_{a,eq}$ = 1.00 %.

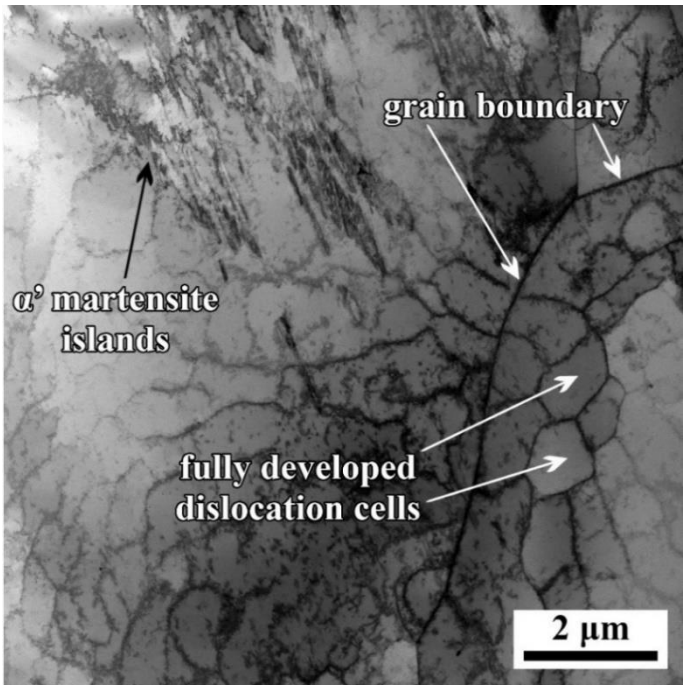

Fig. 57 Equally oriented dislocation cells and strain-induced α´martensite observed in the sample cycled in T mode using $\varepsilon_{a,eq}$ = 0.57 %.

Disoriented cells: high strain amplitude may cause mutual crystallographic disorientation of neighboring cells (typically 0.1° - 0.5°) and elongation of cells. Because diffraction contrast is very sensitive to crystallographic orientation, even such small disorientation results in different contrast of individual cells in Fig. 58 and Fig. 59. Walls of disoriented cells are usually very well condensed. The interior of cells is characterized by extremely low dislocation density; all dislocations are incorporated into cell walls.

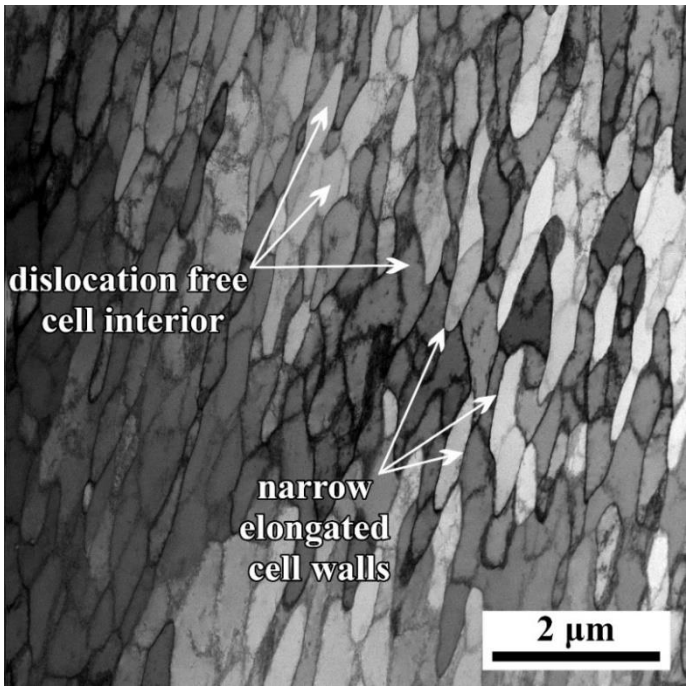

Fig. 58 Disoriented cells observed in the sample cycled in IP mode using $\varepsilon_{a,eq}$ = 1.00 %.

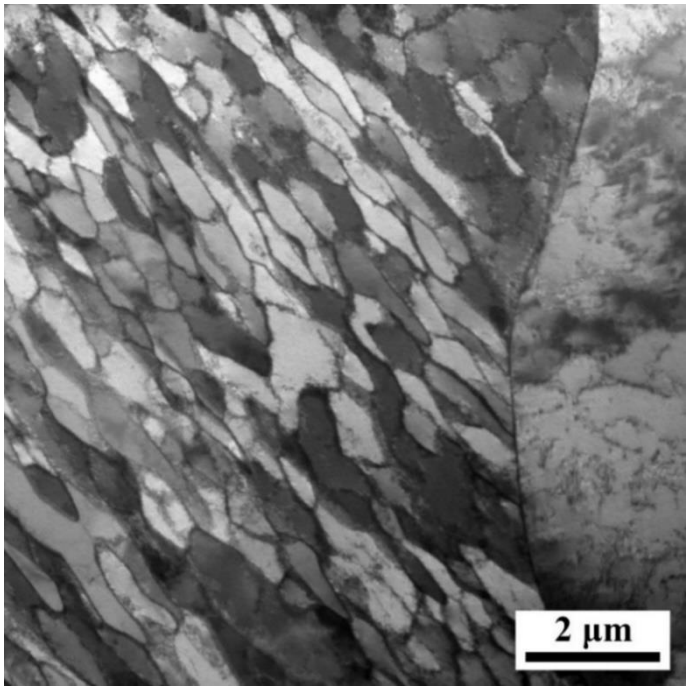

Fig. 59 Disoriented cells observed in the sample cycled in IP mode using $\varepsilon_{a,eq}$ = 0.44 %..

As already mentioned, seven distinct dislocation structures presented in Fig. 47 - Fig. 59 were identified. Their fraction is dependent on the loading mode and strain amplitude. Statistics of observed dislocation structures are listed in Tab. 12. Up to 200 grains were observed on every foil (depending on its quality and the area suitable for TEM observation).

Tab. 12 Fractions of different types of dislocation structures in individual specimens (in %).

Mode	$\varepsilon_{a,eq}$ [%]	Low dislocation density	Planar structures	Veins	Primary walls	Labyrinth	Equally oriented cells	Disoriented cells
A	1.00	0	0	0	30.6	16.0	53.5	10.4
	0.57	0	0	5.5	69.2	2.2	23.1	1.1
	0.44	0	0	18.0	67.2	0	14.8	4.9
	0.32	0.6	0.6	29.1	54.5	0	15.2	0
	0.24	0.6	9.0	60.6	23.2	0	6.5	0.6
T	1.00	0	0	0	2.7	8.9	69.2	19.2
	0.57	0	0	4.6	78.9	0	11.9	4.6
	0.44	0	0	20.5	57.5	0	20.5	1.4
	0.32	0	0	33.5	64.1	0	2.4	0
	0.24	16.7	4.2	69.8	9.4	0	0	0
IP	1.00	0	0	0	35.5	13.5	40.6	10.3
	0.57	0	0	0	70.3	4.1	18.9	6.8
	0.44	0	0	4.7	67.3	0	22.4	5.6
	0.32	0	1.5	52.2	39.7	0	6.6	0
	0.24	11.0	0	81.7	7.3	0	0	0
OP	1.00	0	0	0	0	2.0	29.4	68.6
	0.57	0	0	0	16.7	59.3	21.3	2.8
	0.44	0	0	18.9	14.4	62.2	4.5	0
	0.32	0	0	25.3	10.9	63.8	0	0
	0.24	0	2.7	75.5	21.8	0	0	0

An influence of applied loading on the arrangement of dislocations is schematized in Fig. 60. It may be seen that the same dislocation arrangements were found in all loading modes when $\varepsilon_{a,eq}$ = 0.24 % was applied (particular structures were observed similarly often). A substantial change was noted when TEM foils prepared from samples cycled with $\varepsilon_{a,eq}$ = 0.32 % were analyzed. The labyrinth structure was found to be the most frequent in the case of OP mode while being extremely rare in other loading modes. The same trend is valid also for the amplitudes 0.44 % and 0.57 %. Cyclic loading with $\varepsilon_{a,eq}$ = 1.00 % caused that equally oriented cells prevailed in the microstructure of A, T, and IP-loaded specimens while disoriented cells were the most common in OP mode.

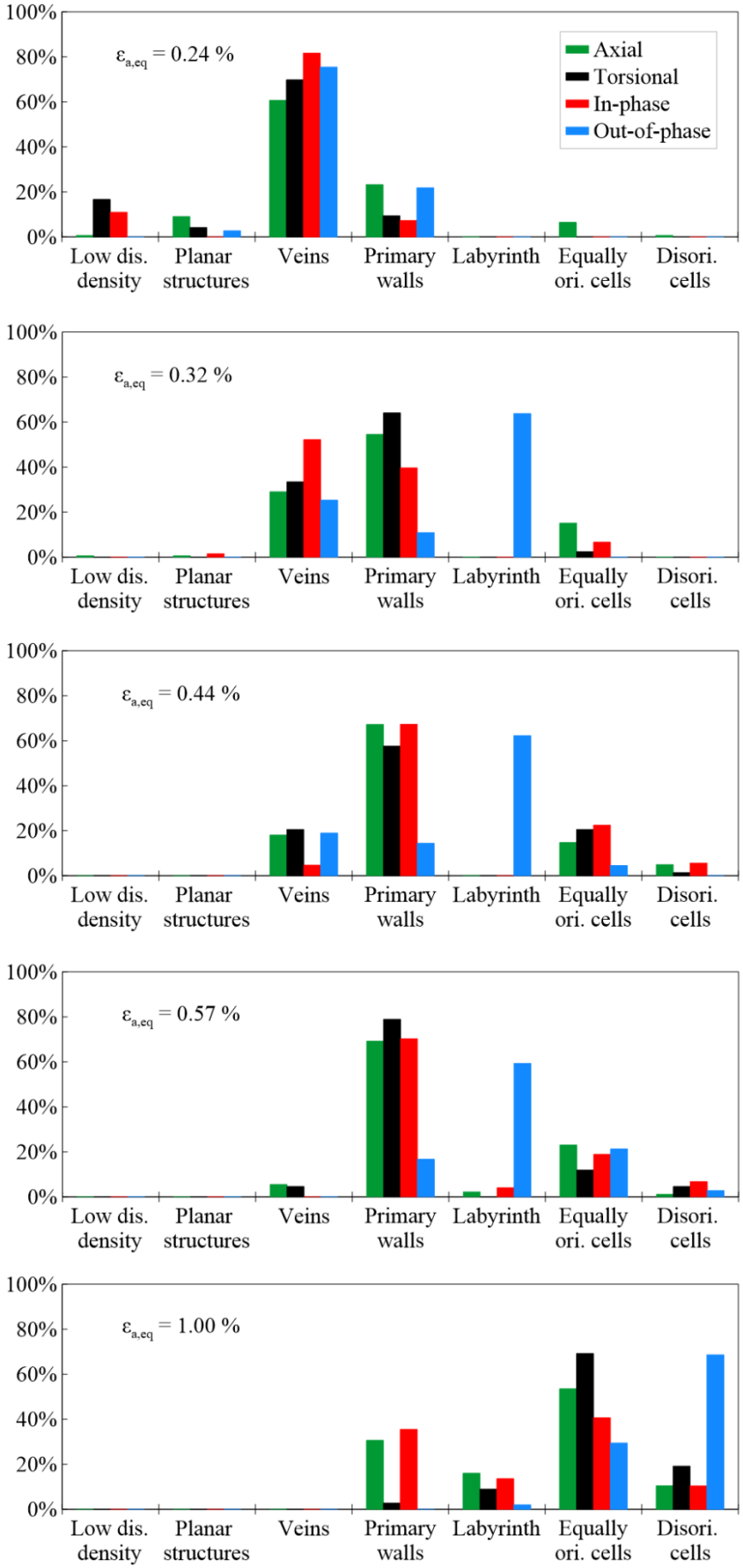

Fig. 60 Comparison of dislocation structures developed under various loading modes with a given level of $\varepsilon_{a,eq.}$

5.3 Crack growth rate tests

For a deeper examination of different crack growth kinetics in various loading modes, a series of CGR tests were performed. It is noteworthy that the initiation period was influenced by the presence of an artificial crack starter. Consequently, it does not coincide with the initiation period of fatigue cracks observed on smooth specimens. It is however supposed, that CGR measured far from the notch is not affected. Performed CGR tests are listed in Tab. 13. The column denoted as N_{1000} represents the number of cycles when the crack length surpassed 1000 μm. The crack length a is defined in Fig. 30.

Tab. 13 List of performed crack growth rate tests.

mode	A/T	$\varepsilon_{a.eq}$ [%]	ε_a [%]	γ_a [%]	$\varepsilon_{ap.eq}$ [%]	$\sigma_{a.eq}$ [MPa]	σ_a [MPa]	τ_a [MPa]	N_{1000} [-]
A	100/0	0.330	0.330	0	0.147	345	345	0	1380
	100/0	0.441	0.441	0	0.270	355	355	0	560
	100/0	0.550	0.550	0	0.351	361	361	0	520
	100/0	0.750	0.750	0	0.520	403	403	0	285
T	0/100	0.279	0	0.483	0.117	337	0	195	16000
	0/100	0.329	0	0.569	0.161	339	0	196	9000
	0/100	0.367	0	0.636	0.193	354	0	204	8500
	0/100	0.409	0	0.708	0.227	362	0	209	5200
	0/100	0.440	0	0.762	0.256	368	0	213	5800
	0/100	0.546	0	0.945	0.345	383	0	221	2520
	0/100	0.680	0	1.177	0.463	418	0	242	1720
	0/100	0.999	0	1.730	0.750	474	0	273	600
IP	50/50	0.238	0.164	0.299	0.077	3245	218	139	4900
	50/50	0.278	0.193	0.347	0.109	346	229	143	2600
	50/50	0.353	0.250	0.430	0.171	351	255	139	1400
	27/73	0.439	0.154	0.713	0.263	349	132	186	1100
	46/54	0.433	0.283	0.566	0.243	371	247	160	1000
	50/50	0.434	0.312	0.523	0.244	356	259	141	2100
	65/35	0.440	0.388	0.359	0.246	368	326	97	700
	80/20	0.439	0.427	0.178	0.243	350	342	45	730
	50/50	0.559	0.399	0.678	0.354	388	275	158	650
	50/50	0.698	0.495	0.851	0.485	413	304	161	360
	50/50	0.996	0.707	1.214	0.744	445	319	179	230
OP	50/50	0.238	0.169	0.290	0.085	313	300	185	8900
	50/50	0.279	0.198	0.342	0.116	343	336	209	4200
	50/50	0.350	0.247	0.428	0.163	379	370	232	1800
	27/73	0.437	0.152	0.710	0.286	338	260	224	2650
	46/54	0.440	0.285	0.579	0.232	427	408	265	1100
	50/50	0.440	0.311	0.538	0.230	431	417	264	1550
	65/35	0.441	0.388	0.361	0.237	399	397	214	880
	80/20	0.440	0.428	0.182	0.254	370	370	118	900

50/50	0.571	0.404	0.697	0.336	488	466	294	480
50/50	0.751	0.531	0.921	0.488	537	515	325	250
50/50	0.986	0.709	1.176	0.690	599	576	365	190

5.3.1 Analysis by Polák and Zezulka [107]

Tests with the same A/T ratio

Fig. 61 (a), Fig. 62 (a), and Fig. 63 (a) show plots of crack length vs. number of cycles for four specimens cycled in distinct modes but with the same equivalent strain amplitude. Fatigue crack initiates much later in T mode. An incubation period in the other three modes is very similar, especially in the case of 0.33 % and 0.55 % strain amplitude. The dependence of the crack length a on the number of cycles N was fitted by Eq. 39, where a_i is the extrapolated crack length to zero cycle and k_g is the crack growth coefficient.

$$a = a_i \cdot e^{k_g \cdot N} \tag{39}$$

Eq. 40 shows a relation between $\frac{da}{dN}$ and crack length a. The relation was derived from Eq. 39.

$$\frac{da}{dN} = k_g \cdot a_i \cdot e^{k_g \cdot N} = k_g \cdot a \tag{40}$$

Fig. 61 (b), Fig. 62 (b) and Fig. 63 (b) depict measured values of CGR as a function of crack length. There is also a line representing values of CGR calculated using Eq. 39. The highest fatigue crack growth rate is in A mode and the lowest in T mode. Values of parameter k_g corresponding to T mode are approximately ten times lower compared to A mode (see Tab. 14). CGRs measured on specimens cycled in multiaxial modes are between them although they are much closer to A mode.

Tab. 14 Crack growth coefficient k_g from the tests with the same equivalent strain amplitude.

$\varepsilon_{a,eq}$ [%]	k_g *in* A	k_g *in* T	k_g *in* IP	k_g *in* OP
0.33	2.64×10^{-3}	1.81×10^{-4}	1.63×10^{-3}	1.15×10^{-3}
0.44	4.09×10^{-3}	3.38×10^{-4}	2.39×10^{-3}	2.14×10^{-3}
0.55	6.66×10^{-3}	7.54×10^{-4}	3.75×10^{-3}	6.18×10^{-3}

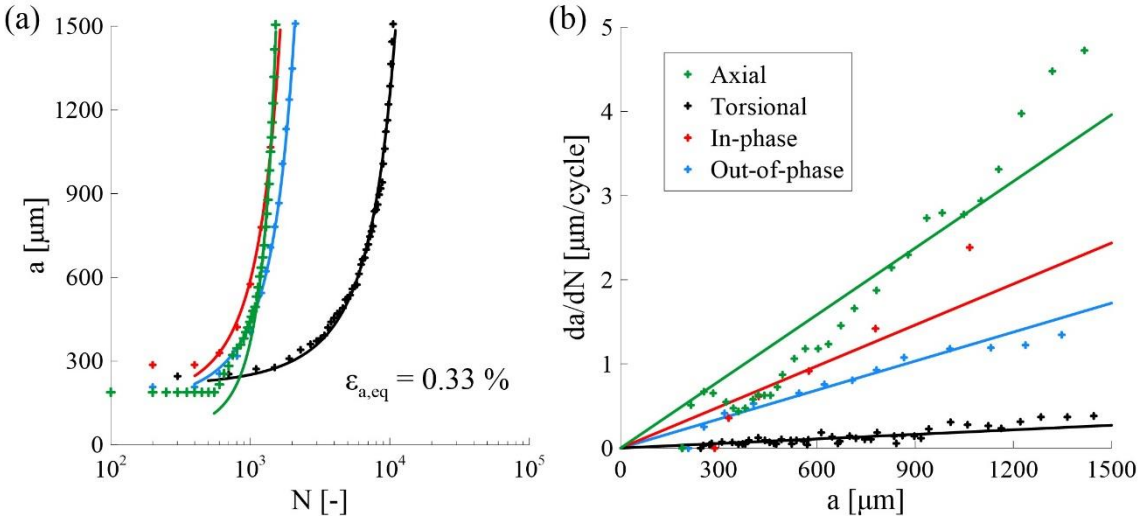

Fig. 61 Crack growth in cycling with $\varepsilon_{a,eq}$=0.33 % (a) a as a function of N; (b) da/dN as a function of a.

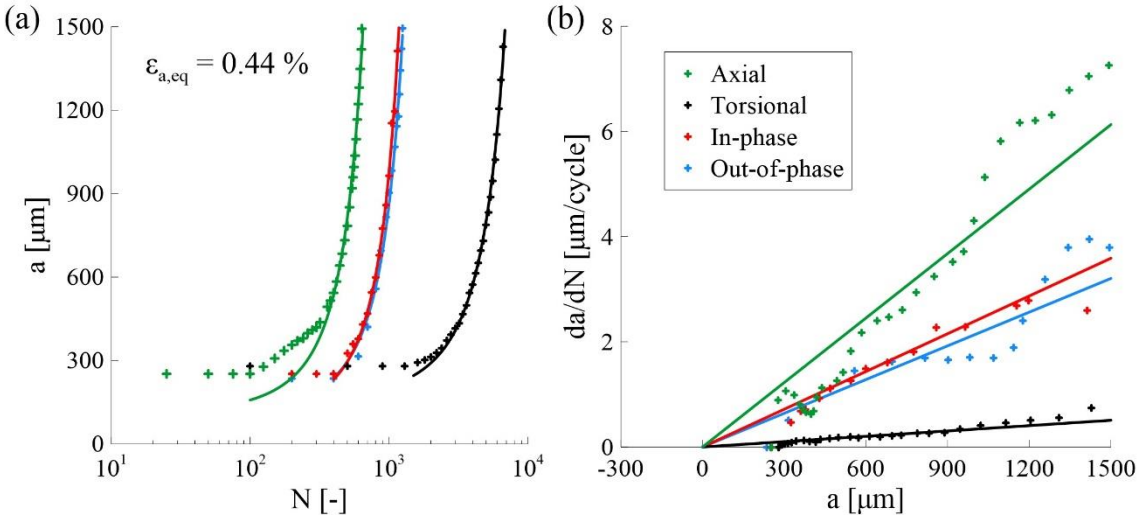

Fig. 62 Crack growth in cycling with $\varepsilon_{a,eq}$=0.44 % (a) a as a function of N; (b) da/dN as a function of a.

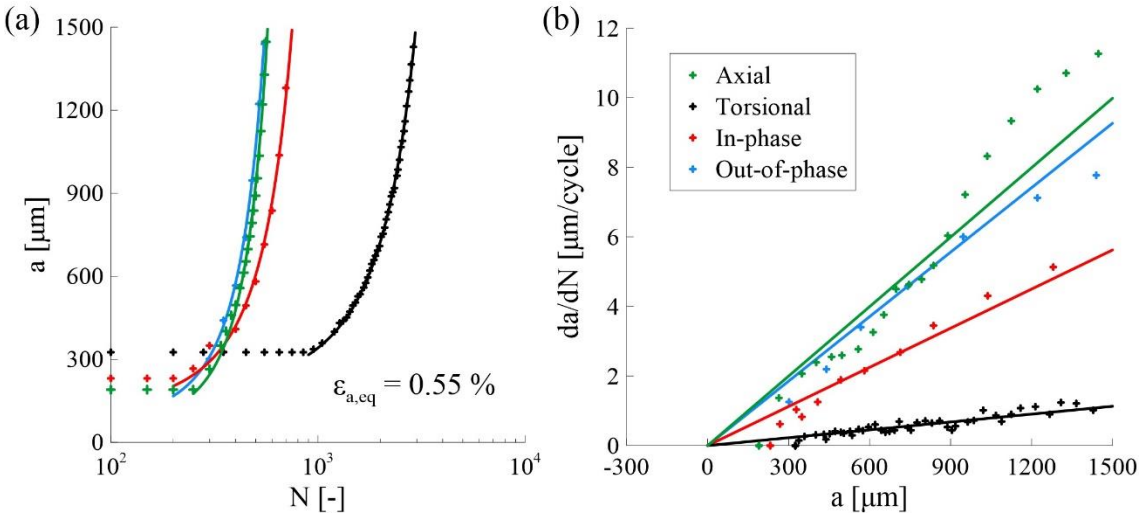

Fig. 63 Crack growth in cycling with $\varepsilon_{a,eq}$=0.55 % (a) a as a function of N; (b) da/dN as a function of a.

Parameter k_g was plotted as a function of $\varepsilon_{ap,eq}$ in Fig. 64. Based on the presented results, it may be concluded that regardless of loading amplitude, CGR reaches the lowest value in T mode. On the contrary, the highest CGR value was always measured in A mode. Curves of both multiaxial modes, therefore, lie between A and T curves. The value of k_g corresponding to OP mode is strongly decreasing with decreasing plastic strain amplitude. On the other hand, the slope of the IP curve is much less steep which leads to the crossing of the IP and OP curve. Based on this feature, it is possible to say that OP mode is more damaging in the case of low amplitudes, and IP mode results in higher CGR when the high amplitude is used.

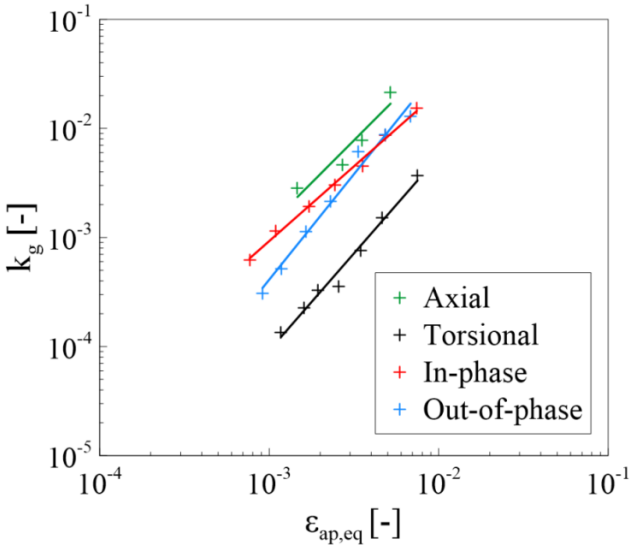

Fig. 64 Dependence of parameter k_g on the amplitude of equivalent plastic strain.

The data from CGR tests were further analyzed to reveal the portion of FL spent by crack growth from given length until the end of FL. The starting crack length was determined to 600 μm. This crack length was chosen because the diameter of the artificial crack starter was often larger than originally intended 300 μm and it's vicinity was affected by the process of spark erosion. The crack length 600 μm was therefore one of the shortest lengths that could be measured during most of the CGR tests. The subsequent analysis was performed in the following manner: i) the number of cycles corresponding to the moment when the crack length surpassed 600 μm denoted as N_{600} was determined, a linear approximation between two measurements was applied; ii) the corresponding criterion, described in the Chapter 4.3, determining the number of cycles to failure was utilized for the data from CGR tests, the established value was denoted as $N_{f\ CGR}$; iii) the number of cycles needed for the crack propagation from 600 μm until the end of FL was estimated as $N_{f\ CGR}$ - N_{600}; iv) the obtained value was further divided by N_f measured from FL tests performed using smooth specimens. The sought percentual part of FL spent by the propagation of the crack from 600 μm until the end of FL marked as $t_{propagation}$ was therefore determined according to the following equation:

$$t_{propagation} = \frac{N_{f\ CGR} - N_{600}}{N_f} \times 100 \tag{41}$$

Calculated values of $t_{propagation}$ are depicted in Fig. 65 as a function of strain amplitude for every loading mode. An increasing tendency of $t_{propagation}$ may be observed in A, IP and T mode. From the three mentioned loading modes, the IP mode's tendency was found to be the weakest. The strongest tendency towards increasing of $t_{propagation}$ with $\varepsilon_{a,eq}$ was noticed in T mode. OP mode, on the other hand, does not exhibit any dependence of $t_{propagation}$ on $\varepsilon_{a,eq}$ as it's value remains constant. The largest part of FL spent by the crack propagation was observed in T mode. The lowest values of $t_{propagation}$ were measured in A mode. IP and OP modes exhibited similar $t_{propagation}$ for $\varepsilon_{a,eq}$ = 1.00 % but lower $t_{propagation}$ may be seen in IP mode in the case of lower $\varepsilon_{a,eq}$.

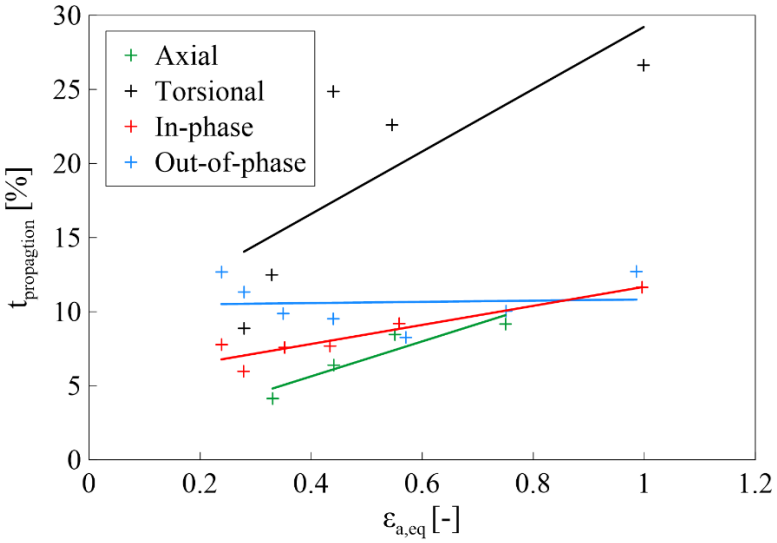

Fig. 65 $t_{propagation}$ as a function of equivalent strain amplitude.

Tests with various A/T ratio

Results from multiaxial modes presented to this moment were obtained from tests with ratio $\varepsilon / \frac{\gamma}{\sqrt{3}} = 1$ (such test is further marked as 50A-50T). To study the influence of changing the ratio between A and T amplitude, another two sets of multiaxial CGR tests were performed (one set in IP mode and one set in OP mode). Equivalent strain amplitude was always 0.44 % and the A/T ratio varied from 100A-0T to 0A-100T. The dependence of crack length on the number of cycles for IP and OP mode is depicted in Fig. 66 (a) and Fig. 67 (a), respectively. An incubation period is getting longer with prevailing torsional amplitude.

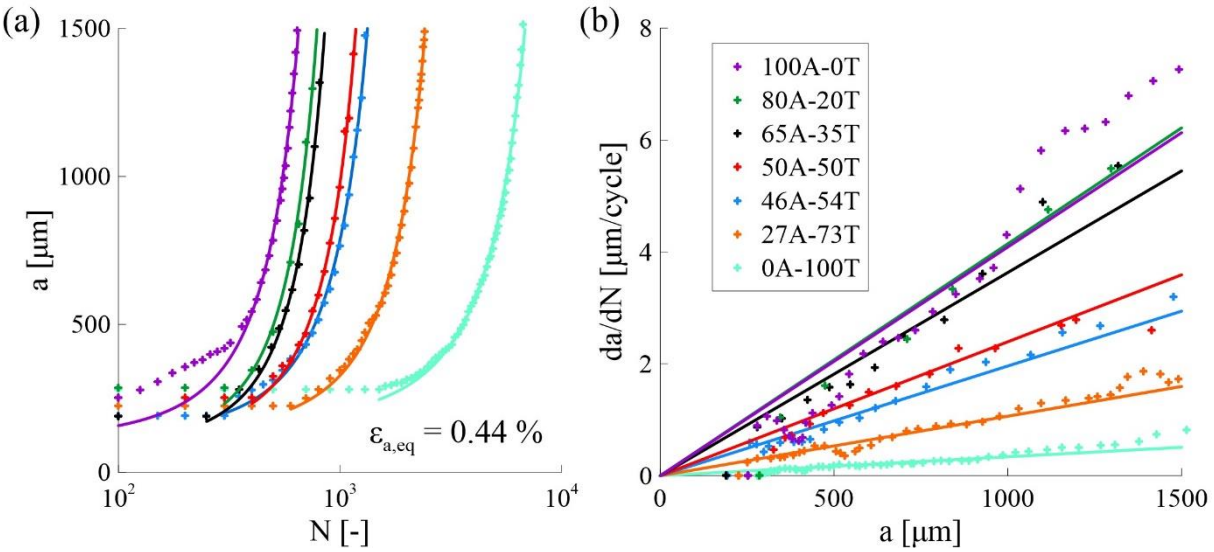

Fig. 66 Crack growth in cycling with $\varepsilon_{a,eq}$=0.44 %; IP mode with various A/T ratios (a) a as a function of N; (b) da/dN as a function of a.

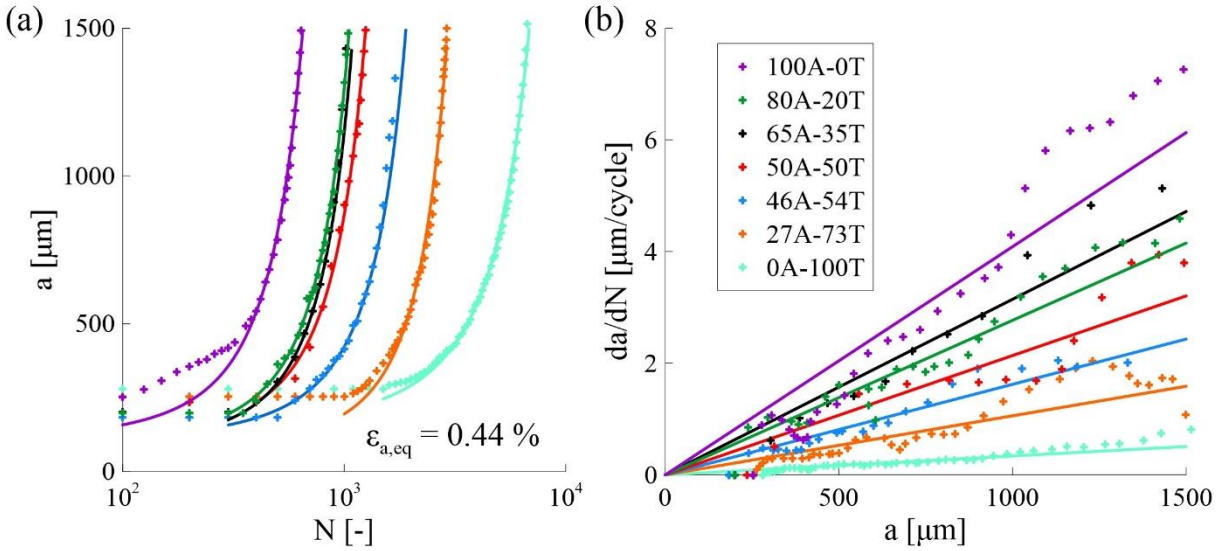

Fig. 67 Crack growth in cycling with $\varepsilon_{a,eq}$=0.44 %; OP mode with various A/T ratios (a) a as a function of N; (b) da/dN as a function of a.

Measured data were fitted using Eq. 39. Parameter k_g is shown in Tab. 15. Based on the knowledge from previous tests, it is reasonable to assume that the value of k_g should grow with increasing A amplitude. However, there are two deviations from this trend which can be observed from Tab. 15 as well as from Fig. 66 and Fig. 67. In particular, k_g corresponding to IP test 80A-20T is slightly higher than k_g corresponding to 100A-0T test and k_g obtained from OP test 65A-35T is higher compared to 80A-20T. The easiest explanation is an experimental scatter typical for fatigue tests due to metallurgical dispersion.

Tab. 15 Crack growth coefficient k_g from multiaxial tests with the same equivalent strain amplitude and variable A/T ratio.

A/T ratio	k_g *in* IP	k_g *in* OP
100A / 0T	4.09×10^{-3}	4.09×10^{-3}
80A / 20T	4.14×10^{-3}	2.77×10^{-3}
65A / 35T	3.63×10^{-3}	3.15×10^{-3}
50A / 50T	2.39×10^{-3}	2.14×10^{-3}
46A / 54T	1.96×10^{-3}	1.62×10^{-3}
27A / 73T	1.05×10^{-3}	1.06×10^{-3}
0A / 100T	3.38×10^{-4}	3.38×10^{-4}

Values of k_g listed in Tab. 15 are graphically compared in Fig. 68. Increasing torsional loading (decreasing A/T ratio) causes slower crack growth described by k_g. The curve representing IP mode is above the OP curve when T loading is low although they are getting closer with increasing T loading. The green cross represents A mode (0 % of T loading) while the black cross corresponds to T mode (100 % T loading).

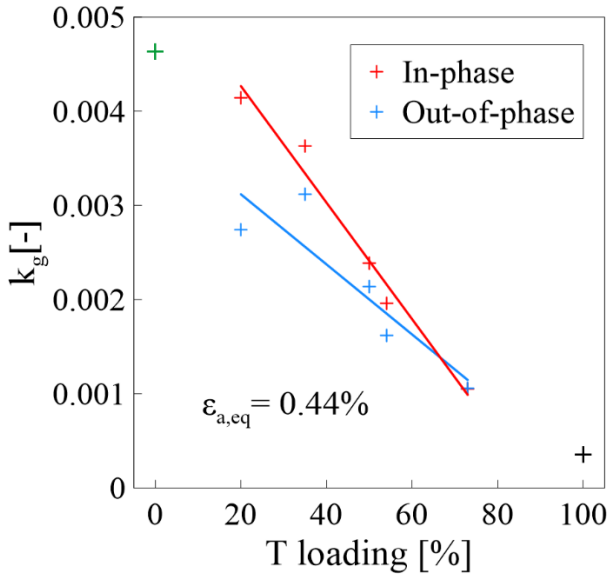

Fig. 68 Dependence of the parameter k_g on the A/T ratio. The green and black cross represent 100 % A and 100 % T mode, respectively.

Similarly to tests with the same A/T ratio, $t_{propagation}$ was calculated according to Eq. 41 also for the tests with various A/T ratio. The obtained results are graphically presented in Fig. 69. It is obvious that an increasing tendency of $t_{propagation}$ was observed in both modes. Higher values of $t_{propagation}$ were noticed in OP mode.

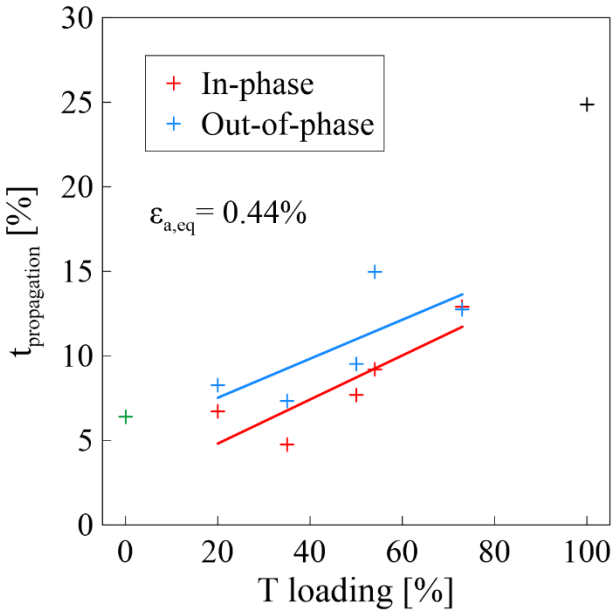

Fig. 69 $t_{propagation}$ as a function of the A/T ratio. The green and black cross represent 100 % A and 100 % T mode, respectively.

5.3.2 Analysis using J-integral

As described earlier in the Chapter 4.7, total and elastic J-integral was calculated for certain crack lengths using the finite element method. An example of the dependence of J_{total} and J_{el} on the crack length a may be seen in Fig. 70, the data presented in this figure were obtained from a specimen loaded in T mode with $\varepsilon_{a,eq}$ = 0.44 %. Datapoints corresponding to calculated values were approximated afterward. The rising trend of J_{total} and J_{el} is in line with expectations.

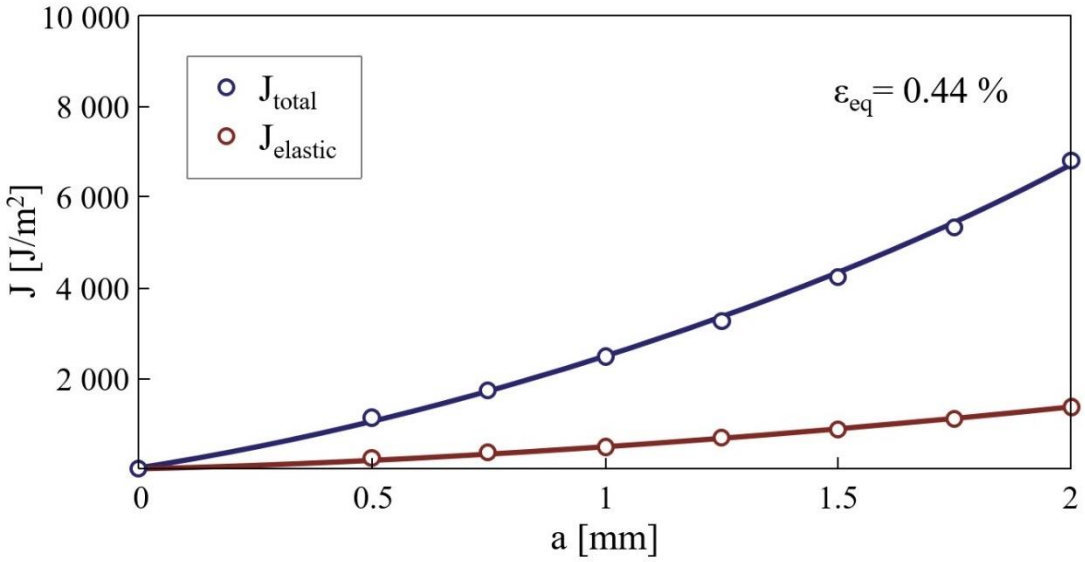

Fig. 70 Dependence of total and elastic J-integral on crack length calculated for T mode and $\varepsilon_{a,eq}$=0.44 % [118].

The following derivation of the plastic part of J-integral was fairly straightforward – see Eq. 35. The dependencies of J_p on a in the case of $\varepsilon_{a,eq}$ = 0.44 % applied in A and T mode are compared in Fig. 71. It is obvious that crack driving forces are significantly larger in the case of A mode. To be more specific, J_p in A mode was found to be approximately four times larger compared to J_p in T loading mode.

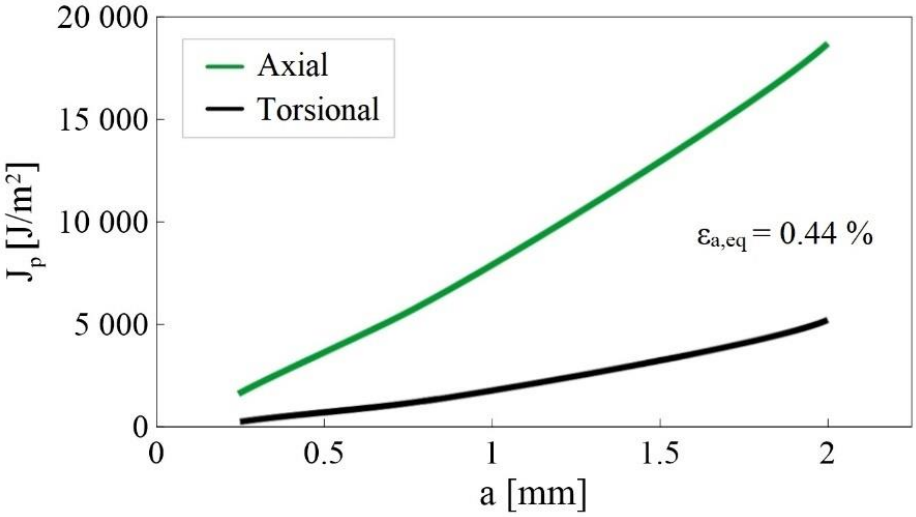

Fig. 71 Comparison of plastic J-integral of A and T mode for the same $\varepsilon_{a,eq}$ [118].

Fig. 72 shows the crack growth rate *da/dN* as a function of the amplitude of plastic J-integral $J_{p,a}$ in the case of A loading mode. All examined loading levels are depicted here. Datapoints from each amplitude were fitted separately. Since the scatter of data points is not large and obtained fitting curves lie close to each other, all data could be reasonably well approximated with a unique curve. The same procedure was performed also for T and IP mode – see [118].

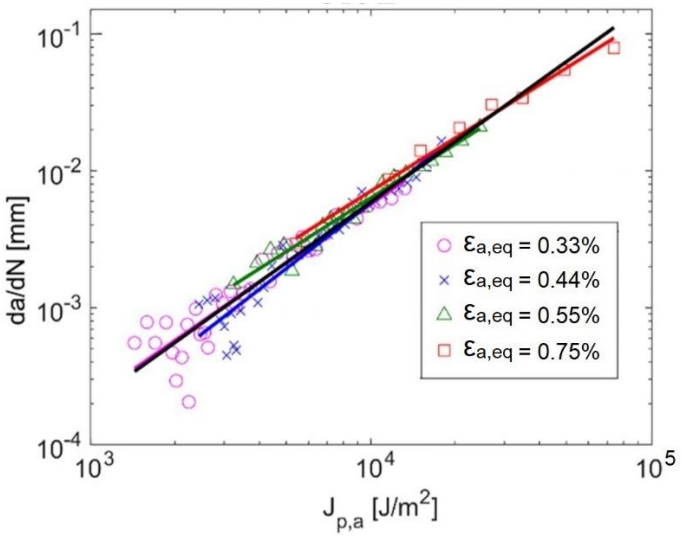

Fig. 72 Crack growth rate da/dN as a function of $J_{p,a}$ in A mode [118].

Fitting curves representing individual loading modes are shown in Fig. 73. It may be seen that using the master curve as a close approximation for all of them is appropriate because of their similar tilt and mutual position.

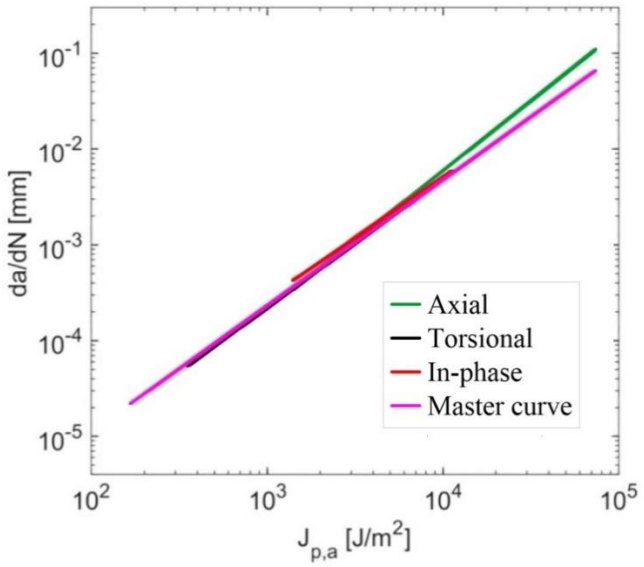

Fig. 73 Fitting lines of A, T, and IP mode and the master curve [118].

5.4 Fatigue life predictions

Cyclic hardening-softening curves presented in the section 5.1.2 demonstrated that $\sigma_{a,eq}$ might vary significantly throughout the fatigue life. Because the mechanical response of our experimental material usually does not exhibit a fatigue life phase where $\sigma_{a,eq}$ is stable, other representative cycles had to be selected as an input for the critical plane analysis: i) the half-life cycle and ii) the maximum softening cycle (see Fig. 37). Fatigue life predictions were performed using both approaches and their AER was compared afterward. Tab. 17 and Fig. 75 contain just the more accurate results (exhibiting lower AER). When more precise predictions were produced using the half-life cycle, the model is marked accordingly in Tab. 17. As mentioned earlier, no softening was detected when the mechanical response of OP test with $\varepsilon_{a,eq}$ = 1.00 % was analyzed ($\sigma_{a,eq}$ was rising from the first loading cycle until the moment when the principal crack started to propagate). Therefore, fatigue life of this test could not be predicted based on the analysis of the maximum softening cycle.

Predictions obtained using the BMC model are utilized as a benchmark for the remaining criteria. Fig. 74 contains a comparison of N_f predicted by the BMC model and N_f measured in experiments. The perfect N_f prediction would lie on the full line inclined by 45°. Dashed lines represent the factor-two-band. It may be seen that the BMC model produces fairly satisfactory results for A, IP, and OP loading since most predictions fell inside the factor-two-band. The model however fails when fatigue lives under T mode are predicted. It is comprehensible since the coefficients contained in the equation's right side were calibrated on results from A tests.

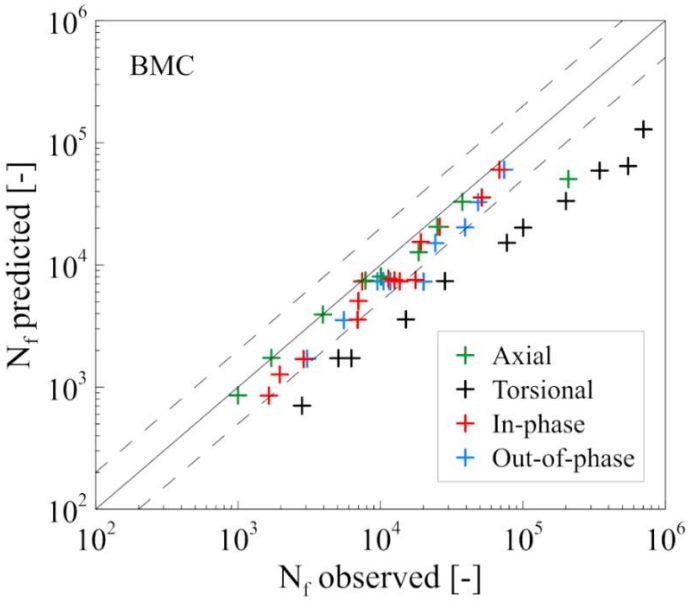

*Fig. 74 N_f predicted by Basquin-Manson-Coffin equation (*Eq. *4) vs. N_f observed.*

As stated earlier, an additional material parameter may be found in some criteria applied in the present study. Their values listed in Tab. 16 were determined by fitting experimental data to minimalize AER.

Tab. 16 Additional material parameters determined by fitting experimental data.

Model	Additional material parameter
FS (Eq. 6)	0.82
Li (Eq. 12)	2.15
MGSE Zhu (Eq. 17)	2.33
MSWT (Eq. 18)	0.49
WB (Eq. 5)	1.65
Zhu (Eq. 23)	0.00

To evaluate the accuracy of a particular critical plane model, two metrics were defined – AER described in the section 4.6, and the percentage of data points that fell within the factor-two-band. Both of them are listed in Tab. 17 which sorts the criteria in increasing order of AER.

Tab. 17 Accuracy of critical plane models (all loading modes included).

Model	AER [%]	Percentage of data points in factor-two-band [%]
FS (Eq. 6)	40.1	97.8
MSWT (Eq. 18)	51.2	82.2
GSE (Eq. 14)	103	60.0

Zhu* (Eq. 23)	111	71.7
WB (Eq. 5)	114	73.3
MKBM (Eq. 9)	125	57.8
BMC* (Eq. 2)	**140**	**68.9**
MGSE Zhu (Eq. 17)	150	42.2
MGSE Yu (Eq. 16)	150	55.6
Li (Eq. 12)	157	40.0
Chen II (Eq. 20)	191	51.1
Liu II (Eq. 22)	203	46.7
SWT* (Eq. 8)	251	67.4
Chen I* (Eq. 19)	310	50.0
Liu I* (Eq. 21)	312	50.0
GSA* (Eq. 15)	375	8.70

** model providing more accurate prediction when 0.5 N_f cycle was used*

Predicted and observed N_f of the ten most accurate models according to Tab. 17 are graphically compared in Fig. 75 (except the BMC model that was already presented in Fig. 74).

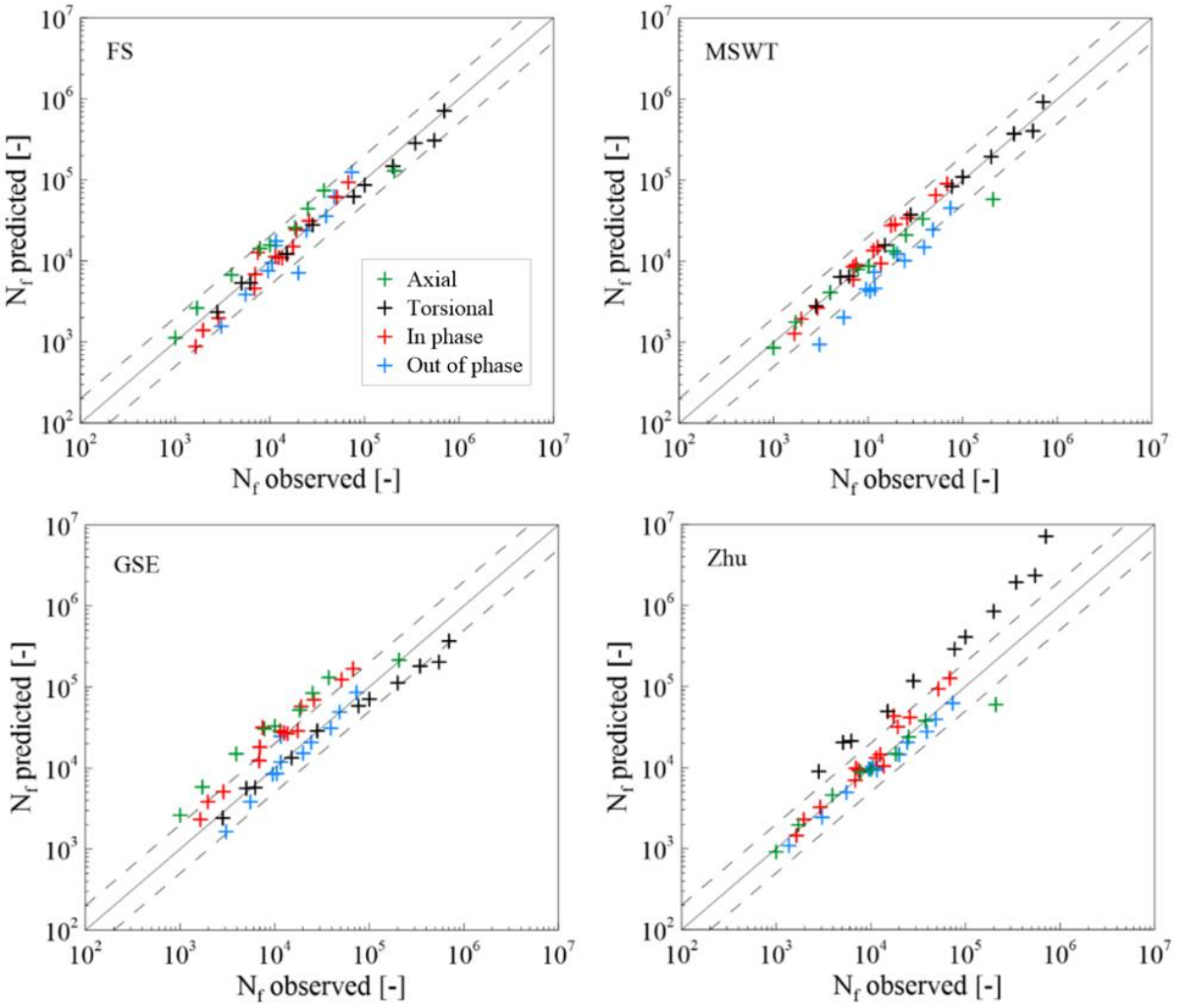

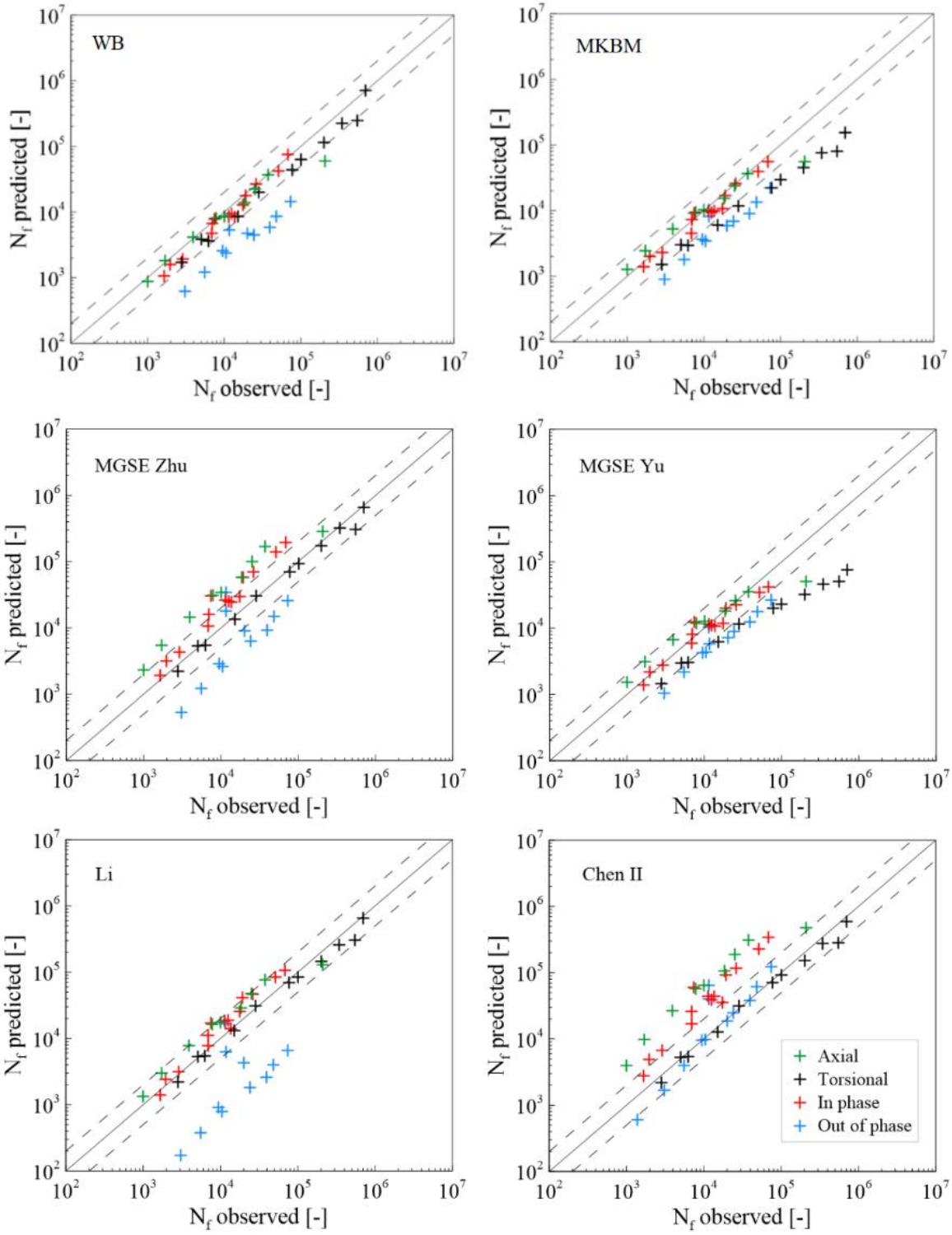

Fig. 75 Comparison of N_f observed in fatigue life experiments and N_f predicted by critical plane models.

5.5 Predictions of fatigue crack orientation

The following section is aimed at predictions of fatigue crack deflection based on the critical plane approach and to a comparison of obtained results with experimental data. The angle α defining the deflection is defined in Fig. 30. The first step in this process involves locating the critical plane, whose definition depends on the specific model being used. It is generally agreed upon in the literature that the principal fatigue crack grows in the plane that is closest to the

critical plane [58, 123]. Once the critical plane has been located, the next step is to determine an interval where the governing parameter reaches a value higher than 0.9 of its maximum [58, 123]. It is possible to locate multiple critical planes during the analysis, but no more than two planes were located in the present research. The comparison of predicted and measured crack orientations characterized by the angle α is depicted in Fig. 79. The prediction was performed for every model and equivalent strain amplitude.

Only one crack orientation was detected in A, IP, and OP loading modes. Cyclic loading in A mode led to the formation of a fatigue crack whose orientation was perpendicular to the specimen axis. A micrograph of the crack growing in A mode may be seen in Fig. 76.

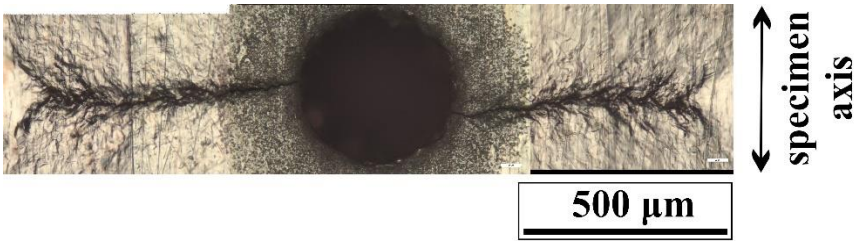

Fig. 76 The orientation of fatigue crack growing in A mode.

It is noteworthy that the direction of rotation during the initial half cycle determines the crack's direction in IP and OP modes. The crack was deflected by 30 degrees due to the application of an anti-clockwise rotation (see Fig. 77). However, if a clockwise rotation had been applied, the crack would have been oriented as a mirror image to the crack in Fig. 77. Fig. 79 displays both options, with full circles indicating the anti-clockwise rotation and empty circles demonstrating the clockwise rotation.

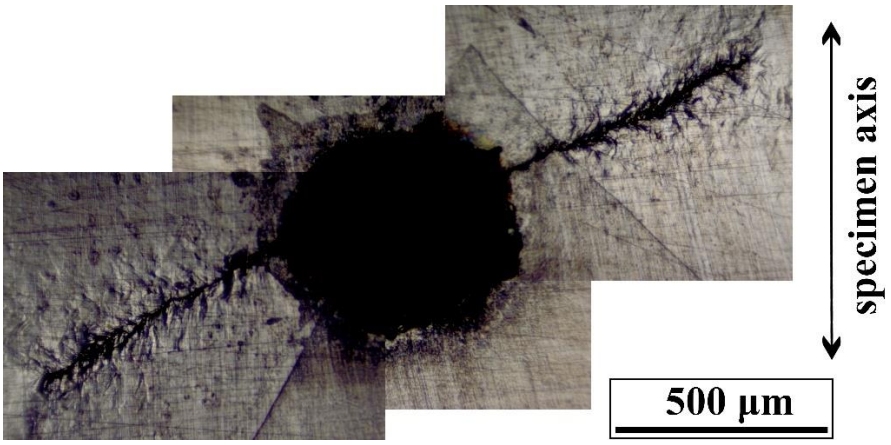

Fig. 77 The orientation of fatigue crack growing in IP mode.

Two perpendicular cracks forming an X shape were detected in T-tests. Both of them are identified in Fig. 79. The angle of deflection was close to 45 and 135 degrees, respectively. An example of fatigue cracks propagating under T loading is shown in Fig. 78.

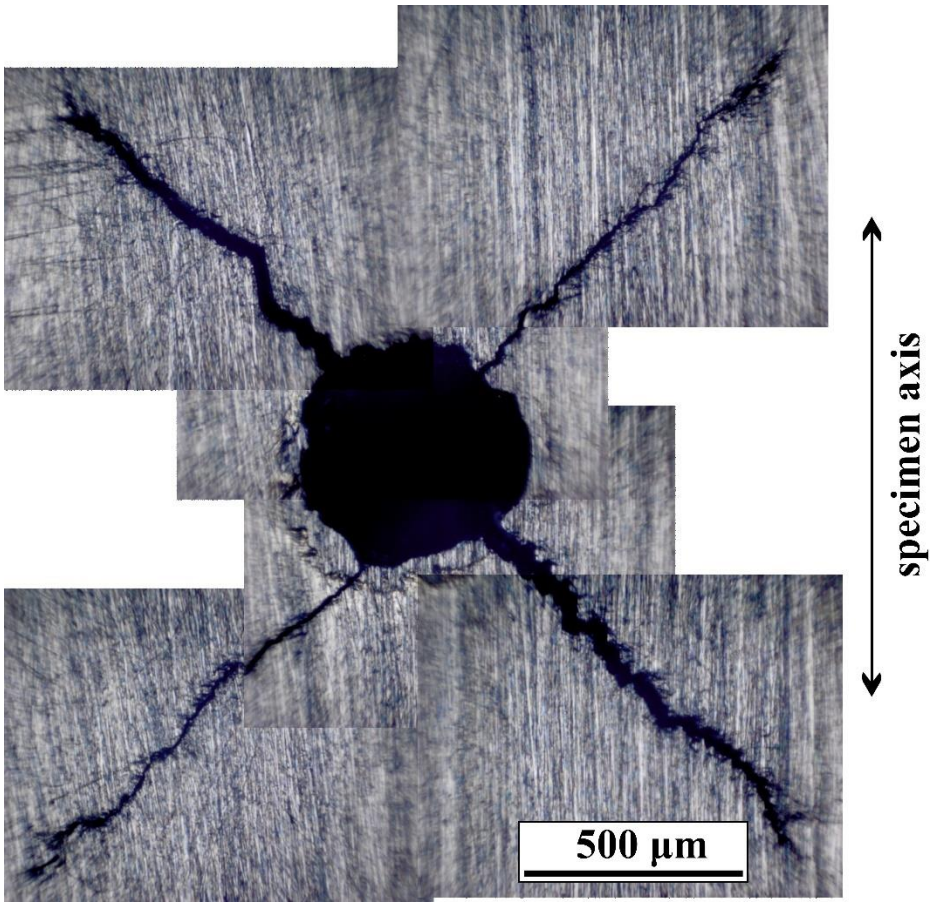

Fig. 78 The orientation of fatigue crack growing in T mode.

The models shown in Fig. 79 are arranged in increasing order of precision. Models that employ the same critical plane definition naturally produce identical predictions of the fatigue crack deflection.

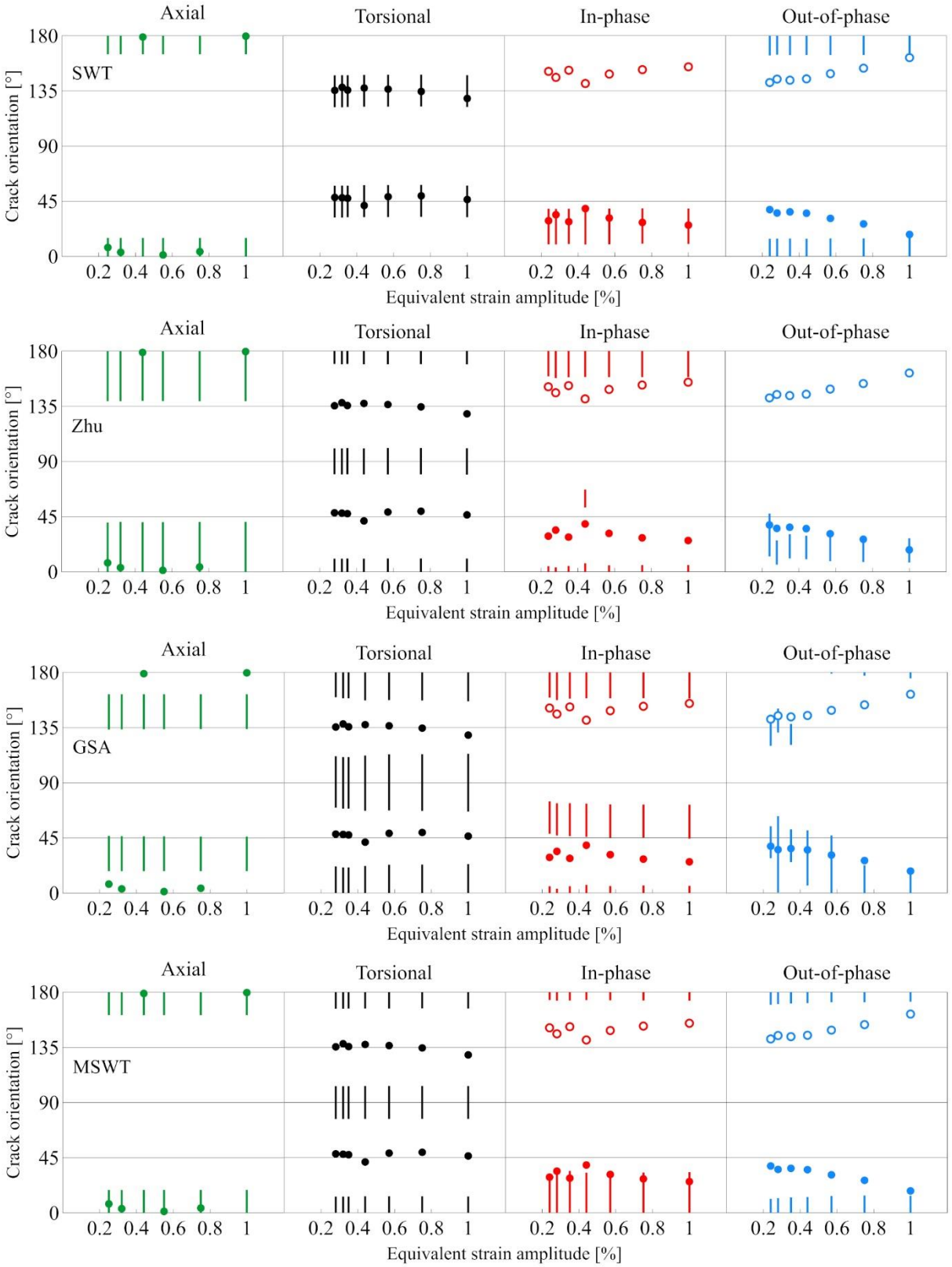
Axial
Torsional
In-phase
Out-of-phase
SWT
Zhu
GSA
MSWT
Crack orientation [°]
180
135
90
45
0
0.2 0.4 0.6 0.8 1
Equivalent strain amplitude [%]

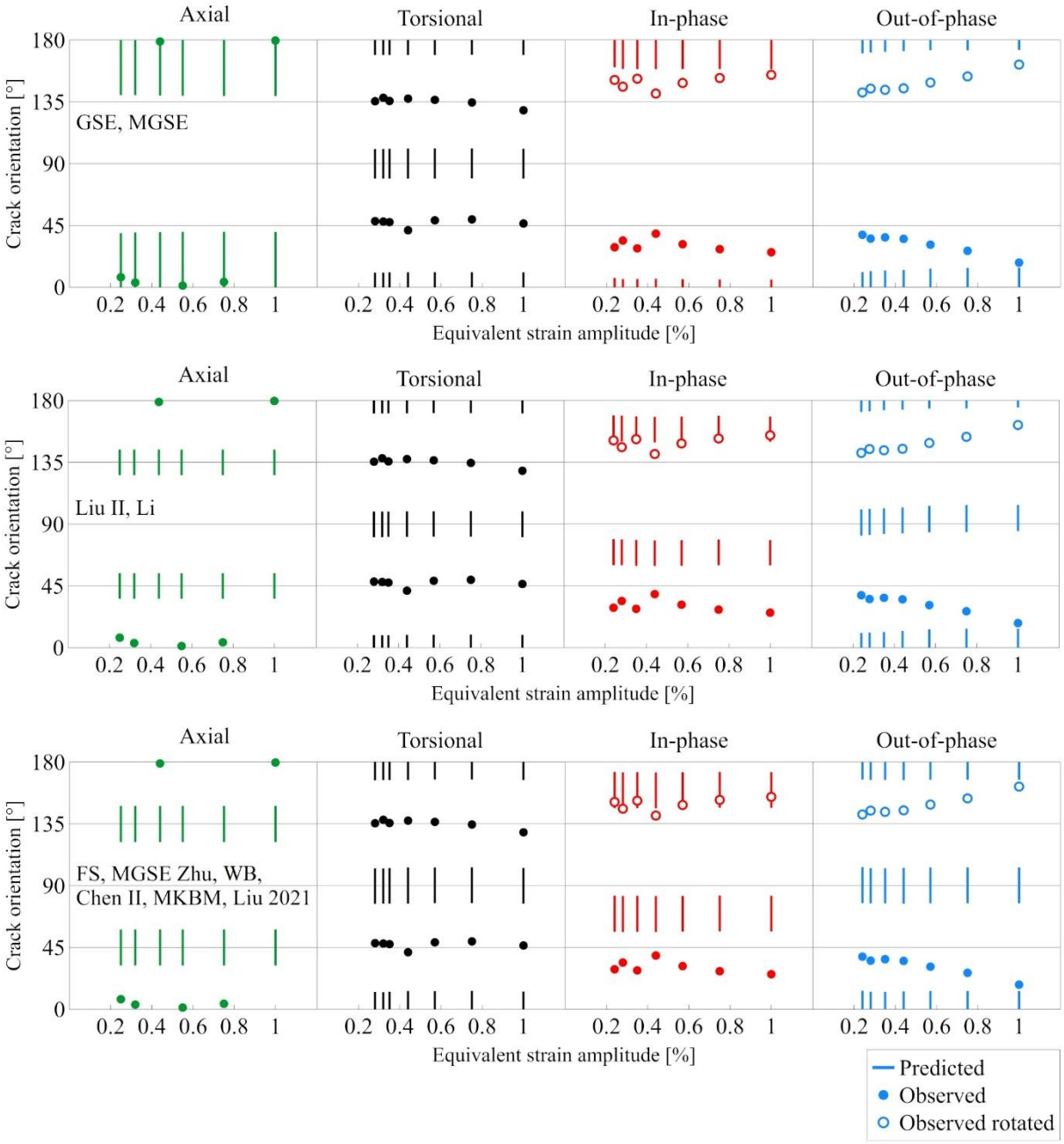

Fig. 79 Comparison of predicted and observed crack orientations [117].

6 Discussion

6.1 Fatigue life curves

The endurance of 316L steel against fatigue failure is demonstrated by fatigue life curves N_f = f ($\varepsilon_{a,eq}$) shown in Fig. 34. The longest fatigue lives were measured in T mode. On the other hand, cyclic loading in A mode was determined to be the most susceptible to fatigue damage. The ratio between N_f observed in T mode and N_f corresponding to the same $\varepsilon_{a,eq}$ in A mode was around three. According to a study from Facheris et al. [61], the T mode fatigue lives of 316L steel are twice as long as those in A mode, which is consistent with the results obtained by Bemfica et al. [58], who performed fatigue life tests using 304L steel. Their explanation was the following: the presence of a rough fracture surface caused increased frictional forces throughout the shear loading, which resulted in reduced stress and strain fields near the crack tip. This ultimately led to a slower rate of fatigue crack propagation and, consequently, to a longer fatigue life [61]. The same authors also found that the fatigue endurance was nearly identical in both A and IP modes. As may be seen in Fig. 34, the same trend was observed in our study since N_f obtained from testing in A and IP mode were comparable, particularly in the case of low loading levels.

Upon analyzing the fatigue life tests included in Tab. 6, a significant amount of non-proportional hardening in OP mode was noticed. It is however limited to loading levels higher than 0.44 %, as can be seen from Fig. 36 where the hardening/softening curve of OP mode is noticeably shifted towards higher stress levels. Fig. 34 suggests that endurance against fatigue fracture measured in OP and IP mode is almost identical. The observed non-proportional hardening is therefore not a reason for a fatigue life reduction. Results of several researchers [56, 69, 78, 124–126] were however found to be in contradiction with this statement since their conclusions indicate that non-proportional hardening causes lower fatigue endurance. Facheris et al. [61] cycled their samples in IP and OP mode with the same $\varepsilon_{a,eq}$ and revealed that N_f corresponding to OP mode was approximately 10 times lower compared to IP mode. This discrepancy could be partially attributed to a circular loading path of their OP mode. To be more specific, the OP mode used in this work depicted in γ-ε coordinates has a rhombus shape – see Fig. 31 and the non-proportionality factor calculated with Eq. 1 is lower than the factor of the circular loading path, respective values are 1.00 and 0.77. Results presented in mentioned papers suggest that loading paths exhibiting higher non-proportionality factor are causing larger non-proportional hardening which results in more pronounced reduction of fatigue life. Bemfica et al. [58] employed the circular loading path as well and an enormous difference in N_f was remarked when OP mode was compared with IP mode on the loading level $\varepsilon_{a,eq}$ = 0.30 %. The specimen cycled in OP mode was able to withstand 1 200 loading cycles while the IP loaded sample failed after 35 000 cycles. The difference was substantially lower when $\varepsilon_{a,eq}$ = 0.20 % was applied – 62 000 and 148 700 loading cycles were noted until the failure occurred in OP and IP modes, respectively. Dey et al. [33] utilized IP and OP rhombus loading paths in their study. Experiments were performed using specimens from 304LN steel. Their results also exhibited a tendency towards reduction of N_f in OP mode. It was however much weaker than those presented by Facheris et al. [61]. Fatigue lives in OP mode measured by Dey et al. [33] were approximately half of N_f corresponding to IP loading.

Mazánová et al. [127] conducted research aimed at the initiation of fatigue cracks under multiaxial loading and discovered that the mechanism of fatigue crack initiation is the same for both IP and OP modes. However, the mechanism of fatigue crack propagation under cyclic multiaxial loading is still not well understood.

6.2 Hardening/softening curves

The results summarized in Tab. 7 show that the shapes of cyclic hardening/softening curves are dependent on the loading mode and the amplitude of loading. Applying low strain amplitudes caused weaker initial hardening, pronounced softening phase, and negligible secondary hardening. The opposite trend was observed in the case of high strain amplitudes – substantial initial and secondary hardening were noted while softening phase was less intense. The response under A and IP loading mode was found to be comparable – the only observable difference was a stronger tendency towards secondary hardening in IP mode. A characteristic feature of T mode was intense secondary hardening even in the case of moderate strain amplitudes. On the other hand, stronger and prolonged initial hardening was noted in OP mode.

Since our material was hot rolled, a moderate dislocation density may be expected in the as-received microstructure. This presumption was confirmed by TEM observations presented in the Chapter 5.2.2. The growth of the dislocation density at the beginning of fatigue tests led to so-called initial hardening. After the dislocation density was increased, dislocations subsequently tended to rearrange into structures enabling their easier movement leading to a decrease in applied stress. The softening observed during the cycling of 316L steel is usually explained by a formation of persistent slip bands (PSBs) [15, 18, 32] enabling an easier slip of dislocations leading to lower stress needed for reaching of given strain level. In the studied material, persistent slip marking are formed on the surface during cycling. The internal dislocation structure corresponding to the surface markings is discussed in section 6.5. The last phase of fatigue life, preceding the propagation of the principal crack, is called secondary hardening. The presented results suggest that its cause may be found in the formation of strain-induced α′ martensite. This phenomenon is thoroughly discussed in section 6.4.

Mazánová et al. [127] observed the same three stages of the stress amplitude evolution during multiaxial cyclic loading of 316L steel as well as Li et al. and Bemfica et al. [49, 58] who examined 304L steel. There are also papers whose authors reported missing or weak secondary hardening phase. Facheris et al. [61] did not record any sign of secondary hardening when studying the mechanical response of 316L steel cycled in A, T, IP, and OP mode with $\varepsilon_{a,eq}$ = 0.65 %. The occurrence of secondary hardening was observed in the case of A and T loaded specimens with $\varepsilon_{a,eq}$ = 1.00 % (IP and OP loading with $\varepsilon_{a,eq}$ = 1.00 % was not applied in their study). Jin et al. [128] also examined the cyclic stress behavior of 316L steel and found that secondary hardening occurs only in OP and T mode using $\varepsilon_{a,eq}$ = 1.00 %. Evolution of stress amplitude corresponding to specimens cycled with $\varepsilon_{a,eq}$ = 0.70 % did not exhibit a secondary hardening phase. Dey et al. [33] chose 304LN steel in their study and applied IP, OP, and A loading mode using four equivalent strain amplitudes (0.5; 0.7; 0.8 and 1.0 %). The tendency towards secondary hardening was noticed only in the case of OP loading using $\varepsilon_{a,eq}$ = 1.00 %.

The reason for different mechanical response using the same type of material is caused by a relatively wide range of nickel content allowed for austenitic steels. Nickel is probably the most commonly used element stabilizing austenite and it's lower content leads to a weaker resistance of austenite towards phase transformation to strain induced α′ martensite [129]. Above mentioned papers from Facheris et al. [61] and Jin et al. [128] were dealing with 316L steel whose nickel content was 12.5 wt.% and 12.0 wt.%, respectively. On the contrary, 316L steel used in the present study and in the study of Mazánová et al. [127] contained only 10.0 wt.% of nickel. Another alloying element increasing the phase stability of austenite is nitrogen [129]. An increased amount of nitrogen is a characteristic feature of 304LN steel used by Dey et al. [33] (contrary to 304L steel used by Li et al. [49] and Bemfica et al. [58]). The presence of α′ martensite in the microstructure subdued to cyclic loading was confirmed by all authors reporting a strong tendency towards secondary hardening [49, 58, 127].

6.3 Hysteresis loops, CSSC, and S-N curves

To eliminate the effect of strain induced martensitic transformation, the Masing behavior was investigated using hysteresis loops from the maximum softening cycle (it is believed that the amount of α′ martensite is negligible before the start of the secondary hardening phase [58]). Another assumption for an occurrence of the Masing behavior, besides the consistent phase composition, is the development of the same dislocation structures regardless of the loading level [130]. TEM analysis described further in the Discussion revealed that the arrangement of dislocation is strongly dependent on the applied strain amplitude. The absence of the Massing behavior observed in the present study is therefore comprehensible. On the contrary, results shown in the study from Bemfica et al. [58] who investigated the mechanical response of 304L steel in various loading modes revealed the presence of the Masing behavior in A and T mode (up to $\varepsilon_{a,eq}$ = 0.35 %) but also in IP mode (up to $\varepsilon_{a,eq}$ = 0.50 %). Roy et al. [131] and Goyal et al. [132] performed an analysis of hysteresis loops obtained by cyclic straining of 316LN steel in A mode and observed the Masing behavior in the case of low amplitudes (up to $\varepsilon_{a,eq}$ = 0.50 %). The likely cause is a lower tendency towards cross-slip of 316LN steel confirmed by numerous authors [3, 4, 22–24].

As mentioned earlier, there is a significant change in the trend of hardening/softening curves presented in Fig. 36 when $\varepsilon_{a,eq}$ reaches 0.44 % (the curve of OP mode gets clearly above the remaining curves). This behavior is the reason for the substantially different slope of the S-N and CSSC curve corresponding to OP mode when compared with other loading paths as shown in Fig. 39 and Fig. 40, respectively. The same tendency in CSSCs was observed by Mazánová et al. [59]. This phenomenon is caused by the distinct dislocation structure developed under conditions of non-proportional loading and $\varepsilon_{a,eq}$ higher than 0.44 %. Arrangements of dislocations observed in particular loading modes and amplitudes are thoroughly discussed in section 6.5.

6.4 Formation and distribution of α′ martensite

The occurrence of strain-induced phase transformation of metastable austenite to α′ martensite was confirmed by all utilized techniques, i.e. TEM, EBSD and the Feritscope. The extent of this transformation depends on the applied strain amplitude and loading mode. The measured values listed in Tab. 10 and Tab. 11 indicate that the transformation is easier when a high loading amplitude is applied. The lowest amount of α′ martensite was induced in A mode. The conclusions regarding other modes are rather problematic. Both methods detected the highest α′ martensite content in T mode when samples cycled with $\varepsilon_{a,eq}$ = 0.57 % were examined. The results regarding $\varepsilon_{a,eq}$ = 0.24 and 1.00 % are however fairly equivocal, e.g. EBSD detected only negligible content of α′ martensite in all loading modes when $\varepsilon_{a,eq}$ = 0.24 % was applied. The Feritscope, on the other hand, measured over 5 vol.% in T mode. The situation is even more inconsistent in the case of $\varepsilon_{a,eq}$ = 1.00 % because 12.0 and 18.4 vol.% was measured in T and OP mode by EBSD while 42.0 and 46.6 vol.% was detected by the Feritscope. The Feritscope measurements exhibit substantially higher values of α′ martensite volume fraction. This discrepancy is probably caused by a combination of the following two factors.

1) The EBSD technique is not able to detect α′ martensite islands whose size is smaller than the step size. The aim of the presented EBSD analysis was to analyze the distribution of α′ martensite across the sample wall. The size of the analyzed area was therefore considerably large, equal to 1 mm^2 (2 x 0.5 mm). The step size naturally influences the time needed for the analysis. Therefore, a reasonable step size had to be chosen to complete the analysis in an acceptable time. It's value was set to 0.3 μm (the analysis than required approximately 6 hours

to be completed). The TEM observations however revealed a presence of α′ martensite islands whose dimension is under this limit, they may be seen in Fig. 80.

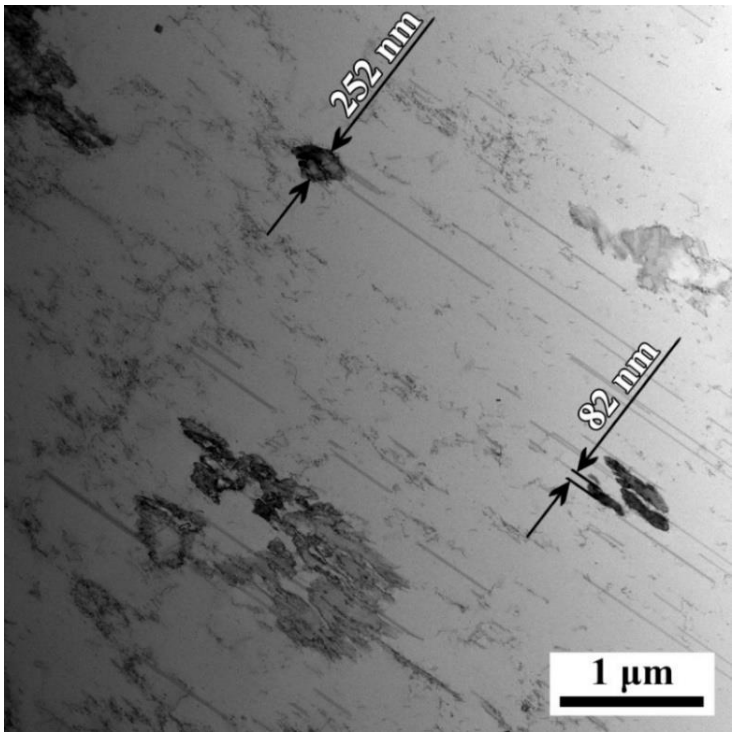

Fig. 80 α´martensite islands observed in the specimen cycled in T mode using $\varepsilon_{a,eq}$ = 0.24 %.

The insufficient susceptibility of EBSD for our case may be demonstrated on the data from OP fatigue life test with $\varepsilon_{a,eq}$ = 0.57 %. The analysis of corresponding hardening/softening curve revealed the occurrence of secondary hardening whose intensity was quantified to 5.6 % (see Tab. 7). Although the amount of α′ martensite measured by EBSD was equal to 0.0 vol.%. On the contrary, the Feritscope measurements revealed 7.5 vol.% of α′ martensite. As mentioned earlier, the correlation between strain-induced martensitic transformation and the appearance of secondary hardening was confirmed by several researchers [49, 58, 127].

2) According to the literature, the volume analyzed by the Feritscope is approximately 10 mm^3 [133, 134] which corresponds to a cube with 2.15 mm edge or a sphere whose diameter equals 2.67 mm. The thickness of the gauge length wall of our specimens was equal to 2 mm – see Fig. 29. It is therefore reasonable to assume that the whole thickness was included in the Feritscope analysis. Obtained results however seem to be fairly overestimated in some cases. For instance; the amount of α′ martensite measured in OP mode in the case of $\varepsilon_{a,eq}$ = 1.00 % was 46.6 vol.% and the corresponding value of SH_I was 20.0 %. A comparably intense SH_I (17.3 %) was noted also in the case of IP mode when the same $\varepsilon_{a,eq}$ was applied (see Tab. 7) even though only 11.8 vol.% of α′ martensite was induced according to the Feritscope. The reason may be found in significantly more heterogeneous distribution of α′ martensite under OP loading when compared to IP mode (see Fig. 45). To be more specific; measurements were presumably affected by the fact that most of the α′ martensite phase was induced near the specimen surface where the Feritscope measurements were performed. This aspect should be taken into account when samples subjected to loading involving torsion are analyzed with the Feritscope.

A relation between strain amplitude and the content of induced α′ martensite was confirmed by several authors in the case of axial loading [35, 44, 45, 135]. All of them concluded that higher

strain amplitude leads to a higher content of α′ martensite in the microstructure. On the contrary, papers discussing the effect of loading path on the content of α′ martensite are rare.

Li et al. [49] performed in situ measurements using Feritscope to measure a volume percentage of α′ martensite during cyclic loading. Eight loading paths with $\varepsilon_{a,eq}$ = 0.50 % were applied and the following conclusion was made: the amount of α′ martensite measured at a given cumulative plastic strain level increases with the non-proportionality of the loading path (calculated by Itoh et al. [136]). The highest content of α′ martensite measured post-mortem was observed in T and OP mode with the cross path (up to 40 vol.%). This finding coincides with our observations since the highest volume of α′ martensite was measured in T and OP mode. On the other hand, the authors also reported that the amount of α′ martensite measured in A, IP and rhombus OP mode was between 10 and 15 vol%. The content of α′ martensite measured by the Feritscope in the case of specimens cycled in A, IP and OP mode with $\varepsilon_{a,eq}$ = 0.57 % is considerably lower in the present paper (between 2.0 and 7.5 vol.%). It is worth noticing that Li et al. [49] used 304L steel and the content of nickel in their material was lower (8.05 wt.%) so a worse resistance against martensitic transformation may be expected.

Mazánová et al. [32] performed post-mortem feritscope measurements of α′ martensite induced in 316L steel by cyclic loading. Their specimen cycled in T mode with $\varepsilon_{a,eq}$ = 0.40 % exhibited 12 vol% of α′ martensite. Their IP and OP specimens were cycled with $\varepsilon_{a,eq}$ = 0.35 % and the measured content of α′ martensite was 3.6 and 1.6 vol.%, respectively. All of their results are compatible with those presented in this thesis.

Dey et al. [33] used the EBSD technique for analyzing the content of α′ martensite in 304LN steel cycled in OP mode with $\varepsilon_{a,eq}$ = 1.00 %, the analyzed area contained only 3.5 vol.% of α′ martensite. Their sample designated for the EBSD analysis was however cut along the gauge length from an unknown depth. The results shown in the present study clearly demonstrated that this approach is inappropriate and may lead to misleading results.

6.5 Dislocation structures

The performed TEM observations are summarized in Fig. 60 and Tab. 12. The following conclusion could be drawn: i) post-mortem arrangement of dislocations is dependent on applied strain amplitude; ii) cycling in A, T, and IP mode on a given level of $\varepsilon_{a,eq}$ led to a formation of similar dislocation structures while a substantially different arrangement of dislocations was revealed in OP mode.

Fig. 60 and Tab. 12 provide an explanation of the distinct mechanical response of 316L steel under OP loading with $\varepsilon_{a,eq}$ > 0.32 %. The hardening/softening curves obtained from these tests exhibit substantially different shapes comparing to the other curves, characterized by longer and more intense initial hardening phase and less pronounced softening phase. Since the hardening/softening curve is shifted to higher stress values, the stress amplitudes corresponding to the half-life and the maximum softening cycle thus have larger values as well which directly affects the CSSC and S-N curves.

The reason may be found in an arrangement of dislocations into structures where their slip becomes more difficult. While the veins and primary walls prevailed in the case of A, IP, and T mode subjected to $\varepsilon_{a,eq}$ = 0.32 %, the secondary walls and the labyrinth structure were formed predominantly in OP mode. A similar situation was noted when TEM foils prepared from A, IP, and T samples cycled with $\varepsilon_{a,eq}$ = 0.44 and 0.57 % were examined. However, vein structures become less frequent meanwhile primary walls were more common as the amplitude increased. The labyrinth structure was still prevailing in the case of OP mode. A different arrangement of dislocations were observed in the case of $\varepsilon_{a,eq}$ = 1.00 %. Primary walls were partly preserved in

A and IP samples. Equally oriented cells were formed in all loading modes. They were found most often in T loaded samples. Relatively high loading amplitude caused disorientation of some dislocation cells. The proportion of disoriented cells was conclusively the highest in the case of OP mode.

A comparison of observed TEM structures with the results of other authors is fairly complicated because the number of studies dealing with dislocation structures developed in austenitic steels due to multiaxial fatigue is considerably limited. It has been however studied under conditions of uniaxial loading [2, 15, 18, 137]. Gerland et al. [2] studied post-mortem dislocation structures of annealed 316L-type steel. They concluded that the microstructure formed due to cycling with low $\varepsilon_{ap,eq}$ consisted mainly of dislocation tangles. Increasing of plastic strain amplitude resulted in the formation of cells while tangles were found less frequently. The authors also investigated the evolution of dislocation structure during fatigue life applying $\varepsilon_{ap,eq}$ = 0.50 %. The cellular structure was formed after a few hundred cycles and the area covered by cells continuously increased. Their walls become more condensed and a misorientation of cells was noted close to the end of fatigue life. PSBs with ladder-like structure were found very rarely (only in 2 % of examined grains). This observation is in contrast with studies performed by Kruml et al. [18] and Obrtlík et al. [15] who observed frequent PSBs in annealed 316L steel cycled with $\varepsilon_{ap,eq} > 4 \times 10^{-4}$. Their density was further growing with increasing amplitude of loading. Since the cyclic slip is easier within these bands, plastic strain is localized into PSBs. The surface relief caused by an intersection of PSBs with the sample surface is often called persistent slip markings (PSMs). Numerous studies [59, 138, 139] confirmed that PSMs are the initiation sites of early fatigue cracks. Both studies [15, 18] revealed that low amplitude of loading resulted in low dislocation density and planar arrangement of dislocations. Intermediate amplitude led to the formation of vein and wall structure meanwhile disoriented and equally oriented cells were found in the case of the high amplitude of loading. This finding is consistent with results from A, T, and IP loading modes shown in the present study.

One of the very few TEM studies dealing with multiaxial loading was published by Mazánová et al. [32] who aimed at dislocation structure developed in cold rolled 316L steel after cyclic straining in T, IP, and OP mode. The results by Mazánová are summarized in this paragraph as follows. The sample subjected to T loading was cycled with $\varepsilon_{a,eq}$ = 0.30 % while $\varepsilon_{a,eq}$ = 0.35 % was applied in the case of both multiaxial modes. The TEM foil fabricated from the T loaded sample exhibited the following features: 67 % of examined grains contained a well-developed ladder-like structure of PSB where dislocation walls alternate with dislocation-free channels. PSBs were often separated by areas exhibiting high dislocation density with no apparent spatial arrangement. These regions resemble the as-received microstructure after cold rolling. PSBs were found to be a preferential site for nucleation of α′ martensite whose presence was revealed in all examined grains. A distinct dislocation structure was found in 40 % of grains. It consisted of well-developed but irregular walls alternating with dislocation-free channels. Dislocation cells were observed very rarely (only in 7 % of examined grains). The dislocation structure developed due to IP loading was similar to that observed in the case of T mode. The dislocation structure was predominantly formed by PSBs surrounded by the matrix exhibiting high dislocation density. The irregular walls however become less frequent while dislocation cells were observed more often. In contrast to the T sample, some grains, free of α′ martensite, were noticed. A more distinct microstructure was reported in the case of OP mode. The equally oriented cellular structure become more common and was observed in 29 % of grains. Most examined grains could be characterized by the perfect wall/channel structure arranged into PSBs. Loading the sample under non-proportional conditions leads to an activation of multiple slip systems which alternate during every loading cycle. It causes the

formation of PSBs with distinct orientations. The intersection of differently oriented PSBs was found to be an initiation site for strain induced martensitic transformation.

On the contrary, no clear ladder-like structures were noticed during our TEM observations. It is probably caused by the various nitrogen content or by differences in the as-received microstructure. The 316L steel studied by Mazánová et al. [32] contained 0.078 wt.% of N meanwhile only 0.042 wt.% of N was measured in our material. The effect of nitrogen on SFE and dislocation structures has been already studied [3, 140]. It was found that increased content of N leads to a higher tendency towards planar slip. In this case, the lower nitrogen content caused the formation of stable spatial structures like dislocation cells, which were observed very often in this work. Secondly, a different as-received microstructure of the steel studied by Mazánová may be expected due to cold rolling. The initial dislocation density directly influences the evolution of the dislocation structure. When the density is low, the movement of dislocations is easier and the evolution takes part in the whole volume of the material. High dislocation density, on the other hand, causes more difficult dislocation movement and their rearrangement thus occurs only in the fraction of the material volume, namely in areas where the slip of dislocations is easier. The resulting microstructure is therefore consisted of regions resembling the as-received structure and zones exhibiting easier movement of dislocation (PSBs) as reported in [32].

Another study dealing with TEM observations of multiaxially fatigued samples was performed by Dey et al. [33] who chose 304LN steel as the experimental material. Four strain amplitudes were used for cycling in IP and OP modes. TEM samples were however prepared only from the tests with $\varepsilon_{a,eq}$ = 1.00 %. The authors reported a presence of incomplete cellular structure and planar arrangement of dislocations in the case of IP loading. Contrary to OP mode which led to the formation of well-defined dislocation cells. The distinction between observed structures was explained by an activation of multiple slip systems in the case of OP loading.

6.6 Crack growth kinetics

The CGR tests revealed that fatigue cracks propagate the fastest in A mode comparing tests performed in different modes at the same $\varepsilon_{a,\mathrm{eq}}$. On the contrary, the slowest rate of fatigue crack growth was observed in T mode. Both multiaxial loading paths exhibited comparable CGR however IP mode proved to be more damaging when low strain amplitudes were applied, see Fig. 64. The effect of various A/T ratios and constant $\varepsilon_{a,eq}$ was studied for IP and OP mode. The results obtained from both modes are in accordance with those attained from uniaxial tests, meaning that higher T strain amplitude led to lower CGR.

Our results partially confirmed the hypothesis saying that cyclic loading with higher $\varepsilon_{a,\mathrm{eq}}$ causes a faster initiation of the fatigue crack [141]. In other words, a larger part of the FL is spent by the crack propagation when higher $\varepsilon_{a,\mathrm{eq}}$ is applied. This behavior was observed only in the case of A, IP and T loading. OP mode, on the other hand, exhibited a constant value of $t_{propagation}$ regardless the strain amplitude - see Fig. 65. Results presented in Fig. 65 are in accordance with those shown in Fig. 64, meaning that loading mode with the lowest CGR expressed as k_g corresponds to the mode exhibiting the highest value of $t_{propagation}$ and vice versa. The same also applies for the results presented in Fig. 69 and Fig. 68, respectively.

The analysis based on the crack growth coefficient k_g does not provide a universal description of the CGR for all loading modes; the curve of the T mode is shifted to substantially lower k_g with respect to the remaining modes (as shown in Fig. 64).

However, the comparison of Fig. 64 and Fig. 73 demonstrated that the J-integral approach proved to be more suitable and versatile for the description of crack growth kinetics under various loading conditions. The curves received by fitting the data from individual loading

modes could be well approximated with a single master curve. This is a very important and original finding, which suggests that the CGR is controlled by the plasticity mechanisms at the crack tip; the same extent of the plasticity led to the same CGR, irrespective of the loading mode. This finding thus opens a way for general description of the crack growth propagation during fatigue and for improved possibility to predict crack growth rate in multiaxial fatigue.

A clear drawback of the J-integral approach is a substantially more complicated computation of $J_{p,a}$ in the case of OP loading. To be more specific, the computation of $J_{p,a}$ in the case of proportional loading was fairly straightforward. It consisted of loading the FEM model with the maximum A and/or T loading which occurred at a given moment of the loading cycle. The difference between computed values of J_{total} and J_{el} is equal to the amplitude of the plastic J-integral $J_{p,a}$. The situation is however more complex in the case of a non-proportional loading scheme because the moment of the maximum J_{total} and J_{el} occurrence is unknown. It could be found by a computing $J_{p,a}$ in every moment of the loading cycle (our loading cycle consists of 400 data points). This approach is thus time-consuming and more than one test have to be evaluated for the construction of the OP fitting curve. The calculation of ΔJ_{total} under conditions of non-proportional loading has been performed by Döring et al. [142]. Certain assumptions and simplifications were however taken into consideration and a simple specimen geometry was used. The advanced modeling for the calculation of $J_{p,a}$ in non-proportional cyclic loading has not been reported in the literature yet.

6.7 Critical plane models

It is worth mentioning that fatigue life is a fairly complex process as suggested in Fig. 1 and different micro-mechanisms are applied in particular stages. For instance, studies of Polák [143, 144] indicate that a production and annihilation of point defects play the major role throughout the fatigue crack initiation. Plastic processes at the crack tip proved to be essential during the growth of short fatigue cracks [115] and so on. Since all these processes cannot be described by a simple model, the description of fatigue life using single equation operating with macroscopic characteristic are therefore inevitably simplistic.

As may be seen from the cyclic hardening/softening curves presented in section 5.1.2, there is usually no stage of fatigue life with a stable stress amplitude in the mechanical response of 316L steel subjected to repeated straining. Therefore, some representative hysteresis loops for fatigue life prediction had to be selected. Life predictions were performed using the cycle from i) the half of the fatigue life and ii) the maximum softening. Many studies [49, 58, 127] have reported the occurrence of secondary hardening in 316L or 304L steel due to strain-induced martensitic transformation. According to the literature [58], the microstructure should be almost free of α′ martensite at the moment when the maximum softening cycle occurs. Obtained results however do not provide an unequivocal recommendation since applying the half-life loop yielded more accurate predictions for five models. Meanwhile, using the maximum softening cycle proved to be a better option for the other ten criteria. The relative difference between predictions based on the maximum softening cycle and the half-life cycle was found to be 7.2 %. An analogous comparison was performed by Bemfica et al. [58]. They also concluded that both approaches yielded similar predictions.

The FS model was found to be the most accurate critical plane model for fatigue life prediction of 316L steel. A comparable precision in terms of AER was achieved also with the MSWT criterion but fewer predictions fell inside the factor-two-band. The AER detected for the remaining criteria is significantly higher (see Tab. 17). GSE, Zhu, and WB models exhibited similar AER but predictions based on the GSE model are more likely to fall outside the factor-two-band. On the other hand, the GSE model is free of additional material parameter. This aspect makes the criterion more versatile and easier to use. Another model that does not

contain the material parameter is the MKBM criterion. Its accuracy is however lower compared to the GSE model. Predictions based on FS, MSWT, WB, and MKBM models were found to be mostly conservative. On the other hand, GSE and Zhu criteria yielded predominantly non-conservative predictions. Fatigue life predictions provided by every other criterion exhibited AER higher than the BMC equation. It may be stated based on Tab. 17, that criteria which include the additional material parameter provide more precise predictions of the fatigue life. It is logical and anticipated that fitting the parameter to a particular dataset enhances the precision of predicted fatigue lives. The practical application of criteria that include an additional material parameter is somewhat limited since the value of this parameter must be identified when not already known in advance. It should be emphasized that the assessment of critical plane models was based on symmetrical fatigue tests without mean stress. A different accuracy should be expected if fatigue endurance under non-zero mean stress loading was analyzed. The damage parameter of the WB model, specifically, is solely calculated from strain. It is therefore incapable of considering the impact of mean stress. Consequently, it is unsuitable for predicting fatigue life under loading conditions with zero mean stress.

The material parameters of critical plane models are physically grounded and generally account for the impact of factors like shear/normal strain or strain energy density on fatigue life. Nevertheless, conclusions drawn from these parameters are frequently inconsistent. The Zhu model yielded the most precise predictions for $\xi_{Zhu} = 0$, which is typical for materials exhibiting a tendency towards tensile cracking. The optimal value of MSWT model's parameter was found to be 0.49, authors claimed that a mixed cracking behavior may be expected when a_{MSWT} is close to 0.5. The Li model considers the influence of normal strain energy density on the fatigue life using the weight index L_{Li} and its value was found to be relatively high. A similar tendency was noted for MGSE Zhu's parameter describing how normal strain energy affects the growth of the fatigue crack. The model proposed by Fatemi and Socie was initially intended for materials cracking according to shear mode. The shear cracking behavior, therefore, explains the fact that the best predictions of fatigue endurance were achieved with the FS model. It is also supported by the fact that our experimental material exhibits significant ductility and ductile materials tend to crack according to shear mode.

Recently proposed as well as traditional criteria were adapted in our study. Papers applying the new criteria are very rare, essentially it is impossible to find a such study in most cases. On the contrary, traditional models like FS, WB, or SWT have been established as a benchmark for novel criteria. It is consequently relatively easy to find a paper where fatigue lives were predicted with these models. Studies dealing with predictions of low cycle fatigue endurance which are based on experiments with 316L steel are not so usual as well. As mentioned earlier, 304(L) steel is similar to 316L steel, it is therefore acceptable to mention papers dealing with this material in the upcoming section.

SWT and FS models were adopted for the fatigue life prediction of 316 and 304 steel subjected to various loading paths in a study performed by Cruces et al. [145]. Analysis of their results revealed that the SWT model produced more accurate predictions for 304 steel. The FS model proved to be a better choice for 316 steel. Another author's conclusion stated that fatigue lives in A mode was predicted more precisely with the SWT model. The FS model, on the other hand, yielded predictions with a good level of accuracy in the case of T mode. These findings coincide with our results because utilizing the SWT model led to better estimations of fatigue endurance under A loading while the FS model provided significantly more accurate predictions in T mode. It is comprehensible since T fatigue life test data were utilized for calibration of the FS model. On the contrary, the SWT model was calibrated using the data from A fatigue life tests.

The 316L steel was tested under five loading paths by Jin et al. [128]. The fatigue endurance was subsequently estimated with SWT, FS, and KBM criteria and compared with experimental results. All predictions corresponding to FS and KBM models lay within the factor-two-band. A comparable amount of datapoints were found inside the band when the FS model was applied in our study (97.8 %). Only 73.3 % of predictions fell inside the factor-two-band using the WB model. Authors also claimed that significantly non-conservative estimations were achieved when fatigue lives under non-proportional loading mode were estimated with the SWT model.

Bemfica et al. [58] chose 304L steel for their study consisted of applying five loading modes and predicting fatigue lives with FS and SWT criteria. They concluded that utilized models provided results exhibiting a comparable level of precision. Around ten percent of datapoints were found outside the factor-four-band while thirty percent of datapoints lay outside the factor-two-band. The authors also noted that both criteria yielded imprecise estimations in the case of low amplitudes. As may be seen from Tab. 17, AER corresponding to the SWT is substantially higher than AER of the FS model. The reason is an exceptionally wrong estimation of fatigue lives in T mode.

In the study from Liu et al. [90] FS, KBM, and SWT criteria were utilized to forecast the fatigue endurance of four materials. It is noteworthy that the extent of their experiments was rather limited. For example, only a single test was performed for the proportional loading of 316L steel. Two proportional tests were executed for analyzing 45 steel and an identical situation was noted for the non-proportional loading of aluminum alloy 7075. According to the authors, the KBM criterion provided the best estimations in the case of proportional loading while the FS criterion yielded the most accurate predictions for the non-proportional mode. Analogous conclusions may be stated based on our results since the WB criterion led to a fairly precise forecast of the fatigue endurance in A, T, and IP modes (contrary to over-conservative predictions in OP mode). The FS model also proved to be a better option for OP mode when compared to WB and SWT models.

There are also papers concluding that the Liu II model provides a good correlation between observed and predicted fatigue lives. FS, WB, SWT, and both Liu's criteria were compared in a study by Yang and Sun [92] which was based on fatigue experiments with samples from 304 steel. They found that predictions obtained by utilizing the Liu II model were the most accurate. The same tendency was revealed in the study by Cruces et al. [146] who compared FS, Liu I, and Liu II models using the data from the cycling of 316 steel. Results presented in this thesis are inconsistent with those from [92] and [146] since only OP and T modes were estimated properly by Liu II criterion.

In the context of multiaxial fatigue, it can be inferred that the WB and FS models exhibit greater accuracy than the SWT model which was predominantly designed for taking into account the effect of non-zero mean stress. The abovementioned studies suggest that the FS criterion yields better estimations of fatigue endurance under conditions of non-proportional loading while the WB model should provide more accurate predictions for proportional loading scenarios. It is supposed to be caused by the inclusion of a normal stress value in the calculation of the FS damage parameter, allowing it to account for additional hardening resulting from non-proportional loading. The findings of other researchers concerning the Liu II model are inconclusive with the results presented in this thesis since more accurate predictions of the fatigue life were achieved utilizing the Liu II model when compared to those based on the FS model.

6.8 Fatigue crack orientation

It is widely recognized that the early crack propagation is life-determining in the case of low cycle fatigue as the initiation period is relatively brief. Consequently, it is important to ascertain

how critical plane models forecast the orientation of the fatigue crack in Stage II. According to Fig. 79, the SWT model produced the best estimations of the fatigue crack orientation. In the SWT criterion, the critical plane is determined as the plane where the range of normal strain reached the maximum value. The critical plane in the SWT model is therefore situated close to the plane of maximum normal stress, and given that the propagation of the crack during Stage II is controlled by normal stress, it seems comprehensible that the SWT model produced a high degree of precision. In contrast, the least accurate outcomes were delivered by criteria that take into account the maximum shear strain plane as the critical. The deflection of fatigue cracks observed in T mode was successfully forecasted only by the SWT model. It was revealed that the SWT criterion is not able to predict the orientation of fatigue cracks propagating under conditions of non-proportional loading. The estimated and measured angles are however fairly close as the strain amplitude increases.

No examined criterion was thus able to provide proper estimations of the crack deflection angle regardless of the loading path. The same conclusion was pronounced by Bemfica et al. [58] in their study aimed at cyclic straining of 304L steel in various loading modes. They tried to predict the crack deflection utilizing Jiang, SWT, and FS criteria. Predictions based on the FS model were found to be the least successful. Neither Jiang nor SWT was capable of providing proper estimations in all loading modes.

6.9 Tensile and shear driven cracks

As mentioned earlier, the FS model provided the most accurate predictions of fatigue lives according to both adopted metrics – AER and percentage of datapoints lying inside the factor-two-band. The maximum shear strain plane is determined as the critical and the model is supposed to yield precise life predictions for materials exhibiting a tendency towards cracking according to shear mode. The best estimations of fatigue crack deflection were achieved when the SWT model was applied. The SWT criterion’s critical plane is determined as the plane experiencing the maximum normal strain. The criterion was initially designed for analyzing materials cracking according to tensile mode.

The abovementioned results may appear inconsistent. The fatigue endurance was estimated precisely using the criterion which defines the maximum shear strain plane as critical even though the fatigue crack grew in the plane with maximum normal strain. This seeming inconsistency may be explained by taking into account the initiation and propagation of fatigue cracks in 316L steel subjected to repeated elastic-plastic loading. Usually, numerous fatigue cracks initiate on the surface but the extent of fatigue damage is given by the longest crack's length and its propagation rate. The initial period, during which the fatigue crack grows at a slow rate, is responsible for roughly half of the fatigue life, it is, therefore, crucial in terms of the lifespan. It is well known that the shear mode of crack growth is utilized within individual grains during this period of short fatigue crack propagation (Stage I). Criteria taking the plane experiencing the highest amplitude of shear strain as critical should thus provide accurate estimations of the fatigue durability. In contrast, the crack deflection was determined when the tensile mode of crack growth was involved, i.e. during Stage II. The SWT criterion was therefore found to be the most suitable for predictions of the fatigue crack orientation.

7 Conclusions

The fatigue behavior of 316L steel was studied under conditions of two uniaxial loading modes: tension/compression and pure torsion as well as in two multiaxial modes: in-phase and 90° out-of-phase. Two aspects of microstructural changes were examined in particular: endurance against strain-induced martensitic transformation and developed dislocation structures. The outputs of fatigue tests were utilized for the verification of critical plane models and their ability to predict fatigue life and the orientation of fatigue cracks. The crack growth kinetics was analyzed with two methods. The following conclusions were drawn:

- Tension/compression mode was the most damaging when tests with the same $\varepsilon_{a,eq}$ is compared. Pure torsion, on the other hand, led to the longest fatigue lives and the slowest crack growth rates.
- The Massing behavior was not observed in any loading mode, suggesting that different microstructure develops in cycling with increasing strain amplitudes.
- Three fatigue life stages were determined based on analysis of hardening/softening curves: initial hardening, softening, and secondary hardening. Their intensity was dependent on loading mode and strain amplitude.
- Cycling in tension/compression, torsional and in-phase mode caused the formation of similar dislocation structures. The vein structure was the most frequent in the case of low strain amplitudes, the structure formed under moderate levels of strain amplitude consisted predominantly of primary walls. Dislocation cells were observed when high strain amplitudes were applied.
- The arrangement of dislocations developed under out-of-phase loading was characterized by the formation of secondary walls and labyrinth structure even at moderate levels of strain amplitude. It has risen due to the change of the primary slip system during every loading cycle. The distinct dislocation structure was the reason for different mechanical responses in out-of-phase mode.
- The heterogeneous distribution of α' martensite in torsional and out-of-phase mode was revealed by EBSD. Measuring its content with the Feritscope may therefore lead to misleading results.
- The most precise predictions of fatigue life were achieved utilizing the model proposed by Fatemi and Socie.
- The angle of fatigue crack tilt was predicted the most accurately by the Smith-Watson-Topper criterion.
- The plastic part of the J-integral provided a universal description of fatigue crack propagation in tension/compression, torsional and in-phase modes. Its application in the case of non-proportional loading is nevertheless still limited. However, this finding suggests that the extent of plasticity at the crack tip is the governing parameter for the crack growth kinetics.

List of author's publications and internships

Papers in Q1 journals:

Poczklán, L., Polák, J., Kruml, T. Comparison of critical plane models based on multiaxial low-cycle fatigue tests of 316 steel. International Journal of Fatigue, 2023; 171. ISSN: 0142-1123.

Slávik, O., Vojtek, T., **Poczklán, L.**, Tinoco, H. A., Kruml, T., Hutař, P. Improved description of low-cycle fatigue behavior of 316L steel under axial, torsional and combined loading using plastic J-integral. Theoretical and Applied Fracture Mechanics, 2022; 118. ISSN: 0167-8442.

Conference papers:

Poczklán, L., Mazánová, V., Kruml, T. Comparison of a cyclic behavior of 316L steel in uniaxial and multiaxial cyclic loading. In Engineering Mechanics 2019 proceedings. Institute of theoretical and applied mechanics of the Czech academy of Sciences, 2019. p. 287-290. ISSN: 1805-8256.

Poczklán, L., Mazánová, V., Gamanov, Š., Kruml, T. Fatigue crack growth rate in axial, torsional and multiaxial mode in 316L austenitic steel. In Materials Structure & Micromechanics of Fracture 2019. Procedia Structural Integrity, 2019. p. 269-274. ISSN: 2452-3216.

Kruml, T., Mazánová, V., **Poczklán, L.**, Chlupová A., Polák, J. Torsional and multiaxial fatigue in 316L austenitic steel. In proceedings of the 13th conference on the Mechanical Behavior of Materials, 2019. p. 491-495. ISBN: 978-1-922016-65-2.

Chlupová, A., **Poczklán, L.**, Man, J., Mazánová, V., Heczko, M., Kruml, T. Character of fatigue damage under axial, torsional and biaxial loading of 316L stainless steel. In Metallography & Fractography. Materials Science Forum, 2020. p. 264-270. ISSN: 1662-9752.

Internships:

Paul Scherrer Institute, Villigen, Switzerland. 1st January to 31st March 2021.

The Polytechnic University of Timisoara, Romania. 22st October to 21st December 2021.

Educational activity:

Leading of laboratory exercise of course 'Introduction to Material Science and Engineering'. Faculty of Mechanical Engineering, Brno University of Technology, February – May 2022.

References

[1] CAMPBELL, F. C. *Fatigue and Fracture: Understanding the Basics*. B.m.: ASM International, 2012. ISBN 978-1-61503-976-0.

[2] GERLAND, M., J. MENDEZ, P. VIOLAN and B. A. SAADI. Evolution of dislocation structures and cyclic behaviour of a 316L-type austenitic stainless steel cycled in vacuo at room temperature. *Materials Science and Engineering: A*. 1989, **118**, 83–95. ISSN 0921-5093. DOI: 10.1016/0921-5093(89)90060-9

[3] MAENG, W. Y. and M. H. KIM. Comparative study on the fatigue crack growth behavior of 316L and 316LN stainless steels: effect of microstructure of cyclic plastic strain zone at crack tip. *Journal of Nuclear Materials*. 2000, **282**(1), 32–39. ISSN 0022-3115. DOI: 10.1016/S0022-3115(00)00401-3

[4] VOGT, J., S. DEGALLAIX and J. FOCT. Low cycle fatigue life enhancement of 316 L stainless steel by nitrogen alloying. *International Journal of Fatigue*. 1984, **6**(4), 211–215. ISSN 0142-1123. DOI: 10.1016/0142-1123(84)90051-3

[5] KRUML, T., J. POLÁK and S. DEGALLAIX. Microstructure in 316LN stainless steel fatigued at low temperature. *Materials Science and Engineering: A*. 2000, **293**(1–2), 275–280. ISSN 0921-5093. DOI: 10.1016/S0921-5093(00)01015-7

[6] KIM, D. W., W. S. RYU, J. H. HONG and S. K. CHOI. Effect of nitrogen on high temperature low cycle fatigue behaviors in type 316L stainless steel. *Journal of Nuclear Materials*. 1998, **254**(2–3), 226–233. ISSN 0022-3115. DOI: 10.1016/S0022-3115(97)00360-7

[7] SRINIVASAN, V. S., M. VALSAN, R. SANDHYA, K. BHANU, S. L. MANNAN and D. H. SASTRY. High temperature time-dependent low cycle fatigue behaviour of a type 316L(N) stainless steel. *International Journal of Fatigue*. 1999, **21**(1), 11–21. ISSN 0142-1123. DOI: 10.1016/S0142-1123(98)00052-8

[8] DEPRES, C., C. F. ROBERTSON and M. C. FIVEL. Low-strain fatigue in 316L steel surface grains: a three dimension discrete dislocation dynamics modelling of the early cycles. Part 2: Persistent slip markings and micro-crack nucleation. *Philosophical Magazine*. 2006, **86**(1), 79–97. ISSN 1478-6435. DOI: 10.1080/14786430500341250

[9] HONG, S. The tensile and low-cycle fatigue behavior of cold worked 316L stainless steel: influence of dynamic strain aging. *International Journal of Fatigue*. 2004, **26**(8), 899–910. ISSN 0142-1123. DOI: 10.1016/j.ijfatigue.2003.12.002

[10] MAN, J., K. OBRTLÍK and J. POLÁK. Study of surface relief evolution in fatigued 316L austenitic stainless steel by AFM. *Materials Science and Engineering: A*. 2003, **351**(1–2), 123–132. ISSN 0921-5093. DOI: 10.1016/S0921-5093(02)00846-8

[11] VILLECHAISE, P., L. SABATIER and J. C. GIRARD. On slip band features and crack initiation in fatigued 316L austenitic stainless steel: Part 1: Analysis by electron back-scattered diffraction and atomic force microscopy. *Materials Science and Engineering: A*. 2002, **323**(1–2), 377–385. ISSN 0921-5093. DOI: 10.1016/S0921-5093(01)01381-8

[12] ALAIN, R., P. VIOLAN and J. MENDEZ. Low cycle fatigue behavior in vacuum of a 316L type austenitic stainless steel between 20 and 600°C Part I: Fatigue resistance and cyclic behavior. *Materials Science and Engineering: A*. 1997, **229**(1–2), 87–94. ISSN 0921-5093. DOI: 10.1016/S0921-5093(96)10558-X

[13] MARSHALL, P. *Austenitic Stainless Steels: Microstructure and mechanical properties*. B.m.: Springer Netherlands, 1984. ISBN 978-0-85334-277-9.

[14] POLÁK, J. Cyclic Deformation, Crack Initiation, and Low-Cycle Fatigue. In: M. H. F. ALIABADI and W. O. SOBOYEJO, ed. *Comprehensive Structural Integrity*. Oxford: Elsevier, 2023, 2–55. ISBN 978-0-323-91945-6. DOI: 10.1016/B978-0-12-822944-6.00077-3

[15] OBRTLÍK, K., T. KRUML and J. POLÁK. Dislocation structures in 316L stainless steel cycled with plastic strain amplitudes over a wide interval. *Materials Science and Engineering: A*. 1994, **187**(1), 1–9. ISSN 0921-5093. DOI: 10.1016/0921-5093(94)90325-5

[16] KRUML, T., V. MAZÁNOVÁ, L. POCZKLÁN, A. CHLUPOVÁ and J. POLÁK. Torsional and multiaxial fatigue in 316L austenitic steel. In: *International Conference on the Mechanical Behaviour of Materials*. 2019, 491–495. ISBN 978-1-922016-65-2.

[17] MAYAMA, T., K. SASAKI and M. KURODA. Quantitative evaluations for strain amplitude dependent organization of dislocation structures due to cyclic plasticity in austenitic stainless steel 316L. *Acta Materialia*. 2008, **56**(12), 2735–2743. ISSN 1359-6454. DOI: 10.1016/j.actamat.2008.02.005

[18] KRUML, T., J. POLÁK, K. OBRTLÍK and S. DEGALLAIX. Dislocation structures in the bands of localised cyclic plastic strain in austenitic 316L and austenitic-ferritic duplex stainless steels. *Acta Materialia*. 1997, **45**(12), 5145–5151. ISSN 1359-6454. DOI: 10.1016/S1359-6454(97)00178-X

[19] MUGHRABI, H. and H. J. CHRIST. Fatigue, Cyclic Deformation and Microstructure. Cyclic Deformation and Fatigue of Selected Ferritic and Austenitic Steels: Specific Aspects. *ISIJ International*. 1997, **37**(12), 1154–1169. ISSN 0915-1559. DOI: 10.2355/isijinternational.37.1154

[20] POLÁK, J., T. KRUML and S. DEGALLAIX. Dislocation substructure in fatigued duplex stainless steel. *Scripta Metallurgica et Materialia*. 1993, **29**(12), 1553–1558. ISSN 0956-716X. DOI: 10.1016/0956-716X(93)90276-X

[21] POLÁK, J., A. VAŠEK and K. OBRTLÍK. Fatigue damage in two step loading of 316L steel I. Evolution of persistant slip bands. *Fatigue & Fracture of Engineering Materials and Structures*. 1996, **19**(2–3), 147–155. ISSN 8756-758X, 1460-2695. DOI: 10.1111/j.1460-2695.1996.tb00954.x

[22] SIMMONS, J. W. Overview: high-nitrogen alloying of stainless steels. *Materials Science and Engineering: A*. 1996, **207**(2), 159–169. ISSN 0921-5093. DOI: 10.1016/0921-5093(95)09991-3

[23] MURAYAMA, M., K. HONO, H. HIRUKAWA, T. OHMURA and S. MATSUOKA. The combined effect of molybdenum and nitrogen on the fatigued microstructure of

316 type austenitic stainless steel. *Scripta Materialia*. 1999, **41**(5), 467–473. ISSN 1359-6462. DOI: 10.1016/S1359-6462(99)00194-3

[24] REED, R. P. Nitrogen in austenitic stainless steels. *The Journal of The Minerals*. 1989, **41**(3), 16–21. ISSN 1047-4838, 1543-1851. DOI: 10.1007/BF03220991

[25] VOGT, J. B., J. FOCT, C. REGNARD, G. ROBERT and J. DHERS. Low-temperature fatigue of 316L and 316LN austenitic stainless steels. *Metallurgical Transactions A*. 1991, **22**(10), 2385–2392. ISSN 0360-2133, 1543-1940. DOI: 10.1007/BF02665004

[26] GERLAND, M., R. ALAIN, B. AIT SAADI and J. MENDEZ. Low cycle fatigue behaviour in vacuum of a 316L-type austenitic stainless steel between 20 and 600°C—Part II: Dislocation structure evolution and correlation with cyclic behaviour. *Materials Science and Engineering: A*. 1997, **229**(1–2), 68–86. ISSN 0921-5093. DOI: 10.1016/S0921-5093(96)10560-8

[27] PHAM, M. S. and S. R. HOLDSWORTH. Evolution of Relationships Between Dislocation Microstructures and Internal Stresses of AISI 316L During Cyclic Loading at 293 K and 573 K (20 °C and 300 °C). *Metallurgical and Materials Transactions A*. 2014, **45**(2), 738–751. ISSN 1073-5623, 1543-1940. DOI: 10.1007/s11661-013-1981-7

[28] SRINIVASAN, V., R. SANDHYA, K. BHANU, S. MANNAN and K. RAGHAVAN. Effects of temperature on the low cycle fatigue behaviour of nitrogen alloyed type 316L stainless steel. *International Journal of Fatigue*. 1991, **13**(6), 471–478. ISSN 0142-1123. DOI: 10.1016/0142-1123(91)90482-E

[29] KANAZAWA, K., K. YAMAGUCHI and S. NISHIJIMA. Mapping of Low-Cycle Fatigue Mechanisms at Elevated-Temperatures for an Austenitic Stainless-Steel. *Tetsu to Hagane-Journal of the Iron and Steel Institute of Japan*. 1988, **74**(6), 1097–1104. ISSN 0021-1575.

[30] CAILLARD, D. and J. L. MARTIN. *Thermally Activated Mechanisms in Crystal Plasticity*. Amsterdam; Boston, Mass: Elsevier Science, 2003. ISBN 978-0-08-042703-4.

[31] HONG, S. G. and S. B. LEE. Dynamic strain aging under tensile and LCF loading conditions, and their comparison in cold worked 316L stainless steel. *Journal of Nuclear Materials*. 2004, **328**(2–3), 232–242. ISSN 0022-3115. DOI: 10.1016/j.jnucmat.2004.04.331

[32] MAZÁNOVÁ, V., M. HECZKO, V. ŠKORÍK, A. CHLUPOVÁ, J. POLÁK and T. KRUML. Microstructure and martensitic transformation in 316L austenitic steel during multiaxial low cycle fatigue at room temperature. *Materials Science and Engineering: A*. 2019, **767**, 138407. ISSN 0921-5093. DOI: 10.1016/j.msea.2019.138407

[33] DEY, R., S. TARAFDER and S. SIVAPRASAD. Influence of proportional and non-proportional loading on deformation behaviour of austenitic stainless steel-macro and micro analysis. *Theoretical and Applied Fracture Mechanics*. 2019, **100**, 342–353. ISSN 0167-8442. DOI: 10.1016/j.tafmec.2019.01.031

[34] DOONG, S. H., D. F. SOCIE and I. M. ROBERTSON. Dislocation Substructures and Nonproportional Hardening. *Journal of Engineering Materials and Technology*. 1990, **112**(4), 456–464. ISSN 0094-4289, 1528-8889. DOI: 10.1115/1.2903357

[35] SMAGA, M., F. WALTHER and D. EIFLER. Deformation-induced martensitic transformation in metastable austenitic steels. *Materials Science and Engineering: A*. 2008, **483–484**, 394–397. ISSN 0921-5093. DOI: 10.1016/j.msea.2006.09.140

[36] TOBLER, R. L., A. NISHIMURA and J. YAMAMOTO. Design-relevant mechanical properties of 316-type steels for superconducting magnets. *Cryogenics*. 1997, **37**(9), 533–550. ISSN 0011-2275. DOI: 10.1016/S0011-2275(97)00071-4

[37] BOGERS, A. J. and W. G. BURGERS. Partial dislocations on the {110} planes in the B.C.C. lattice and the transition of the F.C.C. into the B.C.C. lattice. *Acta Metallurgica*. 1964, **12**(2), 255–261. ISSN 0001-6160. DOI: 10.1016/0001-6160(64)90194-4

[38] OLSON, G. B. and M. COHEN. A general mechanism of martensitic nucleation: Part II. FCC→BCC and other martensitic transformations. *Metallurgical Transactions A*. 1976, **7**(11), 1905–1914. ISSN 0360-2133, 1543-1940. DOI: 10.1007/BF02654988

[39] OLSON, G. B. and M. COHEN. Kinetics of strain-induced martensitic nucleation. *Metallurgical Transactions A*. 1975, **6**(4), 791–795. ISSN 0360-2133, 1543-1940. DOI: 10.1007/BF02672301

[40] OLSON, G. B. and M. COHEN. A mechanism for the strain-induced nucleation of martensitic transformations. *Journal of the Less Common Metals*. 1972, **28**(1), 107–118. ISSN 0022-5088. DOI: 10.1016/0022-5088(72)90173-7

[41] KRUPP, U., C. WEST and H. J. CHRIST. Deformation-induced martensite formation during cyclic deformation of metastable austenitic steel: Influence of temperature and carbon content. *Materials Science and Engineering: A*. 2008, **481–482**, 713–717. ISSN 0921-5093. DOI: 10.1016/j.msea.2006.12.211

[42] TALONEN, J. and H. HÄNNINEN. Formation of shear bands and strain-induced martensite during plastic deformation of metastable austenitic stainless steels. *Acta Materialia*. 2007, **55**(18), 6108–6118. ISSN 1359-6454. DOI: 10.1016/j.actamat.2007.07.015

[43] STAUDHAMMER, K. P., L. E. MURR and S. S. HECKER. Nucleation and evolution of strain-induced martensitic (b.c.c.) embryos and substructure in stainless steel: A transmission electron microscope study. *Acta Metallurgica*. 1983, **31**(2), 267–274. ISSN 0001-6160. DOI: 10.1016/0001-6160(83)90103-7

[44] ZHANG, S. Y., E. COMPAGNON, B. GODIN and A. M. KORSUNSKY. Investigation of Martensite Transformation in 316L Stainless Steel. *Materials Today: Proceedings*. 2015, **2**, 251–260. ISSN 2214-7853. DOI: 10.1016/j.matpr.2015.05.035

[45] DAS, A., S. SIVAPRASAD, P. C. CHAKRABORTI and S. TARAFDER. Connection between deformation-induced dislocation substructures and martensite formation in stainless steel. *Philosophical Magazine Letters*. 2011, **91**(10), 664–675. ISSN 0950-0839, 1362-3036. DOI: 10.1080/09500839.2011.608385

[46] PEGUES, J. W., S. SHAO, N. SHAMSAEI, J. A. SCHNEIDER and R. D. MOSER. Cyclic strain rate effect on martensitic transformation and fatigue behaviour of an austenitic stainless steel: Microstructure and fatigue behaviour of 304L stainless steel. *Fatigue & Fracture of Engineering Materials & Structures*. 2017, **40**(12), 2080–2091. ISSN 8756-758X. DOI: 10.1111/ffe.12627

[47] TALONEN, J., H. HÄNNINEN, P. NENONEN and G. PAPE. Effect of strain rate on the strain-induced $\gamma \rightarrow \alpha'$-martensite transformation and mechanical properties of austenitic stainless steels. *Metallurgical and Materials Transactions A*. 2005, **36**(2), 421–432. ISSN 1073-5623, 1543-1940. DOI: 10.1007/s11661-005-0313-y

[48] VARMA, S. K., J. KALYANAM, L. E. MURK and V. SRINIVAS. Effect of grain size on deformation-induced martensite formation in 304 and 316 stainless steels during room temperature tensile testing. *Journal of Materials Science Letters*. 1994, **13**(2), 107–111. ISSN 0261-8028, 1573-4811. DOI: 10.1007/BF00416816

[49] LI, Y., D. YU, B. LI and X. CHEN. Martensitic transformation of an austenitic stainless steel under non-proportional cyclic loading. *International Journal of Fatigue*. 2019, **124**, 338–347. ISSN 0142-1123. DOI: 10.1016/j.ijfatigue.2019.03.020

[50] ITOH, T., M. SAKANE, M. OHNAMI and D. F. SOCIE. Nonproportional Low Cycle Fatigue Criterion for Type 304 Stainless Steel. *Journal of Engineering Materials and Technology*. 1995, **117**(3), 285–292. ISSN 0094-4289, 1528-8889. DOI: 10.1115/1.2804541

[51] REED, R.P. The spontaneous martensitic transformations in 18% Cr, 8% Ni steels. *Acta Metallurgica*. 1962, **10**(9), 865–877. ISSN 0001-6160. DOI: 10.1016/0001-6160(62)90101-3

[52] BAUDRY, G. and A. PINEAU. Influence of strain-induced martensitic transformation on the low-cycle fatigue behavior of a stainless steel. *Materials Science and Engineering*. 1977, **28**(2), 229–242. ISSN 0025-5416. DOI: 10.1016/0025-5416(77)90176-8

[53] SPENCER, K., J. D. EMBURY, K. T. CONLON, M. VÉRON and Y. BRÉCHET. Strengthening via the formation of strain-induced martensite in stainless steels. *Materials Science and Engineering: A*. 2004, **387–389**, 873–881. ISSN 0921-5093. DOI: 10.1016/j.msea.2003.11.084

[54] LEHNHOFF, G. R. and K. O. FINDLEY. Influence of Austenite Stability on Steel Low Cycle Fatigue Response. In: T. S. SRIVATSAN, M. A. IMAM and R. SRINIVASAN, ed. *Fatigue of Materials II*. Hoboken, NJ, USA: John Wiley & Sons, 2012, 201–209. ISBN 978-1-118-53338-3. DOI: 10.1002/9781118533383.ch15

[55] MEI, Z. and J. W. MORRIS. Influence of deformation-induced martensite on fatigue crack propagation in 304-type steels. *Metallurgical Transactions A*. 1990, **21**(12), 3137–3152. ISSN 0360-2133, 1543-1940. DOI: 10.1007/BF02647310

[56] SOCIE, D. Multiaxial Fatigue Damage Models. *Journal of Engineering Materials and Technology*. 1987, **109**(4), 293–298. ISSN 0094-4289, 1528-8889. DOI: 10.1115/1.3225980

[57] LI, J., Z. P. ZHANG, Q. SUN and C. W. LI. Multiaxial fatigue life prediction for various metallic materials based on the critical plane approach. *International Journal of Fatigue*. 2011, **33**(2), 90–101. ISSN 0142-1123. DOI: 10.1016/j.ijfatigue.2010.07.003

[58] BEMFICA, C., L. CARNEIRO, E. N. MAMIYA and F. C. CASTRO. Fatigue and cyclic plasticity of 304L stainless steel under axial-torsional loading at room temperature. *International Journal of Fatigue*. 2019, **125**, 349–361. ISSN 0142-1123. DOI: 10.1016/j.ijfatigue.2019.04.009

[59] MAZÁNOVÁ, V., V. ŠKORÍK, T. KRUML and J. POLÁK. Cyclic response and early damage evolution in multiaxial cyclic loading of 316L austenitic steel. *International Journal of Fatigue*. 2017, **100**, Multiaxial Fatigue 2016: Experiments and Modeling, 466–476. ISSN 0142-1123. DOI: 10.1016/j.ijfatigue.2016.11.018

[60] SPÄTIG, P., M. HECZKO, T. KRUML and H. P. SEIFERT. Influence of mean stress and light water reactor environment on fatigue life and dislocation microstructures of 316L austenitic steel. *Journal of Nuclear Materials*. 2018, **509**, 15–28. ISSN 0022-3115. DOI: 10.1016/j.jnucmat.2018.05.064

[61] FACHERIS, G., K. G. F. JANSSENS and S. FOLETTI. Multiaxial fatigue behavior of AISI 316L subjected to strain-controlled and ratcheting paths. *International Journal of Fatigue*. 2014, **68**, 195–208. ISSN 0142-1123. DOI: 10.1016/j.ijfatigue.2014.05.003

[62] DONG, Y., G. KANG, Y. LIU, H. WANG and X. CHENG. Dislocation evolution in 316L stainless steel during multiaxial ratchetting deformation. *Materials Characterization*. 2012, **65**, 62–72. ISSN 1044-5803. DOI: 10.1016/j.matchar.2012.01.004

[63] KANG, G., Q. GAO, L. CAI and Y. SUN. Experimental study on uniaxial and nonproportionally multiaxial ratcheting of SS304 stainless steel at room and high temperatures. *Nuclear Engineering and Design*. 2002, **216**(1), 13–26. ISSN 0029-5493. DOI: 10.1016/S0029-5493(02)00062-6

[64] STANFIELD, G. Discussion on „The strength of metals under combined alternating stresses". *Proceedings of the Institution of Mechanical Engineers*. 1935, **131**, 93.

[65] FINDLEY, W. N. A Theory for the Effect of Mean Stress on Fatigue of Metals Under Combined Torsion and Axial Load or Bending. *Journal of Engineering for Industry*. 1959, **81**(4), 301–305. ISSN 0022-0817. DOI: 10.1115/1.4008327

[66] WANG, C. H. and M. W. BROWN. A path-independent parameter for fatigue under proportional and non-proportional loading. *Fatigue & Fracture of Engineering Materials and Structures*. 1993, **16**(12), 1285–1297. ISSN 8756-758X, 1460-2695. DOI: 10.1111/j.1460-2695.1993.tb00739.x

[67] KANDIL, F. A., M. W. BROWN and K. J. MILLER. *Biaxial low-cycle fatigue failure of 316 stainless steel at elevated temperatures*. United Kingdom: Metals Society, 1982. ISBN 978-0-904357-41-7.

[68] BROWN, M. W. and K. J. MILLER. A Theory for Fatigue Failure under Multiaxial Stress-Strain Conditions. *Proceedings of the Institution of Mechanical*

Engineers. 1973, **187**(1), 745–755. ISSN 0020-3483, 2058-1203. DOI: 10.1243/PIME_PROC_1973_187_161_02

[69] FATEMI, A. and D. F. SOCIE. A critical plane approach to multiaxial fatigue damage including out-of-phase loading. *Fatigue & Fracture of Engineering Materials and Structures*. 1988, **11**(3), 149–165. ISSN 8756-758X, 1460-2695. DOI: 10.1111/j.1460-2695.1988.tb01169.x

[70] SMITH, K., P. WATSON and T. TOPPER. Stress-Strain Function for Fatigue of Metals. *Journal of Materials*. 1970, **5**(4), 767–778. ISSN 0022-2453.

[71] INCE, A. and G. GLINKA. A generalized fatigue damage parameter for multiaxial fatigue life prediction under proportional and non-proportional loadings. *International Journal of Fatigue*. 2014, **62**, 34–41. ISSN 0142-1123. DOI: 10.1016/j.ijfatigue.2013.10.007

[72] YU, Z. Y., S. P. ZHU, Q. LIU and Y. LIU. Multiaxial Fatigue Damage Parameter and Life Prediction without Any Additional Material Constants. *Materials*. 2017, **10**(8), 923. ISSN 1996-1944. DOI: 10.3390/ma10080923

[73] ZHU, S. P., Z. Y. YU, J. CORREIA, A. DE JESUS and F. BERTO. Evaluation and comparison of critical plane criteria for multiaxial fatigue analysis of ductile and brittle materials. *International Journal of Fatigue*. 2018, **112**, 279–288. ISSN 0142-1123. DOI: 10.1016/j.ijfatigue.2018.03.028

[74] JIANG, Y. A fatigue criterion for general multiaxial loading. *Fatigue & fracture of engineering materials & structures*. 2000, **23**(1), 19–32. ISSN 8756-758X. DOI: 10.1046/j.1460-2695.2000.00247.x

[75] MA, S., B. MARKERT and H. YUAN. Multiaxial fatigue life assessment of sintered porous iron under proportional and non-proportional loadings. *International Journal of Fatigue*. 2017, **97**, 214–226. ISSN 0142-1123. DOI: 10.1016/j.ijfatigue.2017.01.005

[76] ZHU, H., H. WU, Y. LU and Z. ZHONG. A novel energy-based equivalent damage parameter for multiaxial fatigue life prediction. *International Journal of Fatigue*. 2019, **121**, 1–8. ISSN 0142-1123. DOI: 10.1016/j.ijfatigue.2018.11.025

[77] LIU, K. C. *A Method Based on Virtual Strain-Energy Parameters for Multiaxial Fatigue Life Prediction*. B.m.: ASTM International, 1993.

[78] CHEN, X., S. XU and D. HUANG. A critical plane-strain energy density criterion for multiaxial low-cycle fatigue life under non-proportional loading. *Fatigue Fracture of Engineering Materials and Structures*. 1999, **22**(8), 679–686. ISSN 8756-758X, 1460-2695. DOI: 10.1046/j.1460-2695.1999.t01-1-00199.x

[79] ŁAGODA, T., E. MACHA and W. BĘDKOWSKI. A critical plane approach based on energy concepts: application to biaxial random tension-compression high-cycle fatigue regime. *International journal of fatigue*. 1999, **21**(5), 431–443. ISSN 0142-1123. DOI: 10.1016/S0142-1123(99)00003-1

[80] VARVANI-FARAHANI, A. A new energy-critical plane parameter for fatigue life assessment of various metallic materials subjected to in-phase and out-of-phase

multiaxial fatigue loading conditions. *International Journal of Fatigue*. 2000, **22**(4), 295–305. ISSN 0142-1123. DOI: 10.1016/S0142-1123(00)00002-5

[81] KAROLCZUK, A. and E. MACHA. A Review of Critical Plane Orientations in Multiaxial Fatigue Failure Criteria of Metallic Materials. *International Journal of Fracture*. 2005, **134**(3–4), 267–304. ISSN 0376-9429, 1573-2673. DOI: 10.1007/s10704-005-1088-2

[82] FATEMI, A. and N. SHAMSAEI. Multiaxial fatigue: An overview and some approximation models for life estimation. *International Journal of Fatigue*. 2011, **33**(8), 948–958. ISSN 0142-1123. DOI: 10.1016/j.ijfatigue.2011.01.003

[83] VORMWALD, M., O. HERTEL and P. ZERRES. Fatigue of engineering structures under combined nonproportional loads: An overview. *Fatigue & Fracture of Engineering Materials & Structures*. 2018, **41**(7), 1449–1468. ISSN 8756-758X. DOI: 10.1111/ffe.12834

[84] PAPUGA, J. A survey on evaluating the fatigue limit under multiaxial loading. *International Journal of Fatigue*. 2011, **33**(2), 153–165. ISSN 0142-1123. DOI: 10.1016/j.ijfatigue.2010.08.001

[85] YU, Z. Y., S. P. ZHU, Q. LIU and Y. LIU. A New Energy-Critical Plane Damage Parameter for Multiaxial Fatigue Life Prediction of Turbine Blades. *Materials*. 2017, **10**(5), 513. ISSN 1996-1944. DOI: 10.3390/ma10050513

[86] LI, J., X. WANG, R. T. LI and Y. Y. QIU. Multiaxial fatigue life prediction for metals by means of an improved strain energy density-based critical plane criterion. *European Journal of Mechanics - A/Solids*. 2021, **90**, 104353. ISSN 0997-7538. DOI: 10.1016/j.euromechsol.2021.104353

[87] KAROLCZUK, A., J. PAPUGA and T. PALIN-LUC. Progress in fatigue life calculation by implementing life-dependent material parameters in multiaxial fatigue criteria. *International Journal of Fatigue*. 2020, **134**, 105509. ISSN 0142-1123. DOI: 10.1016/j.ijfatigue.2020.105509

[88] AHMADZADEH, G. R. and A. VARVANI-FARAHANI. Fatigue life assessment of steel samples under various multiaxial loading spectra by means of Smith-Watson-Topper type damage descriptions. *Fatigue & Fracture of Engineering Materials & Structures*. 2018, **41**(7), 1588–1601. ISSN 1460-2695. DOI: 10.1111/ffe.12798

[89] CRUCES, A. S., P. LOPEZ-CRESPO, B. MORENO and F. V. ANTUNES. Multiaxial Fatigue Life Prediction on S355 Structural and Offshore Steel Using the SKS Critical Plane Model. *Metals*. 2018, **8**(12), 1060. ISSN 2075-4701. DOI: 10.3390/met8121060

[90] LIU, J., Y. RAN, Y. WEI and Z. ZHANG. A critical plane-based multiaxial fatigue life prediction method considering the material sensitivity and the shear stress. *International Journal of Pressure Vessels and Piping*. 2021, **194**, 104532. ISSN 0308-0161. DOI: 10.1016/j.ijpvp.2021.104532

[91] XUE, L., D. G. SHANG, D. H. LI, L. J. LI, X. D. LIU and H. CHEN. Equivalent energy-based critical plane fatigue damage parameter for multiaxial LCF under variable

amplitude loading. *International Journal of Fatigue*. 2020, **131**, 105350. ISSN 0142-1123. DOI: 10.1016/j.ijfatigue.2019.105350

[92] YANG, S. and J. SUN. Multiaxial fatigue life assessment of 304 austenitic stainless steel with a novel energy-based criterion. *International Journal of Fatigue*. 2022, **159**, 106728. ISSN 0142-1123. DOI: 10.1016/j.ijfatigue.2022.106728

[93] CASTRO, F. and Y. JIANG. Fatigue life and early cracking predictions of extruded AZ31B magnesium alloy using critical plane approaches. *International Journal of Fatigue*. 2016, **88**, 236–246. ISSN 0142-1123. DOI: 10.1016/j.ijfatigue.2016.04.002

[94] WANG, Y. and L. SUSMEL. Estimating the orientation of crack initiation planes under constant and variable amplitude multiaxial fatigue loading. *Procedia Structural Integrity*. 2016, **2**, 21st European Conference on Fracture, ECF21, 20-24 June 2016, Catania, Italy, 3233–3239. ISSN 2452-3216. DOI: 10.1016/j.prostr.2016.06.403

[95] VANTADORI, S., A. CARPINTERI, C. RONCHEI, D. SCORZA, A. ZANICHELLI, Y. OKAMOTO, S. SAITO and T. ITOH. Lifetime estimation for 316 stainless steel specimens by using a critical plane approach. *Procedia Structural Integrity*. 2020, **26**, 1st Mediterranean Conference on Fracture and Structural Integrity, MedFract1, 106–112. ISSN 2452-3216. DOI: 10.1016/j.prostr.2020.06.013

[96] CHEN, X., Q. GAO and X. SUN. Damage analysis of low-cycle fatigue under non-proportional loading. *International Journal of Fatigue*. 1994, **16**(3), 221–225. ISSN 0142-1123. DOI: 10.1016/0142-1123(94)90007-8

[97] ZHANG, J., Q. XIAO, X. SHI and B. FEI. Effect of mean shear stress on torsion fatigue failure behavior of 2A12-T4 aluminum alloy. *International Journal of Fatigue*. 2014, **67**, Multiaxial Fatigue 2013, 173–182. ISSN 0142-1123. DOI: 10.1016/j.ijfatigue.2013.11.012

[98] WANG, X. W., D. G. SHANG, Y. J. SUN and H. CHEN. Multiaxial high-cycle fatigue life prediction model considering mean shear stress effect under constant and variable amplitude loading. *Theoretical and Applied Fracture Mechanics*. 2018, **96**, 676–687. ISSN 0167-8442. DOI: 10.1016/j.tafmec.2017.10.007

[99] SOCIE, D. and G. MARQUIS. *Multiaxial Fatigue*. B.m.: Society of Automotive Engineers, 2000. ISBN 978-0-7680-0453-3.

[100] BANNANTINE, J. A. and D. SOCIE. Observations of Cracking Behavior in Tension and Torsion Low Cycle Fatigue. In: . West Conshohocken: ASTM International, 1988, 899–921. ISBN 978-0-8031-0944-5. DOI: 10.1520/STP24530S

[101] SAKANE, M. and T. ITOH. A synthesis of cracking directions in tension-torsion multiaxial low cycle fatigue at high and room temperatures. *Theoretical and Applied Fracture Mechanics*. 2018, **98**, 13–22. ISSN 0167-8442. DOI: 10.1016/j.tafmec.2018.09.003

[102] SISTANINIA, M. and M. NIFFENEGGER. Fatigue crack initiation and crystallographic growth in 316L stainless steel. *International Journal of Fatigue*. 2015, **70**, 163–170. ISSN 0142-1123. DOI: 10.1016/j.ijfatigue.2014.09.010

[103] QIAN, C. F., M. O. WANG, B. J. WU, S. H. DAI and J. C. M. LI. Symmetric Branching of Mode II and Mixed-Mode Fatigue Crack Growth in a Stainless Steel. *Journal of Engineering Materials and Technology*. 1996, **118**(3), 356–361. ISSN 0094-4289, 1528-8889. DOI: 10.1115/1.2806818

[104] SURESH, S. *Fatigue of Materials*. 2. ed. Cambridge: Cambridge University Press, 1998. ISBN 978-0-521-57847-9. DOI: 10.1017/CBO9780511806575

[105] CHAI, G., R. PENG, K. SLÁMEČKA and S. JOHANSSON. Fatigue Crack Branching Behaviour in Dual Phase Material. In: *12th International Conference on Fracture 2009, ICF-12*. 2009, 4965–4973. ISBN 978-1-6173-227-7.

[106] JÍŠA, D., P. LIŠKUTÍN, T. KRUML and J. POLÁK. Small fatigue crack growth in aluminium alloy EN-AW 6082/T6. *International Journal of Fatigue*. 2010, **32**(12), 1913–1920. ISSN 0142-1123. DOI: 10.1016/j.ijfatigue.2010.06.003

[107] POLÁK, J. and P. ZEZULKA. Short crack growth and fatigue life in austenitic-ferritic duplex stainless steel. *Fatigue and Fracture of Engineering Materials and Structures*. 2005, **28**(10), 923–935. ISSN 1460-2695. DOI: 10.1111/j.1460-2695.2005.00936.x

[108] RITCHIE, R. O. Mechanisms of fatigue-crack propagation in ductile and brittle solids. *International Journal of Fracture*. 1999, **100**(1), 55–83. ISSN 1573-2673. DOI: 10.1023/A:1018655917051

[109] BURDEKIN, F. M. and D. E. W. STONE. The crack opening displacement approach to fracture mechanics in yielding materials. *The Journal of Strain Analysis for Engineering Design*. 1966, **1**(2), 145–153. ISSN 0309-3247. DOI: 10.1243/03093247V012145

[110] DONG, Q., P. YANG, G. XU a J. DENG. Mechanisms and modeling of low cycle fatigue crack propagation in a pressure vessel steel Q345. *International Journal of Fatigue*. 2016, **89**, Special Issue: Crack Tip Fields 3, 2–10. ISSN 0142-1123. DOI: 10.1016/j.ijfatigue.2016.03.026

[111] VASCO-OLMO, J. M., F. A. DÍAZ, F. V. ANTUNES and M. N. JAMES. Characterisation of fatigue crack growth using digital image correlation measurements of plastic CTOD. *Theoretical and Applied Fracture Mechanics*. 2019, **101**, 332–341. ISSN 0167-8442. DOI: 10.1016/j.tafmec.2019.03.009

[112] ANTUNES, F. V., M. S. C. FERREIRA, R. BRANCO, P. PRATES, C. GARDIN and C. SARRAZIN-BAUDOUX. Fatigue crack growth versus plastic CTOD in the 304L stainless steel. *Engineering Fracture Mechanics*. 2019, **214**, 487–503. ISSN 0013-7944. DOI: 10.1016/j.engfracmech.2019.04.013

[113] BERETTA, S., S. FOLETTI and L. PATRIARCA. Discussion of models for LCF small crack growth. *Procedia Engineering*. 2011, **10**, 11th International Conference on the Mechanical Behavior of Materials (ICM11), 3642–3649. ISSN 1877-7058. DOI: 10.1016/j.proeng.2011.04.600

[114] RABBOLINI, S., S. BERETTA, S. FOLETTI and A. RIVA. Short crack propagation in LCF regime at room and high temperature in Q & T rotor steels. *International*

Journal of Fatigue. 2015, **75**, 10–18. ISSN 0142-1123. DOI: 10.1016/j.ijfatigue.2015.01.009

[115] HUTAŘ, P., J. PODUŠKA, M. ŠMÍD, I. KUBĚNA, A. CHLUPOVÁ, L. NÁHLÍK, J. POLÁK and T. KRUML. Short fatigue crack behaviour under low cycle fatigue regime. *International Journal of Fatigue*. 2017, **103**, 207–215. ISSN 0142-1123. DOI: 10.1016/j.ijfatigue.2017.06.002

[116] HUTAŘ, P., J. PODUŠKA, A. CHLUPOVÁ, M. ŠMÍD, T. KRUML and L. NÁHLÍK. Description of short fatigue crack propagation under low cycle fatigue regime. *Procedia Structural Integrity*. 2016, **2**, 21st European Conference on Fracture, ECF21, 20-24 June 2016, Catania, Italy, 3010–3017. ISSN 2452-3216. DOI: 10.1016/j.prostr.2016.06.377

[117] POCZKLÁN, L., J. POLÁK and T. KRUML. Comparison of critical plane models based on multiaxial low-cycle fatigue tests of 316L steel. *International Journal of Fatigue*. 2023, **171**, 107569. ISSN 0142-1123. DOI: 10.1016/j.ijfatigue.2023.107569

[118] SLÁVIK, O., T. VOJTEK, L. POCZKLÁN, H.A. TINOCO, T. KRUML, P. HUTAŘ and M. ŠMÍD. Improved description of low-cycle fatigue behaviour of 316L steel under axial, torsional and combined loading using plastic J-integral. *Theoretical and Applied Fracture Mechanics*. 2022, **118**. ISSN 0167-8442. DOI: 10.1016/j.tafmec.2021.103212

[119] MUGHRABI, H. and H. J. CHRIST. Cyclic Deformation and Fatigue of Selected Ferritic and Austenitic Steels: Specific Aspects. *ISIJ International*. 1997, **37**(12), 1154–1169. DOI: 10.2355/isijinternational.37.1154

[120] POLÁK, J. and K. OBRTLÍK. Surface Relief and Dislocation Structure in Fatigued Copper Single Crystal. In: P. O. KETTUNEN, T. K. LEPISTÖ a M. E. LEHTONEN, ed. *Strength of Metals and Alloys (ICSMA 8)*. Oxford: Pergamon, 1989, 761–766. ISBN 978-0-08-034804-9. DOI: 10.1016/B978-0-08-034804-9.50119-4

[121] MUGHRABI, H. Microscopic Mechanisms of Metal Fatigue. In: P. HAASEN, V. GEROLD a G. KOSTORZ, ed. *Strength of Metals and Alloys*. B.m.: Pergamon, 1979, 1615–1638. ISBN 978-1-4832-8412-5. DOI: 10.1016/B978-1-4832-8412-5.50248-4

[122] DICKSON, J. I., J. BOUTIN and G. L'ESPÉRANCE. An explanation of labyrinth walls in fatigued f.c.c. metals. *Acta Metallurgica*. 1986, **34**(8), 1505–1514. ISSN 0001-6160. DOI: 10.1016/0001-6160(86)90095-7

[123] JIANG, Y., O. HERTEL and M. VORMWALD. An experimental evaluation of three critical plane multiaxial fatigue criteria. *International Journal of Fatigue*. 2007, **29**(8), 1490–1502. ISSN 0142-1123. DOI: 10.1016/j.ijfatigue.2006.10.028

[124] KANAZAWA, K., K. J. MILLER and M. W. BROWN. Low-Cycle Fatigue Under Out-of-Phase Loading Conditions. *Journal of Engineering Materials and Technology*. 1977, **99**(3), 222–228. ISSN 0094-4289. DOI: 10.1115/1.3443523

[125] WU, Z. R., X. T. HU and Y. D. SONG. Multiaxial fatigue life prediction for titanium alloy TC4 under proportional and nonproportional loading. *International Journal of Fatigue*. 2014, **59**, 170–175. ISSN 0142-1123. DOI: 10.1016/j.ijfatigue.2013.08.028

[126] LOPEZ-CRESPO, P., B. MORENO, A. LOPEZ-MORENO and J. ZAPATERO. Study of crack orientation and fatigue life prediction in biaxial fatigue with critical plane models. *Engineering Fracture Mechanics*. 2015, **136**, 115–130. ISSN 0013-7944. DOI: 10.1016/j.engfracmech.2015.01.020

[127] MAZÁNOVÁ, V., V. ŠKORÍK, T. KRUML and J. POLÁK. Cyclic response and early damage evolution in multiaxial cyclic loading of 316L austenitic steel. *International Journal of Fatigue*. 2017, **100**, 466–476. ISSN 0142-1123. DOI: 10.1016/j.ijfatigue.2016.11.018

[128] JIN, D., D. J. TIAN, J. H. LI and M. SAKANE. Low-cycle fatigue of 316L stainless steel under proportional and nonproportional loadings: 316L Stainless Steel, Proportional and Nonproportional Loadings. *Fatigue & Fracture of Engineering Materials & Structures*. 2016, **39**(7), 850–858. ISSN 8756-758X. DOI: 10.1111/ffe.12399

[129] SOHRABI, M. J., M. NAGHIZADEH and H. MIRZADEH. Deformation-induced martensite in austenitic stainless steels: A review. *Archives of Civil and Mechanical Engineering*. 2020, **20**(4), 124. ISSN 1644-9665. DOI: 10.1007/s43452-020-00130-1

[130] PLUMTREE, A and H. A ABDEL-RAOUF. Cyclic stress–strain response and substructure. *International Journal of Fatigue*. 2001, **23**(9), 799–805. ISSN 0142-1123. DOI: 10.1016/S0142-1123(01)00037-8

[131] ROY, S. C., S. GOYAL, R. SANDHYA and S. K. RAY. Low cycle fatigue life prediction of 316 L(N) stainless steel based on cyclic elasto-plastic response. *Nuclear Engineering and Design*. 2012, **253**, SI : CFD4NRS-3, 219–225. ISSN 0029-5493. DOI: 10.1016/j.nucengdes.2012.08.024

[132] GOYAL, S., S. MANDAL, P. PARAMESWARAN, R. SANDHYA, C. N. ATHREYA and K. LAHA. A comparative assessment of fatigue deformation behavior of 316 LN SS at ambient and high temperature. *Materials Science and Engineering: A*. 2017, **696**, 407–415. ISSN 0921-5093. DOI: 10.1016/j.msea.2017.04.102

[133] PUTZ, A., M. ALTHUBER, A. ZELIĆ, E. M. WESTIN, T. WILLIDAL and N. ENZINGER. Methods for the measurement of ferrite content in multipass duplex stainless steel welds. *Welding in the World*. 2019, **63**(4), 1075–1086. ISSN 1878-6669. DOI: 10.1007/s40194-019-00721-4

[134] BECKER, L., J. BOES, J. LENTZ, C. CUI, V. UHLENWINKEL, M. STEINBACHER, R. FECHTE-HEINEN, W. THEISEN and S. WEBER. Quantification of extremely small-structured ferritic-austenitic phase fractions in stainless steels manufactured by laser powder bed fusion. *Materialia*. 2022, **22**, 101393. ISSN 2589-1529. DOI: 10.1016/j.mtla.2022.101393

[135] ZENG, W. and H. YUAN. Mechanical behavior and fatigue performance of austenitic stainless steel under consideration of martensitic phase transformation. *Materials Science and Engineering: A*. 2017, **679**, 249–257. ISSN 0921-5093. DOI: 10.1016/j.msea.2016.10.005

[136] ITOH, T., M. SAKANE, M. OHNAMI and D. F. SOCIE. Nonproportional Law Cycle Fatigue Criterion for Type-304 Stainless-Steel. *Journal of Engineering Materials and*

Technology-Transactions of the Asme. 1995, **117**(3), 285–292. ISSN 0094-4289. DOI: 10.1115/1.2804541

[137] LI, Y. and C. LAIRD. Cyclic response and dislocation structures of AISI 316L stainless steel. Part 2: polycrystals fatigued at intermediate strain amplitude. *Materials Science and Engineering: A*. 1994, **186**(1–2), 87–103. ISSN 0921-5093. DOI: 10.1016/0921-5093(94)90307-7

[138] POLÁK, J., I. KUBĚNA a J. MAN. The shape of early persistent slip markings in fatigued 316L steel. *Materials Science and Engineering: A*. 2013, **564**, 8–12. ISSN 0921-5093. DOI: 10.1016/j.msea.2012.11.086

[139] BABINSKÝ, T., I. KUBĚNA, I. ŠULÁK, T. KRUML, J. TOBIÁŠ and J. POLÁK. Surface relief evolution and fatigue crack initiation in René 41 superalloy cycled at room temperature. *Materials Science and Engineering: A*. 2021, **819**, 141520. ISSN 0921-5093. DOI: 10.1016/j.msea.2021.141520

[140] REDDY, G. V. P., R. SANDHYA, M. D. MATHEW and S. SANKARAN. The Effect of Nitrogen Alloying on the Low Cycle Fatigue and Creep-Fatigue Interaction Behavior of 316LN Stainless Steel. *Advanced Materials Research*. 2013, **794**, 441–448. ISSN 1662-8985. DOI: 10.4028/www.scientific.net/AMR.794.441

[141] IBRAHIM, M. F. E. and K. J. MILLER. Determination of Fatigue Crack Initiation Life. *Fatigue & Fracture of Engineering Materials & Structures*. 1979, **2**(4), 351–360. ISSN 1460-2695. DOI: 10.1111/j.1460-2695.1979.tb01093.x

[142] DÖRING, R., J. HOFFMEYER, T. SEEGER and M. VORMWALD. Short fatigue crack growth under nonproportional multiaxial elastic–plastic strains. *International Journal of Fatigue*. 2006, **28**(9), 972–982. ISSN 0142-1123. DOI: 10.1016/j.ijfatigue.2005.08.012

[143] POLÁK, J. On the role of point defects in fatigue crack initiation. *Materials Science and Engineering*. 1987, **92**, 71–80. ISSN 0025-5416. DOI: 10.1016/0025-5416(87)90157-1

[144] POLÁK, J. and J. MAN. Experimental evidence and physical models of fatigue crack initiation. *International Journal of Fatigue*. 2016, **91**, Variable Amplitude Loading, 294–303. ISSN 0142-1123. DOI: 10.1016/j.ijfatigue.2016.02.021

[145] CRUCES, A. S., P. LOPEZ-CRESPO, S. BRESSAN, T. ITOH and B. MORENO. On the Behaviour of 316 and 304 Stainless Steel under Multiaxial Fatigue Loading: Application of the Critical Plane Approach. *Metals*. 2019, **9**(9), 978. ISSN 2075-4701. DOI: 10.3390/met9090978

[146] CRUCES, A. S., A. GARCIA-GONZALEZ, B. MORENO, T. ITOH and P. LOPEZ-CRESPO. Critical plane based method for multiaxial fatigue analysis of 316 stainless steel. *Theoretical and Applied Fracture Mechanics*. 2022, **118**, 103273. ISSN 0167-8442. DOI: 10.1016/j.tafmec.2022.103273

List of abbreviations

A	axial
BM	Brown-Miller model
BMC	Basquin-Manson-Coffin model
CGR	crack growth rate
CTOD	crack tip opening displacement
EBSD	diffraction of back scattered electrons
FIB	focused ion beam
FL	fatigue life
FS	Fatemi-Socie model
GSA	generalized strain amplitude model
GSE	generalized strain energy model
IP	in-phase
KBM	Kandil-Brown-Miller model
MGSE	modified strain energy model
MSWT	modified Smith-Watson-Topper model
OP	out-of-phase
PH	primary hardening
PSB	persistent slip band
PSM	persistent slip markings
RT	room temperature
S	softening
SEM	scanning electron microscope
SFE	stacking fault energy
SH	secondary hardening
SWT	Smith-Watson-Topper model
T	torsional
TEM	transmission electron microscope
TRIP	transformation induced plasticity
WB	Wang-Brown model

List of symbols

a	crack length
a_{MSWT}	material parameter of MSWT model
A	fracture elongation
AER	average error of fatigue life predictions
b	fatigue strength exponent
b_0	shear fatigue strength exponent
c	fatigue ductility exponent
c_0	shear fatigue ductility exponent
E	Young's modulus
ER	error of fatigue life prediction
f_{NP}	factor of non-proportionality
G	shear modulus
J	J-integral
K	material parameter of FS model
k_g	crack growth coefficient
k_{MGSE}	material parameter of MGSE model
K'	coefficient of cyclic hardening
L	coefficient of non-proportional hardening
L_{Li}	weight index of Li model
m_F	number of uniaxial experiments
N	number of loading cycles
N_f	number of loading cycles to failure
$N_{f\,CGR}$	number of loading cycles to failure for crack growth rate tests
N_{1000}	number of loading cycles when the crack length reached 1000 μm
N_{600}	number of loading cycles when the crack length reached 600 μm
n'	cyclic strain hardening exponent
P_F	parameter for a determination of weight index L
PH_I	primary hardening
$R_{p0,2}$	0.2 % proof stress
R_m	ultimate tensile stress
S	coefficient of normal strain influence
S_I	softening
SH_I	secondary hardening
t	time

List of symbols

$t_{propagation}$	percentual part of fatigue life spent by propagation of fatigue crack
T	period
α	angle
γ	shear strain
γ_f'	shear fatigue ductility coefficient
ε	normal strain
ε_f'	fatigue ductility coefficient
ν	Poisson's ratio
ξ	angle between ε_{1max} and ε_1
ξ_{Zhu}	weight factor of Zhu model
σ	normal stress
σ_y	yield stress
σ_f'	fatigue strength coefficient
τ	shear stress
τ_f'	shear fatigue strength coefficient
ϕ	non-proportionality factor

Superscripts and subscripts:

1	principle
a	amplitude
corr	corresponding
e	elastic
eq	equivalent
eff	effective
fc	first loading cycle
m	mean
max	maximum
n	normal
p	plastic
x	x direction
xy	y direction, parallel to a plane whose normal is in the x direction
α	inclined by angle α
Δ	range